UNIVERSITY OF TROMSØ UIT

FACULTY OF SCIENCE AND TECHNOLOGY
DEPARTMENT OF PHYSICS AND TECHNOLOGY

Studies of plasma potential with emissive probes in the low temperature plasma experiment NJORD

Christian-Georg Schregel

FYS-3900 Master's Thesis in Physics

November 2012

Studies of plasma potential with emissive probes in the low temperature plasma experiment NJORD

For the ones dear to my heart that gave me the strength to write this thesis.

"Basic research is what I'm doing when I don't know what I'm doing"

Wernher von Braun, 1957

Contents

Chapter 1

Introduction

The current thesis is focused on the application of an emissive probe in a RF plasma experiment, NJORD. The plasma in NJORD is created via application of a specific type of electromagnetic wave, known as helicon wave. Experiments such as NJORD enable to create an ion beam through a double layer which is kept up without the need for a current [1], thus making this class of experiments an interesting option for space propulsion. With the concept being relatively new, a number of open questions about the physics involved still remain. Emissive probes on their own are a tool to get reliable plasma potential measurements, even for plasmas with RF oscillations. In experiments such as NJORD, the diagnostics used so far have mainly been the retarding field analyzers and Langmuir probes. By using emissive probes, the goal has been to have a quicker way to determine the plasma potential for potential mapping. In the course of research for this thesis it has turned out, that when looking into the characteristics obtained by the emissive probe, it is not as easy as anticipated in the beginning. Unexpected results have made obtaining simple potential profiles quite challenging, but have also revealed some highly interesting details.

Chapter 2

Basic Concepts

Although the concepts and terms repeated in this chapter should be commonly known to the valued reader within the field of plasma physics, the author is convinced that these concepts should be repeated to get an understanding which nomenclature was used. It also serves to clarify from which kind of formula and assumption about the physics the algebra was done to reach the final formula. Often, in a discipline like experimental plasma physics, the basic assumptions differ in small but significant details, leading to different understandings of the processes involved in the experiment. Different books on plasma physics hold different points of view on the topic of plasma physics as a whole. While one book is emphasizingg MHD another book stresses a more single particle centered point of view. As such, the following chapter as well as the plasma theory chapter are taken from several books, namely [2],[3], [4] and [5] and represent a blend of descriptions given by this books that where deemed most fit to deliver a useful insight into the basic principles.

2.0.1 Notation remarks

It should be noted at the beginning of the thesis that it has in some parts an uncommon notation. As it is in parts aimed as a guideline for further emissive probe studies at NJORD, sometimes instead of the common, shorter notation, a more extended, explanatory notation has been chosen to reduce possible confusion. The following three deviations from common practice should be pointed out specifically:

- $\triangle$ has not been chosen for any differences, but only as the Lapace Operator. All differences are expressed complete to clarify, what difference between quantities is used or have their own variable to prevent misunderstanding.

- Variables encoding quantities of same units have the same variable and extended indices. This was done to enable an easier look on the physics. E.g. that a division of two frequencies takes place and thus yields a dimensionless parameter.
- All divisions are expressed as $\frac{a}{b}$ while a/b always means "a or b". This is done in the context that a "," in a complex formula is easier overlooked.

2.1 Plasma Parameters

Before any useful treatment of the phenomena in plasmas can be conducted, a small distinction about the boundaries of what defines a plasma should be made. From this, the important basic parameters and the scales those parameters are commonly found on can be derived. E.g. is it crystal clear, that in this work, dimensions in the range of km are completely irrelevant. The parameter g, in literature like [4] called "the plasma parameter", is treated a bit later in a separate section. A good first definition is given by [2]: "A plasma is a quasi neutral gas of charged and neutral particles which exhibit collective behavior". In this short sentence, there are already buried several parameters of importance. Coming first to mind are the densities of the neutrals, the species of ions and electrons, or used as variables here: $n_n; n_{i_{a/b/c}}$ and n_e. The prerequisite of quasi neutrality along with the fact that in this experiments only one type of gas was used at a time is making the use of a single "charge-carrier density" $n_0 = n_i = n_e$ feasible. Subsequently, other parameters of interest are those that guide the collective behavior. For a neutral gas, first comes to mind the classical triplet of pressure, temperature and volume. Pressure, while being an important parameter for experimental settings and reproducibility, is absorbed into the knowledge of the particle densities. Volume is only important to ensure, that the conditions detailed in chapter 2.3 are obeyed, so that the plasma falls into a part that can be treated as "endlessly expanded". When close to the walls it is governed by sheath formation process, for whom more details are given i in chapter 3.1. The remaining parameter, temperature, needs to be treated a bit more careful. Temperature is easily defined in a more classical sense, but in plasmas, a closer look is advised. A deeper discussion follows in chapter 2.2. For now it just should be noted that it is handy to define an electron-temperature T_e and an ion-temperature $T_{i_{a/b/c}}$. The last parameters to be defined are the ones guiding the behavior of charge-carriers, the magnetic field B and the electric field, which in electrodynamics is better parameterized by the electric potential. So for a plasma this potential is called the plasma-potential Φ. The challenge in plasma physics is the fact that the collective behavior causes B and ϕ, which in turn cause collective behavior. The problem of this simple

Parameter	Variable used	Common value expected in NJORD
Electron Density	n_e	$10^{10} - 10^{12} m^{-3}$
Ion Density	n_i	$10^{10} - 10^{12} m^{-3}$
Neutral Density	n_n	
Ion Temperature	T_i	0,1-02 eV
Electron Temperature	T_e	3-6 eV
Magnetic Field	B	0,001-0,02 Tesla
Plasma Potential	Φ	50-60 V

Table 2.1: Overview of basic parameters and their expected values

loop-like problem is detailed in [3], and it is the goal of understanding in plasma physics to identify self-consistent solution to this problem which manifest in stable or repeating phenomenons.

2.2 Definition of Temperature

As shortly mentioned earlier, the concept of temperature needs a closer look. Temperature is normally defined as a parameter defining a certain Maxwell-Boltzmann like velocity-distribution, with the formula for a Maxwell-Boltzmann Distribution (1-Dimensional treatment is given here only. A 3-Dimensional would be an analogous superposition) being:

$$f(v) = A \cdot \exp\left(\frac{-\frac{1}{2}mv^2}{\kappa T}\right) \tag{2.1}$$

In a plasma, containing electrons and ions, which vastly differ in mass (for Argon e.g. the ratio $\frac{m_{electron}}{m_{ion}}$ is $1,37 \cdot 10^{-5}$), heating mechanisms can mainly affect either ions or electrons, resulting in different velocity-distribution-functions. Thus, it is advised to use separate temperatures for both species. More important is, that the basic assumption of the distribution shape can be off. E.g. in NJORD, a distinct ion-beam can form, and the RF-Signal used to drive the plasma source impacts the distribution too. Further, the theory behind the plasma diagnostic methods to access the plasma parameters is often based on the assumption of a Maxwell-Boltzmann like population. This can lead to an systematic error when applying those methods. Sadly, often the theoretical solutions require simplifications to be solvable at all, so until further solutions are found, it is a necessary evil to live with.

Order	Single distribution quantity	Dimension	Multi species quantities
0	Density	Scalar	Charge density, mass density
1	Mean velocity	Vector	Current and mass flow
2	Pressure, Temperature	Tensor	Total pressure
3	Heat flux	3rd order Tensor	Total heat flux

Table 2.2: Moments of a distribution function

2.2.1 Moments of a a distribution function

The *distribution function* is a very basic plasma quality as it is of core value when treating plasmas theoretically. Also, many macroscopic quantities can be determined by determining the so called k-order moments of the distribution function, even when assumptions like Maxwellian distribution are not valid. This, in combination with knowledge of the electric and magnetic fields would give a complete description of any plasma close enough to thermal equilibrium [6]. In practice, it is nearly impossible to obtain them experimentally, although some specialized diagnostics can get very close to obtaining a full distribution function. The k-order moment of a distribution function $f(\vec{v})$ is defined as [6]:

$$M^k = \int f(\vec{v}) (\vec{v})^k \, d^3\vec{v} \tag{2.2}$$

When treating several species at the same time (as ions and electrons) at the same time, the knowledge gets even more detailed. The table 2.2 gives an overview, of which orders of moment correlate to which macroscopic quantity. Although not used extensively in this thesis, in more theoretical works this can then be expanded into the Vlasov equation, leading to Landau damping and detailed analysis of waves in plasmas.

2.3 Debye Shielding

As expressed earlier, it is useful to be able to understand how electric fields penetrate into plasmas. Every charge and thus, every electric field introduced, triggers a response from the plasma. Opposite charges are attracted, while same are repelled and by this, a disturbance of the local charge neutrality (mainly electrons as explained later) is damping out the outside field. This mechanism, called Debye-Shielding, was first discussed by Debye and Hueckel in 1923 [7]. Using fluid assumptions for the charge-carriers, a defining length, the so-called Debye-Length λ_D can be calculated that gives an estimate for a sphere of imbalance from charge neutrality. Outside the Debye-Sphere with radius λ_D, the influence can be neglected and quasi neutrality again be assumed. First, assume a quasi-neutral

background of ions and electrons. Treat both particle species as fluids. To begin the approximation, consider the reaction of the plasma to a test charge particle. Assuming a collision-less plasma, the equation of motion for each species is [3]:

$$m_{e/i}\frac{d\vec{u_{e/i}}}{dt} = q_{e/i}\vec{E} - \frac{1}{n_{e/i}}\nabla P_{e/i} \tag{2.3}$$

Here $\vec{u}$ is the velocity, q is charge and P is the pressure. Invoking another set of assumptions, namely:

- All changes are slow, there is no time-dependence, so that $\frac{d}{dt} \approx 0$.
- There is no induction taking place, so that only an electrostatic potential is considered, $\vec{E} \sim \nabla\Phi$.
- There is no temperature gradient
- The insertion of the test charge does not disturb the plasma in the way. That means, it can be considered in thermal equilibrium. As such it can be characterized by a temperature, which is linked to pressure by the Boltzmann constant κ via $P = n_{e/i}\kappa T_{e/i}$

This set of assumptions collapses the equation of motion into

$$n_{e/i}q_{e/i}\nabla\Phi = -\kappa T_{e/i}\nabla n_{e/i} \tag{2.4}$$

This trivially gives for all three spacial directions the same solution, known as the Boltzmann relation

$$n_{e/i}(x) = n_{e/i_0}e^{\frac{-q_{e/i}\Phi}{\kappa T_{e/i}}} \tag{2.5}$$

Now to look at the Poisson equation to solve for the potential gives

$$\triangle\Phi = \frac{1}{\epsilon_0}\left[\underbrace{q_{test}\delta(\vec{r})}_{Testcharge} + \underbrace{n_e(\vec{r})q_e + n_i(\vec{r})q_i}_{Plasma\ Response}\right] \tag{2.6}$$

For the region of parameters where $\left|\frac{q_{e/i}\Phi}{\kappa T_{e/i}}\right| \ll 1$ is valid, an expansion into a Taylor series is feasible so that 2.5 can be represented as $n_{e/i} = n_{e/i_0}\left[1 - \frac{q_{e/i}\Phi}{\kappa T_{e/i}}\right]$, yielding

$$\triangle\Phi = \frac{1}{\epsilon_0}\left[n_{e_0}q_e\left(1 - \frac{q_e\Phi}{\kappa T_e}\right) + n_{i_0}q_i\left(1 - \frac{q_i\Phi}{\kappa T_i}\right) + q_{test}\delta(\vec{r})\right] \tag{2.7}$$

As the background plasma is neutral, the term $n_{i_0}q_i + n_{e_0}q_e$ gives 0, thus equation 2.7 is simplified to

$$\triangle\Phi - \left[\frac{n_{i_0}q_i^2}{\epsilon_0\kappa T_i} + \frac{n_{e_0}q_e^2}{\epsilon_0\kappa T_e}\right]\Phi = -\frac{q_{test}}{\epsilon_0}\delta(\vec{r}) \tag{2.8}$$

This gives way for a species specific Debye length and an effective Debye length consisting of the inverse square sum of all Debye length involved in the shielding. As the electrons move much faster than the ions, this means ions are shielded by electrons as well as by ions. Electrons in contrast are shielded by other electrons only as they move too fast for any ion shielding to take place.

$$\frac{1}{\lambda_e^2} = \frac{n_{e_0}q_e^2}{\epsilon_0\kappa T_e} \tag{2.9}$$

$$\frac{1}{\lambda_i^2} = \frac{n_{i_0}q_i^2}{\epsilon_0\kappa T_i} \tag{2.10}$$

$$\frac{1}{\lambda_D^2} = \underbrace{\frac{1}{\lambda_e^2}}_{For\ electron\ shielding} + \underbrace{\frac{1}{\lambda_i^2}}_{For\ ion\ shielding} \tag{2.11}$$

Via simple use of a spherical Laplace operator, equation 2.8 can be solved and gives the so called Yukawa Potential that describes the potential of a shielded charge

$$\Phi(\vec{r}) = \frac{q_{test}}{4\pi\epsilon_0 r}\exp\left(-\frac{r}{\lambda_D}\right) \tag{2.12}$$

It is evident, that when being several Debye lengths away from the test charge, there is going to be no noticeable effect of the plasma. This is important when considering the size of the whole plasma and giving credibility to the assumption that the main plasma has infinite extension and is not disturbed by effects due to walls. Also it is a good base for the mental picture of the Debye-Sphere within which particles "feel" the charge, while particles outside are unaffected. There is another, less complicated way to derive the Debye length [2]. Instead of taking care of several shielding species and allowing for a complicated testcharge, in this line of argumentation one assumes an infinitely thin, infinitely extended grid and the ions are assumed to be an unison, static background. The equations are only solved for one dimension. The Taylor expansion is then only done for the electrons and the Laplace Operator solved for one dimension. Using this approach, the total Debye length is to no surprise found to be the electron specific Debye length and the potential away from the grid is found to be:

$$\Phi = \Phi_0\exp\left(-\frac{|x|}{\lambda_D}\right) \tag{2.13}$$

Although encumbered by less math, some assumptions that have been given explicitly in the first method disappear implicitly into the mind experiment with the grid. For laboratory practice, the simple assumption to neglect ions is still valid, as often only the electron temperature is considered to be of importance as $\frac{T_i}{T_i} \leq \frac{1}{10}$. It is also obvious from these equations that the first term in both solutions represents the potential given by the source, while the exponential term describes the damping of the potential due to the plasma.

2.3.1 The Number of Particles within a Debye Sphere

Another useful dimensionless parameter are the particles in a Debye Sphere. For the concept of quasi neutrality to fully work, so that there is no distortion outside the Debye sphere, it must be showed that the number of particles within the Debye sphere is big enough. Else the (statistically based) assumption of shielding breaks down. This can be done by a simple geometric calculation determining the number of particles within a Debye sphere

$$N_D = \frac{3}{4} n_0 \pi \lambda_D^3 \tag{2.14}$$

By demanding that $N_D \gg 1$ fulfillment of this assumption is assured. It should be noted on the side but not executed in detail, that the number of particles in the Debye sphere being high enough is also directly connected to the demand that the plasma can be treated as collision-less (or more precise, to the fact that the amount of low angle changing pass-by‘s are dominant in regard to the amount of head on collisions between particles taking place). The inverse, $\frac{1}{n_0 \lambda_D} = g$ is known in literature as *plasma parameter*, and while intriguing on its own due to the fact that it can be shown to be proportional to the potential to kinetic energy ratio in the plasma, it will not be considered further in this work

2.4 The Plasma Frequency

In the spirit of this chapter it is also feasible to take a look at oscillations in the plasma. To cover the whole field of oscillation in plasmas is quite a big task, but when designing a plasma system that is heated by electromagnetic heating, basic assumptions are necessary. First, we treat the frequency with which electrons react to a local disturbance. As established via the Debye-Length, the disturbance can be taken as appearing over the distance λ_D. Take then the mean velocity the electrons have at a given temperature:

$$v_e = \sqrt{\frac{\kappa T_e}{m_e}} \tag{2.15}$$

From the combination of these we obtain the *electron plasma frequency*:

$$\omega_{pe} = \frac{\sqrt{\frac{\kappa T_e}{m_e}}}{\lambda_D} = \sqrt{\frac{n_e e^2}{m_e \epsilon_0}} \tag{2.16}$$

Analogously an *ion plasma frequency* can be defined:

$$\omega_{pi} = \sqrt{\frac{n_i \left(Ze\right)^2}{m_i \epsilon_0}} \cong 1,32Z\sqrt{\frac{n_i}{A}} \tag{2.17}$$

Where A is the atomic number and Z is the charge number. For the first look at plasmas, when designing an experiment, the electron plasma frequency is of higher importance, so that it is often only referred to as the plasma frequency. Any electric field applied with a frequency below the plasma frequency has no chance of penetrating into the bulk plasma, as the electrons move fast enough to immediately shield it out.

2.5 Magnetic Moment of a gyrating particle

In a helicon setup, there are also magnetic fields present, so a small look at the basic phenomena of single particles in magnetized plasmas is in order. First, assume no electric field and for simplicity reasons a B-Field in the z-direction while the charged particle moves in the x-y-plane (a velocity in z-direction has no impact, as a movement parallel to a magnetic field does not result in a Lorentz-force and thus can be neglected here). The basic equation of motion is:

$$m\frac{d\vec{V}}{dt} = q\vec{v} \times \vec{B} \tag{2.18}$$

Taking the crossproduct and deriving the terms in time gives two equations:

$$m\ddot{v_x} = -\left(\frac{qB}{m}\right)^2 v_x \ \wedge \ m\ddot{v_y} = -\left(\frac{qB}{m}\right)^2 v_y \tag{2.19}$$

Those are the differential equations for a harmonic oscillator. Taking a standard exponential solution approach, this gives a circular motion around a guiding center with the so called *cyclotron frequency* $\omega_c = \frac{|q|B}{m}$. Of interest in this solution is the radius of this motion, called *Larmor Radius*, which is easily found to be $r_L = \frac{v_\perp}{\omega_c} = \frac{mv_\perp}{|q|B}$ with $v_\perp$ the absolute value of velocity in the x-y-plane. Again, this is a parameter to bear in mind, when designing a plasma experiment. Any experiment with dimensions smaller that the Larmor Radius would inevitable suffer from loss

of confinmentt, as the particles gyrate into the wall.
It is also useful to define a *magnetic moment* for gyrating particles in this context, as it helps to describe the phenomenon of the magnetic mirror, as in chapter 3.2, used to trap particles and discussed later in this thesis. An easy access to understanding this concept is to look at the gyrating particle as a current running through a loop. A particle with charge q and cyclotron frequency ω_c is equal to a current loop with $I = \frac{q\omega_c}{2\pi}$ covering the cross section area $A = \pi r_L^2$. This gives the definition of the magnetic moment as:

$$\mu = \frac{q\omega_c}{2\pi} \cdot \pi r_L^2 = \frac{mv_\perp^2}{2B} \tag{2.20}$$

This quantity also plays an important role as it is a conserved quantity in plasmas (one exemplary way to deduct this is given in chapter 3.2) and provides an interesting link between several viewpoints of conserved properties. For example, the magnetic moment is also a representation of the ratio of kinetic energy in the gyromotion to the gyration frequency, which yields $\frac{W_\perp}{B}$, that is also conserved. Further it can be linked to the conservation of the magnetic flux enclosed in one orbit, due to the fact that the enclosed flux is:

$$\Omega = B\pi r_L^2 = \frac{2m\pi}{q^2}\mu \tag{2.21}$$

This can be understood from the fact that if the the density of field lines increases, the Lamor radius decreases accordingly so that still the same amount of field lines is encompassed. Other links, that are not explored or explained in detail here are that, if the system is looked at in Hamiltonian formalism using a cylindrical geometry and the assumption of azimuthal symmetry, a Lagrangian can be defined within which, the canonical angular momentum can be defined, that again turns out to be conserved as it is an adiabatic invariant and directly proportional to the magnetic moment.

Chapter 3

Plasma Theory

This chapter is dedicated to give an overview of the more advanced theoretical concepts playing an important role in the context of this thesis. Without question, this chapter can not reach the goal of completeness, as the field of theoretical plasma physics is constantly developing and expanding. But still, it should give a firm basic understanding of the major processes involved in the NJORD experiment. Another goal of this chapter is to add a level of physical understanding different from the simple conclusion derived by mathematics and consisting of more graphical picture of the processes taking place, to enable an intuitive understanding of NJORD. As with chapter 2, the books mostly used are [3],[4],[2] and [6]

3.1 Sheath formation

The undeniable most important theoretical concept when using Langmuir and emissive probes is that of sheath formation. This is the detailed study of plasma shielding behavior close to objects immersed in it and has been done by Langmuir, though more detailed solutions require numerics [3]. The first situation to look at is that of the *floating potential* Φ_{Float}. This is the potential an electrical isolated object acquires automatically due to electron and ion flux from the plasma towards it. As the electrons are far more mobile then the ions, they hit the object before the ions. That in turn leads to a charge build-up on the object, charging it up negatively with respect to the plasma. The perturbation in the surrounding plasma potential and electron density leads then to a reduced electron- and increased ion-flux towards the object. If the slow down on the electron flux is not enough, the object further charges up negatively with correlating impact on ion and electron flux, until a potential is reached at which electron and ion flux balance each other out. This is the floating potential, that is shielding the plasma from further electron loss.

Solving this problem for a more complicated situation is needed, when the object is set to a certain potential (or grounded). Inhomogeneous parameters add to a nonlinear equation to create an intricate problem solvable only through numerical methods, or well chosen boundary conditions and simplifications.
Assume an one-dimensional problem. Also, assume Maxwellian distributed electrons that then have the following function depending on the electron energy, which is a constant of motion and a potential $\Phi_{relative}(x) = \Phi(x) - \Phi_{plasma}$ that is measured relatively to the bulk plasma and considered negative in regard to the plasma :

$$f_e(v_e,x)) = \frac{n_0}{\sqrt{2\pi\kappa\frac{T_e}{m_e}}} \exp\left(-\left(\frac{\frac{mv^2}{2} + q_e\Phi_{relative}(x)}{\kappa T_e}\right)\right) \tag{3.1}$$

It should also be noted that as a boundary condition, $\lim_{|x|\gg\lambda_D} \Phi_{relative}(x_0) = 0$. Also $\lim_{x\to 0} \Phi_{relative}(x) = V_{bias} - \Phi_{plasma}$, with V_{bias} being the potential bias of an object immersed in the plasma. Integrating the distribution function is a way to to get the density (and further quantities, see 2.2.1). The electron density is by this found to be:

$$n_e(x) = \int_{-\infty}^{\infty} f_e(v,0)\,dv = n_0 \exp\left(\frac{-q_e\Phi_{relative}(x)}{\kappa T_e}\right) \tag{3.2}$$

This expresses, that for a negatively biased probe, only electrons energetic enough are able to overcome this barrier. The closer to the wall, the stronger the barrier, and thus the electron density decreases more and more the closer to the wall. For ions, the situation is slightly more complex. The electron movement is governed mainly by the pressure gradient with respect to the momentum term, while for the ions the momentum is playing a more important role than the pressure. This is in essence the statement that the ions are considered cold. So, several things have to be considered. As a first thought it is handy to remind oneself, that, as there has to be ion flux conservation and the ions are accelerated towards the biased object, the ion density has to decrease to, albeit for other reasons than the electron density and also slower. As the potential has to vanish inside the plasma as set by the boundary conditions, the resulting potential between the bulk plasma and the biased wall has to have a downward slope. This is in essence the call for a completely convex curvature as there are no sources in this simple picture. To find an exact solution for the ion density now, first we have to evoke ion energy conservation with:

$$\frac{1}{2}m_i v_i^2(x) + e\Phi_{relative} = \frac{1}{2}m_i u_0^2 \tag{3.3}$$

Adding in the ion flux conservation:

$$n_{i_0} v_{i_0} = n_i(x)\, v_i(x) \tag{3.4}$$

this gives for the ion density:

$$n_i(x) = \frac{n_{i_0}}{\sqrt{\frac{1-2e\Phi_{relative}(x)}{mv_{i_0}^2}}} \tag{3.5}$$

The one-dimensional Poisson equation governing $\Phi_{relative}(x)$ is then with the assumption of quasineutrality:

$$\frac{d^2\Phi_{relative}}{dx^2} = \frac{n_0 e}{\epsilon_0}\left[\exp\left(\frac{e\Phi_{relative}}{\kappa T_e}\right) - \left(1 - \frac{2e\Phi_{relative}(x)}{m_i v_{i_0}^2}\right)^{-\frac{1}{2}}\right] \tag{3.6}$$

To fulfill the demand of a convex function, the term in rectangular brackets has to be always negative because the ion density is supposed the be higher than the electron density. There are several notations to make this step easier by exchanging to dimensionless variables now and through this step looking at Mach numbers, but this is not done here. Instead a solution that is short and does not change the physical viewpoint is presented as found in [3]. The full expression gives:

$$\left(1 - \frac{2e\Phi_{relative}(x)}{m_i v_{i_0}^2}\right)^{-\frac{1}{2}} > \exp\left(\frac{e\Phi_{relative}(x)}{\kappa T_e}\right) \tag{3.7}$$

Now using the fact that by definition $\Phi_{relative}(x) \leq 0$ for all values, this can be expressed as:

$$\left(1 + \frac{2e\left|\Phi_{relative}(x)\right|}{m_i v_{i_0}^2}\right) < \exp\left(\frac{2e\left|\Phi_{relative}(x)\right|}{\kappa T_e}\right) \tag{3.8}$$

At this point, either a strong assumption or numerics are needed. If using assumptions, it is advised to assume to be very close to the sheath edge to the plasma. This then enables a Taylor expansion of the exponential term, so that the inequality reads:

$$\frac{2e\left|\Phi_{relative}(x)\right|}{m_i v_{i_0}^2} < \frac{2e\left|\Phi_{relative}(x)\right|}{\kappa T_e} + \frac{1}{2}\left(\frac{2e\left|\Phi_{relative}(x)\right|}{\kappa T_e}\right)^2 + \frac{1}{3!}\left(\frac{2e\left|\Phi_{relative}(x)\right|}{\kappa T_e}\right)^3 + \dots \tag{3.9}$$

This enforces the condition that:

$$v_{i_0}^2 > \frac{\kappa T_e}{m_i} \tag{3.10}$$

This velocity, $v_s = \sqrt{\frac{\kappa T_e}{m_i}}$ is known as the *ion acoustic* velocity, and the condition that ions entering the sheath have at least this velocity is know as the *Bohm sheath*

criterion. If this criterion is not fulfilled, the solution for the Poisson equation would be sinusoidally oscillating [6]. This in turn would make a smooth matching from sheath to plasma potential impossible. Or, in a more graphic description [2], it would lead to areas that are not electron repellent, which is again violating the basic assumption that sheath shield from electron loss. Steady state spatial oscillations can be neglected too, as dissipation within the plasma would soon destroy any kind of state that requires such high organization without means to keep it up. Another important point is that this condition also puts an upper limit on sheath formation. To reach the Bohm sheath criterion, the bias potential has to be at least $\Phi_{sheathedge} = \frac{\kappa T_e}{2e}$. If the wall is biased above that, or even positive, no sheath formation can take place. The plasma remains quasi neutral up to the object (for most case. See chapter 3.1.2 for a short outlook those special formation cases).

3.1.1 Floating potential including RF influence

An expression for the floating potential has not been given as this needs special consideration when dealing with RF. Without such, it is simply calculated by using flux balance between electrons and ions:

$$\frac{1}{4} n_s v_{e_{average}} \exp\left(\frac{e\Phi_{float}}{\kappa T_e}\right) = n_s v_s \tag{3.11}$$

This gives:

$$\Phi_{float} = \frac{\kappa T_e}{2e} \ln\left(\frac{2\pi m_e}{m_i}\right) \tag{3.12}$$

When now there is an RF potential present, this changes the behavior. Assuming that the ions are not affected by the quick chances in the potential as the frequency is far higher than their oscillation frequency, (see chapter 2.4 for a definition of the ion plasma frequency), the electrons can still react to the changes in the potential and the current to the object will be determined by the Boltzmann retardation factor adjusted to the instantaneous potential. To derive the floating potential under RF, the electron flux has to be averaged over one RF cycle:

$$< \frac{1}{4} n_s v_{e_{average}} \exp\left(\frac{e(V_{RF}\sin\omega t + \Phi_{RFfloat})}{\kappa T_e}\right) >= n_s v_s \tag{3.13}$$

Evaluating this gives the expression for the floating potential in RF plasmas, which shows two distinct terms. The original floating potential in a DC plasma and a correction term due to the increased electron collection when the sheath is expanded,

that lowers the floating potential.

$$\Phi_{RFfloat} = \frac{\kappa T_e}{e}\left[\underbrace{\frac{1}{2}\ln\left(\frac{2\pi m_e}{m_i}\right)}_{DC\ floating\ potential} - \underbrace{\ln J_0\left(\frac{eV_{RF}}{\kappa T_e}\right)}_{RF\ correction\ to\ potential}\right] \tag{3.14}$$

With J_0 being the zero order Bessel function. For more complex oscillations, the averaging has to adjusted accordingly, as in NJORD a more complex mix of harmonics can be found.

3.1.2 Electron Sheath

While the derivation for the sheath given above is the standard method, it is noteworthy that also pure electron sheath can form. In the absence of ions, a pure electron sheath is possible [8]. This serves to balance out the current, and following this, the electron sheath can only form if the relation for balancing out the loss areas is observed [8]:

$$\frac{A_{ionloss}}{A_{electronloss}} \approx \sqrt{\frac{m_i}{m_e}} \tag{3.15}$$

So electron sheaths can occur around small biased objects (like probes). Fitting this criterion are probe tips, so it is to be considered. Measurements [9] showed a dip in the potential before the electron sheath, which is positive biased towards the plasma. First this was attributed to ion pumping mechanism towards an insulator in the chamber, but further investigations revealed that the potential dip is present independent of this [9], so that an electron sheath can exist for anodes that are seemingly bigger than allowed by equation 3.15. Those electron sheaths are known to be prone to instabilities and those instabilities in turn have been reported to produce a RF magnetic field that excites whistler modes in the plasma [10]

3.2 Magnetic Mirrors

While NJORD is at the moment not configured to run as a magnetic mirror, the geometry of magnetic fields still gives good reason to think about it, as the source is separated from the expansion chamber through a magnetic bottleneck. Also no big impact is expected on the experimental results, for the sake of completeness, the theory for magnetic mirrors is included here. First, a small proof that the magnetic moment μ is a conserved quantity is in order. Assume a bottle shaped magnetic field like the one drawn in figure 3.1. This implies axial symmetry, and

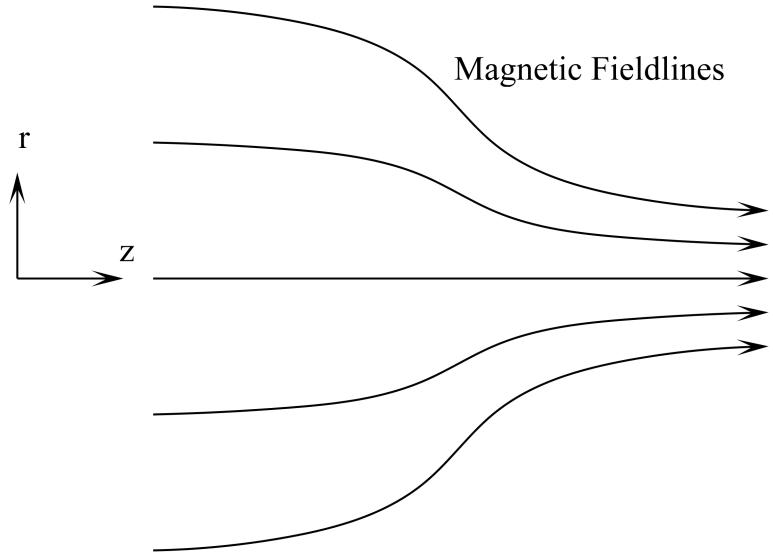

Figure 3.1: Bottleneck Configuration of a magnetic field for the magnetic mirror concept

if cylindrical coordinates are used, $B_\Theta = 0$. To get the bottle shape, the field lines have to converge and B_r has to be quantified. To obtain a more detailed expression, determine the divergence of the magnetic field, $\nabla \cdot \vec{B} = 0$ in cylindrical coordinates:

$$\frac{1}{r}\frac{\partial}{\partial r}(rB_r) + \frac{\partial}{\partial z}B_z = 0 \tag{3.16}$$

When the field is known along the middle axis and $\frac{\partial}{\partial r}B_z$ can be assumed as negligible, this can be solved via integration:

$$rB_r = -\int_0^r r\frac{\partial}{\partial z}B_z = -\frac{1}{2}r^2\left[\frac{\partial}{\partial z}B_z\right]_{r=0} \tag{3.17}$$

Equipped with this way to express B_r, the crossproduct for the Lorentz force on a particle can be calculated. This gives:

$$\vec{F} = q\begin{pmatrix} v_\Theta \cdot B_z - v_z \cdot B_\Theta \\ v_z \cdot B_r - v_r \cdot B_z \\ v_r \cdot B_\Theta - v_\Theta \cdot B_r \end{pmatrix} \tag{3.18}$$

Several terms governing different kinds of motion can be identified in here. First of all, the terms containing B_Θ can be dropped, as it was set to 0 in the beginning. Two terms can be connected to the gyromotion of a particle around a guiding center, specifically:

$$F_r = q \cdot v_\Theta \cdot B_z \cup F_\Theta = -q \cdot v_r B_z \tag{3.19}$$

Another term which interacts with the gyromotion is in equation 3.20. When exactly on the axis of symmetry, this term is also 0. When not on the center axis, it causes the guiding center to follow the magnetic field lines as the particle drifts into the bottle neck of higher B_z:

$$F_\Theta = q v_z B_r \tag{3.20}$$

If there is a a slight gradient in the magnetic field, a ∇B-drift takes place too, as a result of the gyromotion being off from the center axis. This means, that the guiding center of the gyromotion drifts circularly around the center of symmetry axis. So the resulting motion of the guiding center described by equations 3.19 and 3.20 is that of a spiral getting smaller and moving towards the bottleneck.
The last term however is the most interesting. For simplicity, a particle on the central axis is considered, so that the spiraling motion can be neglected. Using the expression derived in equation 3.17 for B_r, this gives the following term, where the definition made in chapter 2.5 is applicable for the average force over one circulation :

$$< F_z >= -\frac{1}{2} q v_\Theta r_L \frac{\partial}{\partial z} B_z = -\mu \frac{\partial}{\partial z} B_z \tag{3.21}$$

From the knowledge about the average force, the time derivative of energy stored in the motion parallel to z is found to be (note, that $\frac{d}{dt}$ is in the reference frame of the particle and also that $B_z \gg B_r$ is assumed):

$$\frac{d}{dt}\left(\frac{1}{2} m v_z^2\right) = -\mu \frac{d}{dt} B \tag{3.22}$$

The time derivative of energy stored in the gyromotion is also easily expressed via the magnetic moment:

$$\frac{d}{dt}\left(\frac{1}{2} m v_\perp\right) = \frac{d}{dt}\left(\mu B\right) \tag{3.23}$$

Combining equation 3.22 and 3.23 with energy conservation by setting the time derivative of the total system energy W to 0 yields that μ has to be a conserved quantity :

$$\frac{d}{dt}\left(\underbrace{-\mu \frac{d}{dt} B}_{\text{Derivative of W in motion parallel to z}} + \underbrace{\mu \frac{d}{dt} B + B \frac{d}{dt} \mu}_{\text{Derivative of W in gyromotion}}\right) = 0 = B \frac{d}{dt} B \tag{3.24}$$

This is also the concept of a magnetic mirror. As a particle moves further into the high B side, to keep μ constant, also the energy stored in the gyromotion must increase. Due to no external energy source, the energy for this must come from

the parallel motion and v_z has to decrease. At some point the particle either has moved through the maximum in the B-field, or it has $v_z = 0$ and is reflected as it in turn picks up speed when moving outward to a lower B-field. A bit of formalism about the ratio of reflected particles is useful, as not all particles can be trapped this way. Particles with a very small μ and a high velocity in z direction can easily overcome the bottleneck. Consider a magnetic bottle with B_{min} at its low field side and B_{max} at its high field side. A particle starting on the low field side with $v_{\Theta_{min}}$ has a certain μ that has to be conserved. Also, the pitch angle Ξ between gyromotion and z-ward motion can be defined as $\tan \Xi = \frac{v_{\Theta_{min}}}{v_{z_{min}}}$ Now assume that the particle turns when reaching z so that $B(z) = B_{max}$ with $v_{\Theta_{max}}$. Then the conservation of μ requires:

$$\frac{1}{2} m \frac{v_{\Theta_0}^2}{B_{min}} = \frac{1}{2} m \frac{v_{\Theta_{max}}^2}{B_{max}} \tag{3.25}$$

Also, conservation of energy applies, so that the total kinetic energy at the start has to be the kinetic energy stored in gyromotion when being reflected. Combination of these two gives a ratio of velocities for that reflection to take place. Via this ratio, a relation angle is defined:

$$\frac{B_{min}}{B_{max}} = \frac{v_{\Theta_{min}}^2}{v_{Total}^2} \equiv \sin^2 \Xi \tag{3.26}$$

This leads to the definition of the mirror ratio $R = \frac{B_{max}}{B_{min}}$ via the ratio of magnetic fields at minimum and maximum value. Any particle with $sin(\Xi) > \sqrt{R}$ is reflected. As insignificant as the whole concept of magnetic mirrors might seem at the first glance, it has strong applications and is a very useful tool in plasma science. Although the loss can never be eliminated completely, as even when all particles with a Ξ are lost, collisions will refill this population, leading to further loss. Still it is a significant step forward in confinement and reason enough to line the walls of plasma experiments with several small magnets, creating many small mirrors. In industrial applications like thin film production, this is also exploited to create trapped pockets of electrons to better ionize gas and increase the plasma particle flow. In addition, pursuits to reach fusion conditions through this concept are done and at CERN, the principle is used to trap anti hydrogen plasma. In NJORD, the machine in which the experiments of this thesis were carried out, the magnets in the source region are configured the way that they also can form a magnetic trap.

3.3 Helicon Waves

Helicon waves are a specific subcategory of waves in plasmas. The first glance into the problem came through the observation of so called whistler waves. Those are waves created in the ionospheric plasma containing a multitude of frequencies like the ones created by lightning strike. The dispersion relation in magnetized plasmas makes the different frequencies arrive at different times at the detector, with the lower frequencies arriving later. Helicon waves are part of that class of waves in magnetized plasmas. The name is derived from waves inside the free electron plasma of metals, but the same waves can be seen in gas plasmas too. As the treatment of waves is analytically very cumbersome, and not every case possible is of interest for this thesis, only the mathematics leading to insight into helicon waves are considered and if possible, logic and mathematic shortcuts are taken. For a broader overview over waves in plasmas the so called CMA diagram can be used as a reference. Every wave treatment in plasmas start with the basic Maxwell equations and the ones governing flow. Already now not every equation possible is necessary to solve the problem. Only some equations form the closed set of equations necessary to describe the waves, while the rests encodes initial conditions. As such, the required equations are invoked as needed and not given as a full set at the beginning. Those equations are all assumed for cold plasmas with small amplitudes, so that linearized versions can be used. So, starting with the velocity of a particle in a plasma fulfilling prior conditions of a cold plasma with a B field in z direction [3]:

$$\vec{v_{i/e}} = \frac{iq_{i/e}}{\omega m_{i/e}} \left[E_z \cdot \vec{e_z} + \frac{\vec{E_\perp}}{1 - \frac{\omega_{c_{i/e}}^2}{\omega^2}} - \frac{i\omega_{c_{i/e}}}{\omega} \frac{\vec{e_z} \times \vec{E}}{1 - \frac{\omega_{c_{i/e}}^2}{\omega^2}} \right] \exp\left(i(\vec{k}\vec{x} - \omega t)\right) \tag{3.27}$$

Those are representations of the $E \times B$ and the generalized drift mechanism taking place and oscillating propagation of an electric field in z-direction. With the particle densities, this gives the plasma current.

$$\vec{I} = n_{0_i} q_i \vec{v_i} + n_{0_e} q_e \vec{v_e} \tag{3.28}$$

This in turn can be used in Amperes law which then takes the full form:

$$\begin{aligned} \nabla \times \vec{B} = \mu_0 \Bigg(& \frac{i\epsilon_0 \omega_{pi}^2}{\omega} \left[E_z \cdot \vec{e_z} + \frac{\vec{E_\perp}}{1 - \frac{\omega_{c_i}^2}{\omega^2}} - \frac{i\omega_{c_i}}{\omega} \frac{\vec{e_z} \times \vec{E}}{1 - \frac{\omega_{c_i}^2}{\omega^2}} \right] \exp\left(i(\vec{k}\vec{x} - \omega t)\right) + \\ & + \frac{i\epsilon_0 \omega_{pe}^2}{\omega} \left[E_z \cdot \vec{e_z} + \frac{\vec{E_\perp}}{1 - \frac{\omega_{c_e}^2}{\omega^2}} - \frac{i\omega_{c_e}}{\omega} \frac{\vec{e_z} \times \vec{E}}{1 - \frac{\omega_{c_e}^2}{\omega^2}} \right] \exp\left(i(\vec{k}\vec{x} - \omega t)\right) \Bigg) + \mu_0 \epsilon_0 \frac{\partial \vec{E}}{\partial t} \end{aligned} \tag{3.29}$$

This however is a very bloated and unhandy formula, so that it is useful to instead absorb it into a tensor $\tilde{K}$. The resulting equation would be:

$$\nabla \times \vec{B} = \mu_o \epsilon_0 \frac{\partial}{\partial t} \left(\tilde{K} \cdot \vec{E} \right) \tag{3.30}$$

The following formalism was introduced by Stix in 1962 [11] and contains some help to memorize what the mathematics means. It will not be explained in detail but rather used as means to an end. Defining the five quantities L for "Left"', R for "Right", S for "Sum", D for "Difference" and P for "Parallel" [3]:

$$R = 1 - \frac{\omega_{pi}^2}{\omega(\omega + \omega_{ci})} + \frac{\omega_{pe}^2}{\omega(\omega - \omega_{ce})} \tag{3.31}$$

$$L = 1 - \frac{\omega_{pi}^2}{\omega(\omega - \omega_{ci})} + \frac{\omega_{pe}^2}{\omega(\omega + \omega_{ce})} \tag{3.32}$$

$$S = \frac{R + L}{2} \tag{3.33}$$

$$D = \frac{R - L}{2} \tag{3.34}$$

$$P = 1 - \frac{\omega_{pi}^2}{\omega^2} + \frac{\omega_{pe}^2}{\omega} \tag{3.35}$$

Although it can be seen as kind of circular logic here, is has already been pointed out, that R and L where chosen to represent right- and left-handed solutions for waves propagating through the plasma. With the simplifications defined, the equation 3.29 in tensor form writes as:

$$\nabla \times \vec{B} = \mu_0 \epsilon_0 \frac{\partial}{\partial t} \left(\left(\begin{array}{ccc} S & -iD & 0 \\ iD & S & 0 \\ 0 & 0 & P \end{array} \right) \cdot \vec{E} \right) \tag{3.36}$$

With this in place, Maxwells equations can be summed up as the equation given in 3.30 and:

$$\nabla \times \vec{E} = -\frac{\partial \vec{B}}{\partial t} \tag{3.37}$$

Now, the so called cold plasma wave equation can be obtained by combining those two into:

$$\nabla \times \left(\nabla \times \vec{E} \right) = -\frac{1}{c^2} \left(\tilde{K} \cdot \vec{E} \right) \tag{3.38}$$

Since all the variables oscillate with $\exp(i\vec{k}\vec{x} - i\omega t)$ as assumed in the beginning, this can be expressed as:

$$\vec{k} \times (\vec{k} \times \vec{E}) = -\frac{\omega^2}{c^2} \tilde{K} \cdot \vec{E} \tag{3.39}$$

Now, in most literature a refractive index is defined for normalization purposes, which here is chosen to be $\vec{\eta} = \frac{c\vec{k}}{\omega}$. This leads then for the cold plasma wave equation, to:

$$\vec{n}\vec{n} \cdot \vec{E} - \eta^2 \vec{E} + \tilde{K} \cdot \vec{E} = 0 \tag{3.40}$$

This can be expressed as one matrix equation. Using spherical coordinates for the refractive index:

$$n_x = n \sin \Theta \tag{3.41}$$

$$n_y = n \cos \Theta \tag{3.42}$$

$$n^2 = n_x^2 + n_y^2 \tag{3.43}$$

This gives for equation 3.40:

$$\begin{bmatrix} S - n^2 \cos^2 \Theta & -iD & n^2 \sin \Theta \cos \Theta \\ iD & S - n^2 & 0 \\ n^2 \sin \Theta \cos \Theta & 0 & P - n^2 \sin^2 \Theta \end{bmatrix} \cdot \begin{bmatrix} E_x \\ E_y \\ E_z \end{bmatrix} = 0 \tag{3.44}$$

This, in essence has reduced the problem of finding a self consistent wave solution in plasmas to an eigenvalue problem. As such, this is the *general dispersion relation for cold plasma waves*. For the existence of non trivial solutions to this, the determinant of the matrix has to be zero. Unless it is zero, only the trivial solution could exist mathematically. This gives the condition:

$$\left(S \sin^2 \Theta + P \cos^2 \Theta\right) n^4 - \left(RL \sin^2 \Theta + PS(1 + \cos^2 \Theta)\right) n^2 + PRL = 0 \tag{3.45}$$

If the wave propagates along B in z direction, this sets $\Theta = 0$ and as such, the determinant simplifies to

$$\left(\left(S - n^2\right)^2 - D^2\right) P = 0 \tag{3.46}$$

This gives three solutions, $P = 0$, $n^2 = R$ and $n^2 = L$, so that two separate dispersion relations exist. They are coupling to different mechanisms. The $n^2 = L$ is driving ions while the $n^2 = R$ is connecting to the electrons. The meaning of this can be seen when determining the eigenvector for $n^2 = R$. This gives a right hand circular polarized wave that propagates in z direction, as the eigenvector relation is $\frac{E_x}{E_y} = i$. Hence the wave is rotating in the same rotation sense as electrons are gyrating due to the B-field. For waves with higher frequencies further simplifications are appropriate [12][5] [3], and the Altar-Appleton-Hartree approximation is to be invoked. This means dropping the ion frequency terms, as the processes take place on a far higher time scale. But for the discussion of helicon waves one has to stick with the solution for medium oscillations with the dispersion relation

$\nu^2 = R$. When all terms that are on of the order $\frac{\omega_{ci}}{\omega_{ce}} = \frac{m_e}{m_i} \ll 1$ are dropped, this gives the expression:

$$\nu^2 = \frac{k^2c^2}{\omega^2} = 1 + \frac{\omega_{pe}^2}{\omega\omega_{ce}\left(1 + \frac{\omega_{ci}}{\omega} - \frac{\omega}{\omega_{ce}}\right)} \tag{3.47}$$

It should be noted that another way to reach this conclusion is to start with the generalized Ohms law [12]. When choosing this procedure, some other physics get accounted for. The leading "1" in the dispersion relation disappears, which is according to Bellan [3] an expression of displacement current. On the other hand, it is easy to include a term to account for the collisions between electrons and neutrals. Now to further narrow down the area of interest, it is only of use to investigate the area just below electron cyclotron resonance. When exactly on the electron cyclotron frequency with the electromagnetic wave, the electrons are constantly experiencing an electric field and thus are accelerated continuously. For even higher frequencies, the refraction index drops below zero, indicating that the wave can not propagate at all. The dispersion relation can then under the assumptions $\omega < \omega_{ce}, \omega_{ce} \ll \omega_{pe}$ and $\omega \ll \omega_{pe}$ be writen as:

$$\nu^2 = \frac{\omega_{pe}^2}{\omega\omega_{ce}\left(1 + \frac{\omega_{ci}}{\omega} - \frac{\omega}{\omega_{ce}}\right)} \tag{3.48}$$

In this range, three wave types can be identified. First, when having a slow wave so that also the term $\frac{\omega}{\omega_{ce}} \ll 1$, the relation turns constant, and gives as limit an Alfven wave as solution for very slow oscillations:

$$\nu^2 = \frac{\omega_{pe}^2}{\omega_{ce}(\omega_{ci} + \omega)} \tag{3.49}$$

On the other side, for oscillations that are close to the electron cyclotron resonance, the term $\frac{\omega_{ci}}{\omega} \ll 1$ can be dropped out so that the dispersion gives:

$$\nu^2 = \frac{\omega_{pe}^2}{\omega\omega_{ce}\left(1 - \frac{\omega}{\omega_{ce}}\right)} \tag{3.50}$$

When operating in this regime, the heating is very efficient, as it is close to the resonance. Finally, there are the helicon waves to be covered. The dispersion relation has a minimum at $\omega \approx 0.5\omega_{ce}$.For frequencies below that, ν^2 does increase again. This is the helicon regime. In this, ions can be considered static so that $\frac{\omega_{ci}}{\omega} \ll 1$ and the electron inertia $\frac{\omega}{\omega_{ce}} \ll 1$ can be dropped. Or in other terms, $\omega_{ci} \ll \omega \ll \omega_{ce}$. This yield the simple relation for helicon waves:

$$\nu^2 = \frac{\omega_{pe}^2}{\omega_{ce}\omega} \tag{3.51}$$

This calculations have been done under the assumption of perfectly aligned waves in relation to the magnetic field. For imperfect alignment, as it might happen under experimental conditions, this changes to [12]:

$$\nu^2 = \frac{\omega_{pe}}{\omega(\omega_{ce}\cos\Theta - \omega)} \tag{3.52}$$

This is in so far of impact for the laboratory experiment as it shows that there is a maximum misalignment angle for which the wave can propagate. Further investigation reveals that the permitted angle of misalignment is even smaller, as for the group velocity of the wave an even smaller angle is permitted [5]. Further attention must be given to the fact, that for the initial derivation, a boundary free plasma was assumed. In this, the helicon waves have the shape of a spiral turning in the right sense. When exited in a cylinder, the boundary conditions give the solution for the magnetic component as follows [5]. With an arbitrary amplitude H (k_z being the wave vector in the B-field direction, k_r perpendicular outwards to this in cylindrical coordinates and $k^2 = k_z^2 + k_r^2$) this gives a more complicated picture:

$$B_r = H\left[(k+k_z)\,J_{m-1}(k_r r) + (k-k_z)\,J_{m+1}(k_r r)\right] = -\frac{k_z}{\omega}E_\Theta \tag{3.53}$$

$$B_\Theta = -iH\left[(k+k_z)\,J_{m-1}(k_r r) - (k-k_z)\,J_{m+1}(k_r r)\right] = \frac{k_z}{\omega}E_r \tag{3.54}$$

$$B_z = -2HiJ_m(k_r r)) \; and \; E_z = 0 \tag{3.55}$$

In this solution calculated by [13], J_m denotes the Bessel function of m-th order. In this context, the different values are called modes. This term of "modes" is not to be confused with other modes and only refers to the Besselfunction without connection to operation regimes in a plasma, that are also called modes. Graphic representation of how the electric field looks like are given for the m=0 mode in figure 3.2 and for the m=1 mode in figure 3.3 The main research focus has been the modes +1, 0 and -1. The m=-1 mode however performs very poorly and couples badly to the plasma, and it is rather a side product of research into the m=1 mode, as antennas designed to excite the m=1 mode can excite the m=-1 too. The m=1 is very good for plasma sources as it couples very well. As antennas designed to excite the m=1 mode have an axial length l, there are also axial modes to be considered and an axial mode number χ is also defined via:

$$k_z = (2\chi + 1)\frac{\pi}{l} \tag{3.56}$$

What makes the helicon so efficient at plasma creation is the fact that unlike the other two RF mechanisms, capacitive and inductive heating, helicon heating takes

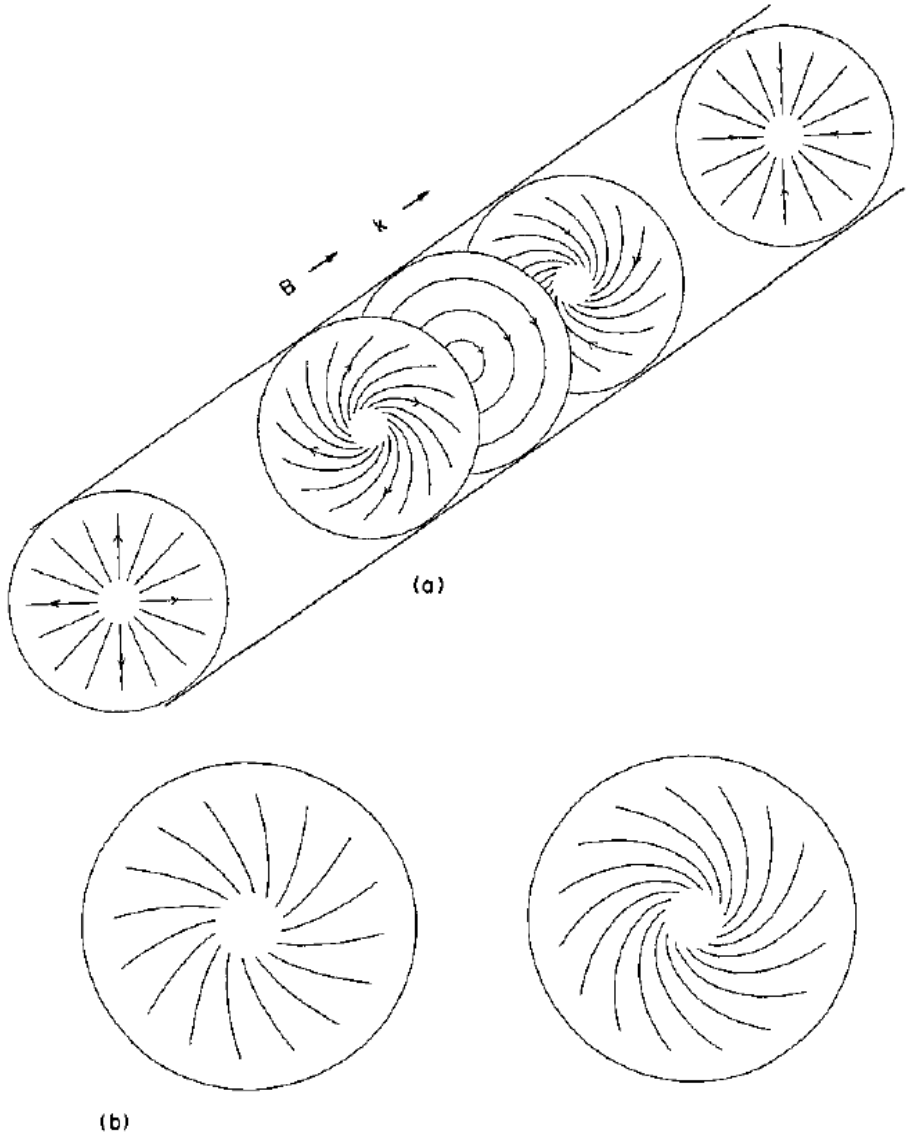

FIG. 1.—Electric field line patterns for the $m = 0$ mode. (a) 3-D representation; (b) cross-sections at $(k/\alpha)\,\mathrm{ctn}\,(kz - \omega t) = 1/3$ (left) and 1 (right).

Figure 3.2: Representation of the helicon mode 0 in a cylinder, taken from [13]

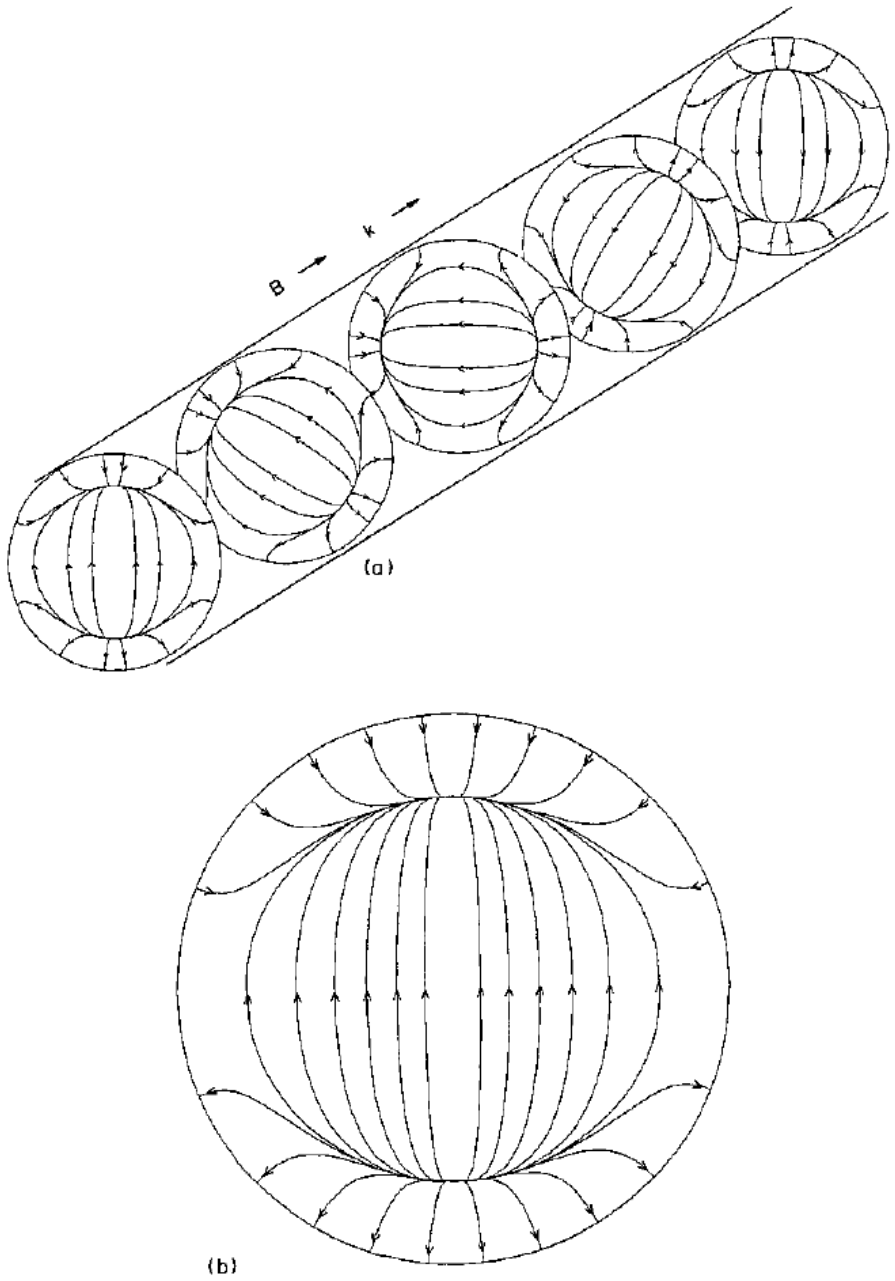

FIG. 2.—Electric field line patterns for the $m = 1$ mode. (a) 3-D representation; (b) detailed pattern for $k/\alpha = 1/3$. Line spacing is indicative of field strength only at $y = 0$.

Figure 3.3: Representation of the helicon mode 1 in a cylinder, taken from [13]

place through collision-less mechanisms (like in capacitive and inductive heating) as well as also through collision mechanisms. But it can also operate by means of pure collision-less mechanisms. It is handy to imagine a step-like process when generating a plasma with a helicon source. The source starts in E-mode, which means a thin, capacitively coupled plasma. Most of the heating takes place by the energy being deposited in the sheath, not unlike the picture of the electric field acting as kind of a piston. As the RF power increases, this switches to the inductive coupled H-mode and the plasma density increases. Here, at least for higher plasma densities, a transformer analogy has been proven to be valid [5]. The one end is the RF source and the plasma is considered a one-turn secondary coil. Further increase then finally leads to operation in the helicon W-mode with even higher plasma density and very high ionization degree.

3.4 Double Layers

A double layer represents a category of special space charge structures. The basic idea is that of a smooth transition step from a high potential to a lower potential. In literature, they are often considered as related to the physics of sheaths [2], [8], and they are even seen forming from simple sheaths that have a potential drop strong enough to ionize the background gas, creating a second plasma [1]. The step in plasma potential over a certain distance has several implications. First, it is obvious by taking the second derivative of this step, that there has to exist two distinct, separate layers of charge carrier species next to each other. From there, two mechanisms of creation are to be considered, as it is obvious that two layers of opposite charge are not naturally stable. If the potential step is kept up by an external influence, then four distinct species emerge. Ions and electrons that due to low kinetic energy get reflected by the double layer when moving towards it and those that have enough energy to move freely through the double layer. Or even get energy by running through the potential drop, charge sign and movement direction are proper. This can give rise to the charge carrier densities. The other way is that at least three of those species are present so that the existence of local heightened carrier density gives rise to the potential drop. For reference of the geometry in this situation also see figure 3.4. Having two layers of higher density of a species also give the double layer its name. The height of particles on the potential axis indicates how much kinetic energy equivalent to potential energy in an electric field they have and the arrow indicates in which direction they move in relation to the double layer.

Far from being a purely theoretical concept, double layers appear in nature and can be created in the laboratory in several ways. The easiest way in the laboratory is a simple dc discharge that has to pass through a constriction. At the end of

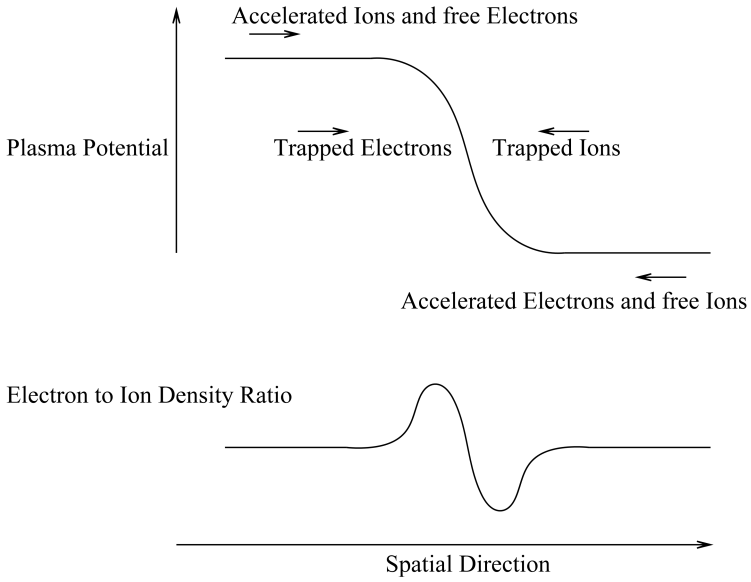

Figure 3.4: Figure of the basic setup of a double layer

this constriction, a double layer forms [14]. Another easy way is to create two separate plasmas and provide an interface area between the two plasmas, which automatically requires the formation of a double layer. Or as stated before, by simply using a sufficiently biased anode in a cathodic plasma. This creates a complex, three dimensional space charge structure known as a fireball. On a side note of interest, the fact should be stated that those fireballs even can contain several double layers in onion-like layering [15]. Other concepts include so called Q machines, that create a quiet plasma in a strongly magnetized tube between an anode and a cathode plate. Common of all the concepts stated before is the fact that they are kept up by a current running in the plasma. But concepts for double layer exists [1], that do not require a current. The older one is that of a device where two distinct electron populations are created and allowed to expand [16]. This was done by timed injection of neutral gas for example. The most complex and challenging formation of double layers however is taking place when a plasma is locally created via RF and then ejected into an expanding geometry via an expanding magnetic field as shown in figure 3.5. This creates a double layer that also is current free. The class of these experiments is referred to as current-free double layers or CFDL [1]. Utilizing the fact that the double layer is current free and thus no neutralizer is needed, the interest has been to fashion this phenomenon into a kind of a plasma thruster for satellites [17]. The experiments on magnetic

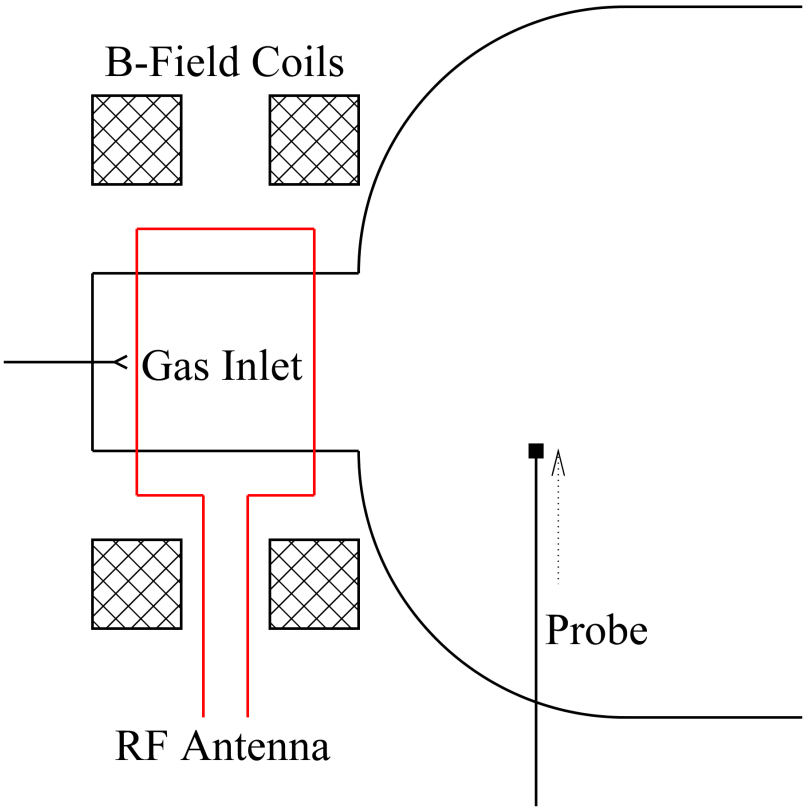

Figure 3.5: Schematic of the NJORD experiment, a typical HDLT creating a CFDL

expansion with RF created plasmas have been conducted with RF setups operating near the helicon regime. As a result, the experiment on which this thesis was conducted is similar to experiments called "Helicon Double Layer Thrusters" or short HDLT. While the work to harness the capabilities of HDLTs has progressed far already, topping with a demonstration of the feasibility of a thruster [1], the physics behind the exact mechanisms on the double layer formation are not yet fully understood and subject to ongoing academic discussion. Three points of view published in recent publications are listed here [1][16][18]. A finite answer to what creates this double layer however is beyond the scope of this thesis.

3.4.1 CFDL Formation according to Charles and Liebermann

When the first current free double layers where diagnosed in HDLTs [1], an explanatory model was given by Liebermann et. al. [19] that, when setup up prop-

erly, could reproduce the results via numerical simulation. It is a simulation of the interaction between two plasmas of different potential. To make the double layer free of current transport, more electrons passing through the potential barrier are needed. The argumentation is that electrons get accelerated inwards into the source in the first step. In the source, those electrons get reflected by the backplate and for the sake of the model are considered as a fifths species of particles. This species substantially adds to the high energetic tail of electrons with enough kinetic energy to cross the double layer and move into the expansion chamber, and is supposed to be numerous enough to balance out the ion current streaming outwards. The numerical model used was able to reproduce the double layer behavior. In detail, there is some deviation between prediction and measurement as the potential rises more in the experiments than anticipated, but the general trend is preserved. A big difference between the theoretical and measured ion beam density has been reported too. It is also noted about this difference, that the measurements are very sensitive and the theoretical assumptions not perfect. Also, the double layer creation is enforced by setting very strict boundary conditions for high and also low potential side, and as such, not emerging from first principles.

3.4.2 CFDL Formation according to Chen

By Chen a very simple, yet compelling analytical breakdown of double layers has been published [18]. The perhaps most important statement by Chen is that, when following through with his line argumentation, the perceived double layers reduces to simple singular sheaths. For this reason, and because it is a first principle argument, his theory is to be included in detail in this thesis. Starting with the assumption of a plasma that is frozen to the field lines, the drop in the magnetic field strength and density by expansion can be linked to the radius r of the expanding plasma:

$$\frac{B}{B_{source}} = \frac{n}{n_{source}} = \left(\frac{r_{source}}{r}\right)^2 \tag{3.57}$$

With Maxwellian electrons, the density drop must mean for the electrons also a drop in plasma potential as they follow the Boltzmann relationship for density to potential relation (note, in the source, both electrons and ions have the density n_{source} and the source potential is chosen to be 0 for convenience, else a relative potential would be required):

$$n_e = n_{source} \exp\left(-\frac{e\Phi}{\kappa T_e}\right) \tag{3.58}$$

The ions, being cold and like in a sheath are governed by their momentum term and first fall through the potential drop created by the electron density drop. At

a certain point, namely when:

$$-\frac{e\Phi}{\kappa T_e} = \frac{1}{2} \tag{3.59}$$

the ions have accumulated a kinetic energy that is equal to the energy when traveling at the ion acoustic speed, which mean, they are fulfilling the Bohm criterion. A quickly dropping electron density and ions at the ion acoustic speed in turn means, that sheath formation has to take place. The exact position in space at which the sheath must form can be determined by looking at the ratio of radii in comparison to the required density drop and gives for the radii ratio the value of 1.28, meaning that the sheath must form when the plasma has expanded by 28% in radius. The ion and electron densities drop, forming a sheath with a related sheath potential until the floating potential is reached:

$$\Phi_{float} = \frac{1}{2}\frac{\kappa T_e}{e}\left(1 + \ln\left(\frac{m_i}{2\pi m_e}\right)\right) \approx 5,18 \cdot \frac{\kappa T_e}{e}\ for\ Ar \tag{3.60}$$

The potential can not fall further as now the flux is balanced. On the contrary, a further fall would require a biased electrode to supply energy to the ions. This is without doubt an elegant argument for the potential drops observed, but Chens model is not without open questions either. An imbalance is in the energy flow to the walls. Calculating the flux after the sheath, the energy lost to the wall per unit area can be expressed for ions:

$$W_i = \frac{e\Phi_{float}}{\kappa T_e} n_0 \exp^{-\frac{1}{2}} \sqrt{\frac{\kappa T_e^3}{m_i}} \tag{3.61}$$

and for the electrons the lost energy to the wall per unit area is:

$$W_e = n_0 \exp\left(-\frac{e\Phi_{float}}{\kappa T_e}\right) \sqrt{\frac{2\kappa T_e^3}{\pi m_e}} \tag{3.62}$$

If now energy conservation requires that those two to be equal, this gives for the required potential on the low potential side the result that:

$$\frac{e\Phi_{required}}{\kappa T_e} \ln\left(\frac{e\Phi_{required}}{\kappa T_e}\right) = \frac{e\Phi_{float}}{\kappa T_e} + \ln(2) \tag{3.63}$$

This shows, that another source of energy is needed, as the required and the floating potential do not balance out. Chen points out, that usually far more energy is supplied. For helicon devices, parts of this energy could form a source, that has not been fully researched yet, as it shows that the perpendicular and parallel ion temperatures seem to interact and interchange energy. After the sheath, device

specific circumstances smooth out the knee when transitioning from sheath to a plasma on floating potential. For the physical process it only plays a minor role and measurements have found the electron part of double layers that fit this model to be very thin only. The ion beam kinetic energy can be at most the energy acquired by dropping through the sheath, or, if the beam undergoes collisions, even lower. Chen states, that this has been experimentally validated by Charles and other measurements [18].

3.4.3 CFDL formation according to Singh

In strong contrast to the explanation given by Chen, a topical review about double layers is published by Singh [16]. The main point of disagreement is the fact that the density drop across the double layer is overestimated strongly, as the measured density ratio is more than 3 times smaller than what would be expected from the simulations. The one dimensionality of the former models is seen as cause for this. Very recently published measurements give two dimensional potential contours for HDLT [20]. In those, very strong perpendicular electric fields can be observed directly at the throat of the source region. The model proposed by Singh to describe the double layer puts emphasis on giving an explanation for the strong perpendicular drop at the throat and the relatively low drop in parallel direction. It is argued for the fact, that within the source, only the electrons have a considerable magnetic moment whereas the ions have a large Lamor radius and negligible magnetic moment. As such, only the electrons are influenced by the diverging magnetic field and are dispersed outwards, while the ions do not follow the field lines and move out of the source region in axial direction. This generates an outward charge separation, resulting in the strong perpendicular electric field. This process creating strong perpendicular electric field also generates an electric field that drops in parallel direction, leading to a u-shaped double layer. This strong perpendicularly electric field then pull the ion beam perpendicularly outwards, resulting in distinct horn shaped structures in the ion density [20]. This is a model that is more encompassing concerning kinetic effects than the one proposed by Chen, and it also states that not all CFDL‘s created in HDLTs are necessarily current free.

3.4.4 Ion Beams

In the discussion of double layer, already the term *ion beam* has been mentioned. This is in reference to two distinct ion populations at different potentials that have been measured in HDLTs. RFEAs turned towards the source show those two distributions, while RFEAs turned 90 degrees away from the source do not show the higher energy distribution but only the lower energy one. From this, it has

been determined that the second distribution must represent kind of an ion beam directed outwards in axial direction, while the lower distribution is representing the background plasma.

Chapter 4

Probe Theory

As the use of an emissive probe is the main topic of this thesis, this chapter is dedicated to give a broad look on emissive probes and the different theories used to describe their behavior. The model picture of an emissive probe has been continuously refined but still, many strong restraints and assumptions are in place to make the mathematics tractable. But even with those assumptions slightly violated, the results obtained by this concept of measurement are reliable and stand up to comparison with other methods.

4.1 Cold Langmuir Probe

Before discussing the fineries of an emissive probe, it is appropriate to look at the theory guiding the behavior a cold probe, also known as Langmuir probe. The idea of this probe is to determine several plasma parameters by applying various voltage and monitoring the current drawn from the plasma. The behavior of this curve, called I-V trace, is in parts governed by the sheath theory.
Three distinct regions have to be accounted for when looking at I-V traces. Ion saturation area, electron collection and electron saturation are identifiable. There is no detailed consideration for the ion collection, as the differences between electrons and ions caused by the different masses cause the ion saturation current to be already so small that it is difficult to look further into the ion collection process and although possible, is cause for problems when using cold probes (The whole concept of an emissive probe described in chapter 4.2 is even to compensate for this small ion current). A typical probe bias versus collected current trace plot obtained with a cold probe is displayed in figure 4.1.

If the probe is sufficiently negatively biased from the floating potential Φ_{float}, it can be assumed that it only draws an ion current. The current to a surface

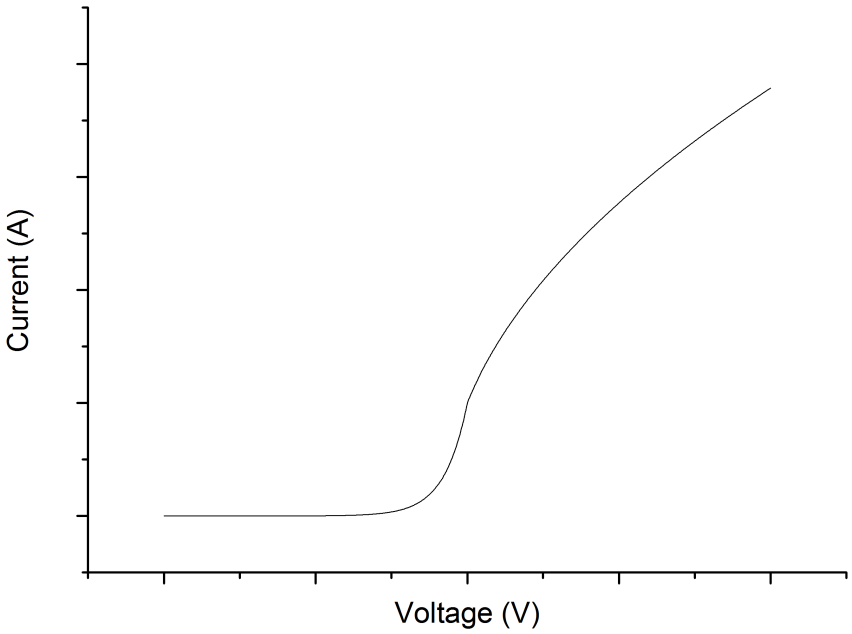

Figure 4.1: I-V Trace for a cold probe, obtained via the simulation code given in appendix A

A_{probe} in a plasma (containing only singly charged ions) is then given by:

$$I_{ionsaturation} = -\frac{1}{4} e A_{probe} \left(n_i \overline{v_i} \right) \tag{4.1}$$

The density can be estimated by looking at the conditions derived for the sheath edge in 3.1. All ions moving through the sheath must fulfill the Bohm criterion, and thus have the velocity:

$$c_s = \sqrt{\frac{\kappa T_e}{m_i}} \tag{4.2}$$

With Maxwellian electrons and the concept of quasi-neutrality, the density of ions at the sheath edge is then:

$$n_{i_{sheathedge}} = n_{e_{sheathedge}} = n_0 \cdot \exp\left(\frac{e\Phi_{sheath-edge}}{\kappa T_e} \right) \approx 0,61 n_0 \tag{4.3}$$

This gives for the ion saturation current:

$$I_{ionsaturation} \approx \underbrace{0,62}_{Scaling factor} \; n_0 \sqrt{\frac{\kappa T_e}{m_i}} A_{probe} \tag{4.4}$$

At this point it should also be noted that this is a very small current that normally is not accounted for at all when analyzing the IV curve in the electron rich part. Even in the established plasma literature, the treatment is often rough and normally not discussed further, resulting in different scaling factors given. In the book by Boyd and Sandersson [4] the scaling factor is given as 0,24 ,because the ions are considered far more strict and accurate via the general formula for the electron density at a given point, that also takes care of electrons not being reflected by the presheath drop:

$$n_e(x) = n_0 \exp\left(\frac{e\Phi(x)}{\kappa T_e} \right) \cdot \frac{1}{2} \cdot \sqrt{1 + \frac{2}{\sqrt{\pi} \int_0^{\Phi(x)-\Phi_{bulk}} e^{-y^2} dy \cdot \frac{e}{\kappa T_e}}} \tag{4.5}$$

In the books by Hutchinson and Chen [6] [2], all electrons are considered as reflected like in this thesis. For practical purposes, Chen however suggests to use 0,5 instead. The other end of assumptions is found in the book by Bellan [3]. There, no distinction between density in the bulk plasma and density at the sheath edge is made, and the scaling between is taken to be simply 1. Once the probe bias is above floating potential but underneath the plasma potential (so, it is still negative in respect to the plasma), a certain amount of electrons will be drawn to the probe. Only electrons with a kinetic energy higher that the barrier imposed by the probe can strike it. As stated earlier, there should be no sheath present, so

the striking current is the random current reduced by the Boltzmann factor given in equation 2.5:

$$I_{electroncollection} = \frac{n_0 e A_{probe}}{2} \sqrt{\frac{2\kappa T_e}{\pi m_e}} \exp\left(\frac{eV}{\kappa T_e}\right) \tag{4.6}$$

With this knowledge, an easy way to access the electron temperature opens up by using the derivative of the total current. This is:

$$\frac{dI}{dV} = \frac{e}{\kappa T_e} I_e + \frac{dI_i}{dV} \tag{4.7}$$

Neglecting the addition given by the ion current and subtracting the ion saturation current from the total current, the I-V trace can be plotted in logarithmic scaling, and the inclination, that directly corresponds to the electron temperature be read off immediately. With the electron temperature known, the floating potential Φ_{float} can be used to obtain Φ_{Plasma}. The prerequisite for the currents to cancel out each other is:

$$\sqrt{\frac{2\kappa T_e}{m_i}} = \sqrt{\frac{\kappa T_e}{2\pi m_e}} \exp\left(\frac{e\Phi_{relative}}{\kappa T_e}\right) \tag{4.8}$$

This happens when:

$$\frac{e\Phi_{relative}}{\kappa T_e} = \ln \sqrt{\frac{m_i}{4\pi m_e}} \tag{4.9}$$

This gives a good way to asses the plasma potential, as the transition from electron collection to electron saturation is no well defined knee that would enable easy determination of the plasma potential. Under perfect theoretical conditions, where the probe behaves that simple, once the probe bias is equal or greater the plasma potential, one should only see the electron saturation current. As this is not the case, the equation 4.9 is convenient to determine the plasma potential:

$$\Phi_{Plasma} = \Phi_{float} + \frac{\kappa T_e}{e} \ln \sqrt{\frac{m_i}{4\pi m_e}} \tag{4.10}$$

4.1.1 Consideration of the probe area

In the previous chapter, the ion current was considered to be drawn to an area equal to the probe area, because the probe dimensions are assumed to be far bigger than the sheath thickness. This however is a simplification that is of use at a first glance only. To achieve more precise results, a look at the relation between the sheath surface and the probe surface is required, as the sheath has to grow when the probe bias is more negative. This kind of treatment is necessary to understand the dynamics of the saturation currents when taking sweeps in NJORD that cover

range of over 80V. The starting point for this is the assumption to drop any contribution from electrons, as the probe is considered sufficiently negative. This gives the Poisson equation for an area A [6]:

$$\Delta\Phi = \frac{-e}{\epsilon_0}\frac{I_{ion}}{A}\sqrt{\frac{m_i}{-2e\Phi}} \tag{4.11}$$

This can be solved to give a value for the sheath thickness by looking at a one dimensional slab only. The complete integration can be found in literature [6] and is not to be detailed here as it is rather lengthy and not highly relevant to the use of emissive probes. It should just be noted that the derivative $\frac{d\Phi}{dx}$ is assumed to be 0 at the sheath edge. The mathematics yield a relation for the sheath thickness closely related to the so called Child Langmuir law for space-charge limited current. The sheath thickness $x_{sheaththickness}$ given by this relation is:

$$\frac{x_{sheaththickness}}{\lambda_D} = \frac{2}{3}\left(\frac{2}{\exp(-1)}\right)^{\frac{1}{4}}\sqrt{\sqrt{\frac{-e\Phi_{probe}}{\kappa T_e}} - \frac{1}{\sqrt{2}}}\left(\sqrt{\frac{-e\Phi_{probe}}{\kappa T_e}} + \sqrt{2}\right) \tag{4.12}$$

This can be used to determine the sheath thickness. Simple geometric approximations then give the relation between the probe of dimension a and its surface area and the actual surface area created via the sheath expansion. For a spheric probe this would amount to:

$$A_{sheath} \approx A_{probe}\left(1 + \frac{x_{sheaththickness}}{a}\right)^2 \tag{4.13}$$

And for a cylindrical probe

$$A_{sheath} \approx A_{probe}\left(1 + \frac{x_{sheaththickness}}{a}\right) \tag{4.14}$$

More drastically strict, numerical solutions have been calculated too, with better attuned assumptions. Comparison with the analytical solution shows, that if considering the fact that in laboratory experiments the accuracy of Langmuir probes is limited by default, the results are fairly close to each other and the analytical solutions are good enough. In practice, another good path to take is to design the probe in a way, that minimizes the impact of the geometry. Noteworthy for example is the switch from a single pin probe to a planar probe with insulated backside and rim. Even stricter and more advanced is the guard ring concept. This takes the insulated planar probe but eliminates the rim effects. It is a planar probe, where the actual probe area is embedded in a ring that is biased at the same voltage as the probe. This nearly eliminates any geometric effects, and thus, influence of the sheath thickness. But it is a relative complex electric setup, that requires perfect matching between the probe and the ring. So, for more complex, RF driven plasmas, this solution again gets less viable.

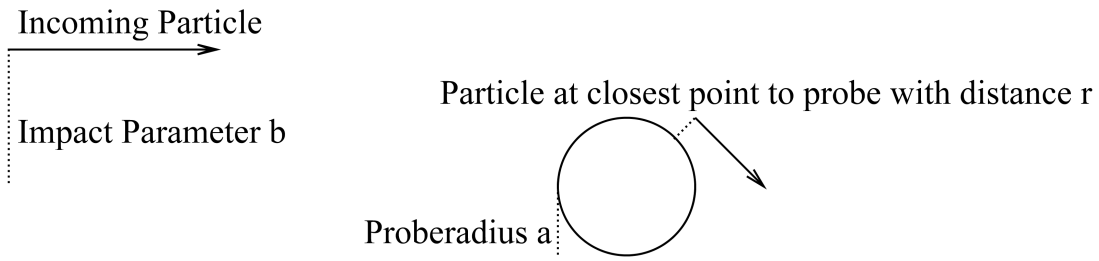

Figure 4.2: Situation sketch of orbit collection

4.1.2 Orbit limited collisonless collection

Another factor to take into account are effects taking place once the probe tip size and the Debye length are on comparable scale, or the probe tip is even smaller than the Debye length. This happens, if very small wires are used to minimize plasma perturbation. The simple approximations for the sheath thickness made in 4.1.1 are not valid anymore in that case, and instead it is necessary to treat this process by looking at the orbits of singular particles. This is done by taking into account energy conservation and angular momentum conservation for a charged particle that is moving towards a biased probe with V_{bias}. For a setup of the situation see figure 4.2. When at a the closest distance to the probe center, the particle is a distance r away and has no radial velocity. Only an angular velocity. This gives the following relation for the angular momentum:

$$mbv_\infty = mrv_\Theta = mr\sqrt{\frac{2}{m}\left(\frac{1}{2}mv_\infty^2 - q(V_{bias} - \Phi_{Plasma})\right)} \tag{4.15}$$

This gives a condition for the parameter b so that the particle will be collected:

$$b \leq a\sqrt{1 - \frac{q(V_{bias} - \Phi_{Plasma})}{\frac{1}{2}mv_\infty^2}} \tag{4.16}$$

Further analysis of this problem is in the realm of theoretical mechanics and analogue to any treatment of a moving particle towards a attracting potential like gravity, with all implications like the potential barrier posed for the radial velocity by the momentum conservation. Detailed treatments about this can be found in most works about theoretical mechanics, and reveal that it is a necessary but not sufficient condition. Considering that, Langmuir devised a way to work around this. Assuming a sheath, it is safe to say that all particles with an impact parameter smaller than the sheath thickness are collected. Integrating a Maxwellian

distribution, this gives for a cylindrical probe the scaling factor:

$$I_{orbitcollection} = I_{saturation} \underbrace{\sqrt{1 + \frac{qV_{bias} - \Phi_{Plasma}}{\kappa T_e}}}_{Orbit\,increased\,current\,factor\,f} \tag{4.17}$$

For spherical probes this relation resolves to:

$$I_{orbitcollection} = I_{saturation} \underbrace{\left(1 + \frac{qV_{bias} - \Phi_{Plasma}}{\kappa T_e}\right)}_{Orbit\,increased\,current\,factor\,f} \tag{4.18}$$

This orbit collection current increase factor has been implemented in the numerical simulations done in parts of this thesis.

4.2 Emissive Langmuir Probe

The standard Langmiur probe can asses a variety of plasma parameters. As outlined before, the accuracy of the data obtained is not the best. The emissive probe can be seen as a specialization of this concept. Several parameters, like density and temperature are dropped, and not obtainable. The one remaining parameter in contrast can be measured with a greater accuracy and precision than it would ever be possible by Langmuir probes. Also, it is, at least in theory, easier to read out the parameter from the data, so that the time to analyze is reduced. The basic idea of an emissive probe is to balance out the currents. In a cold probe, the ion current is very low in comparison to the electron current. By making the probe emit electrons, this can be countered, as emitted electrons from the probe in essence behave like collected ions in the measurement data. In the first iteration of this concept, one could say, the emitted electrons deliver the difference between ion saturation and electron saturation current, so that the floating potential is the same as Φ_{Plasma}. It is not that simple in reality, but the floating potential gets substantially shifted towards the plasma potential. An ideal I-V trace obtained by this concept can be seen in figure 4.3

To construct an emissive probe, one needs a Langmuir probe setup with the ability to heat the probe tip, so that Richardson Emission takes place. With Σ defined as the work function of the material the tip consists out of, this gives a temperature limited current of:

$$I_{e_{Richardson}} = \underbrace{R}_{Richardson\,Constant} T_{Probetip}^2 A_{Probe} \exp\left(\frac{e \cdot \Sigma}{T_{Probetip}}\right) \tag{4.19}$$

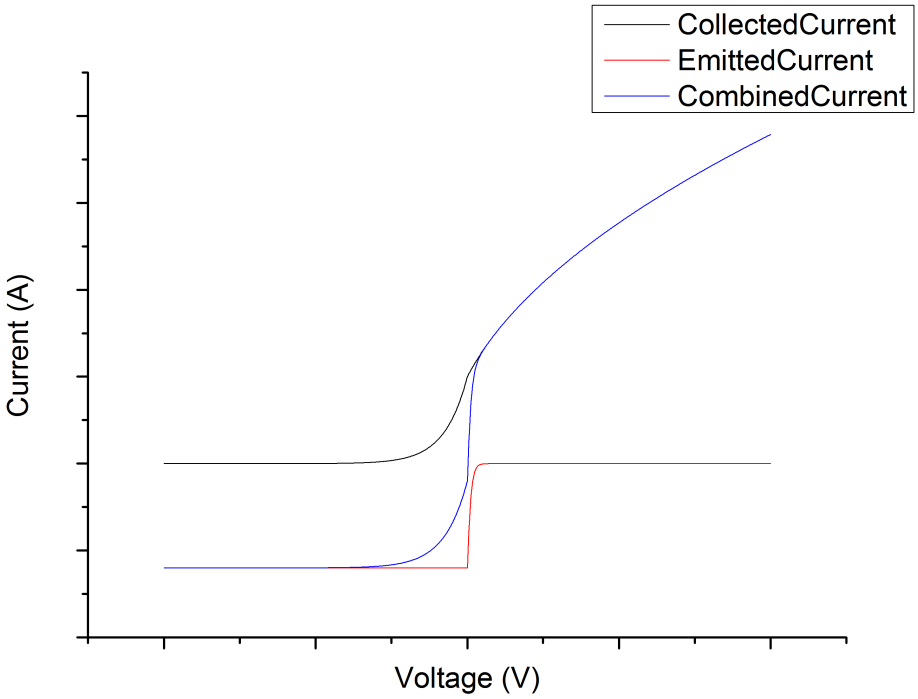

Figure 4.3: I-V Trace for an emissive probe, obtained via the simulation code given in appendix A

The most common way to achieve heating is to just drive a current through some kind of probe tip loop (for details see chapter 5.2). Other methods used by Schrittwieser et al. include systems to heat the probe tip by laser, but are not covered in this thesis. The current drawn by the probe can be separated into two parts. Current drawn when the probe is biased negatively and current drawn when it is biased positively in respect to the plasma. The main equations used in literature [21] are given here, but later (see chapter 4.2.6), other models in use will also be discussed. Here, the ion current is completely neglected, as it is magnitudes smaller than the emitted electron current and as such does not really affect the measurements:

$$I_{totalcurrent} = I_{collected\,electrons} + I_{emitted\,electrons} \tag{4.20}$$

$$I_{collected\,electrons} = \begin{cases} I_{e_{sat}} \cdot \exp\left(\frac{e\Phi_{relative}}{\kappa T_e}\right) & for\ V_{Bias} < \Phi_{Plasma} \\ I_{e_{sat}} \cdot f(\Phi_{relative}) & for\ \Phi_{Plasma} < V_{Bias} \end{cases} \tag{4.21}$$

$$I_{emitted\,electrons} = \begin{cases} I_{e_{emi_{sat}}} & for\ V_{Bias} < \Phi_{Plasma} \\ I_{emi_{sat}} \exp\left(\frac{-e(V_{bias}-\Phi_{Plasma})}{\kappa T_w}\right) \cdot g(V_{bias} - \Phi_{Plasma}) & for\ \Phi_{Plasma} < V_{Bias} \end{cases} \tag{4.22}$$

Note that the factor f is as discussed in 4.1.2

4.2.1 Potential Determination by Separation Point

The separation point technique is historically the first method that was deployed to measure the plasma potential. The thought behind it is rather simple and so far, only a qualitative argument exists, but no quantitative. The idea is, that the I-V traces of a cold and a hot probe only differ in the added part due to electron emission. In the most basic assumption, the emission starts sharply at the plasma potential. So when overlaying both traces taken at the same time and same spot, they should start separating at the plasma potential. In reality however, it is seldom a separation, but rather a crossing, as there are more influences on the emissive probe. Also, as discussed in chapter 4.2.6, the picture of a simple, Heaviside-like step is wrong, leading to a systematic error. Further complications stem from the fact that the probes can not be arbitrarily close in experimental setups, but have to be at a certain distance for mechanical reasons. Adding to that comes the problem that the probes might influence each other and it is difficult to maintain exactly the same voltage on both probes constantly. Combines with the cumbersome heating-setup used in earlier days, this gave the emissive probe the reputation of a diagnostic that is unnecessarily difficult to use for a relative small gain which still resonates in literature like in the book "Principles of Plasma Diagnostics"' [6]

4.2.2 Potential Determination by Floating Point

Another, quick way is through the assumption, that the emitted electrons help balancing the particle flow to the probe. So it is a good first assumption that the floating potential is equal to the plasma potential. This was published first in detail in by Kemp and Sellen [22]. Just driving the emissive probe with a very strong emission current where the floating potential only changes very little with any further increase, however is attached to a small systemic error. Namely the formation of a virtual cathode by the emitted electrons, as not all electrons can escape into the plasma, and thus some form an area of higher space charge and some are also even reflected back into the probe whilst others escape. This process leads to a dip in the sheath potential that forms the virtual cathode, and shifts the floating potential. Further relatively new, thorough theoretical treatments of this process can be found e.g. in papers like Takamura [23] and numerical simulations [24] put the shift at about $1.5 \cdot T_e$. A proposed method to cut down the influence of the error proposed in the paper by Kemp and Sellen is to gradually increase the heating. Two distinct regions are then visible. The region, where the emission is not yet enough to fully compensate and balance out the floating potential to the plasma potential. In this, the floating potential increases rapidly with emission area temperature, which is proportional to the heating current use. In the second region, after a short knee in the curve, the emission is high enough and the floating potential increases only very slowly, as the energy of the emitted electrons changes a bit and thus also the virtual cathode. The proposed method then advises to make linear interpolation of these two regions and look for the intersection, which should be very near the plasma potential. The claim was made that this method is accurate to 0.01 V, which is to be viewed a bit critically, as advanced probe theory predicts that the minimum uncertainty is about 0.2V [21].

4.2.3 Potential Determination by Double Cross

As described in [25], another method is the double cross method. This is compared to all other methods of I-V trace analysis a method that is giving far more data. Namely, T_e and $T_{Probetip}$ in eV as well as Φ_{Plasma}. For this kind of analysis to work however, very strict basic conditions have to be met. Explicitly, this is the demand that the emission saturation current as well as the electron collection current show no no-linear behavior when strongly biased in relation to Φ_{Plasma}, or the nonlinear behavior can be described analytically. For this to happen either a probe with a known geometry is needed or the probe has to be constructed the way to eliminate this geometric influence, increasing the construction difficulties (see chapter 5.2.2). But even with those conditions fulfilled, this would not hold up in a plasma that drives nonlinear I-V trace behavior such as RF plasmas. As such, this method is of

hypothetical interest only for this thesis and included for completeness only. Also, while conducting this thesis it came clear that a secondary electron population exists, rendering the most basic premise of this method invalid (see chapter 6.3). Without attention to detail the method consist of three steps. First, by plotting the deviation of the measured current from a linear interpolation in a logarithmic scale, the electron temperature and the temperature of the emitted electrons can be determined. Then, the crossing of the curve obtained by plotting the deviation from the interpolation with a shifted linear interpolation is determined. In the third step, both crossing points are compared and should give the same potential, which is then presumed to be the plasma potential.

4.2.4 Potential Determination by Inflection Point

The inflection method proposed by Smith et. al. [25] is a development from the double cross method. Owning to its flexibility, precision and robustness towards unexpected physics, it has become the de-facto standard method to determine the plasma potential by emissive probes. The fact used is, that when transitioning from emission to non emission, the governing mechanisms change very abruptly, and as such a peak-like discontinuity should show up. See figure 4.4 for a sketch showing the peak obtained for a simulated probe characteristic after the model in chapter 4.2.6.

Some consideration has to be given to the wire temperature and to space charge effects. It shows that the measured potential is shifted negatively with increasing wire temperature due to this space charge. This shift, however is at the beginning comparatively linear, so this flaw can even be fashioned into a feat. By taking several measurements at different wire temperatures, the measured potential can be plotted against the ratio of emitted current to electron saturation current. Then, a linear interpolation can be done to find the so called *zero emission limit*, which is supposed to represent the true Φ_{Plasma} and theoretical models state the error to be $\approx \frac{T_e}{10e}$ [26]. The use of several data points to interpolate is also statistical helpful in reducing the measurement error. The size of the probe also impacts this method, as smaller heads lead to a steeper curve for the zero emission limit. But as seen later in in chapter 5.2.2, this is a trade off, because smaller heads are also far more prone to burn through. On the other hand, the thicker the wire, the stronger the half width-half maximum value growth with increased heating.

Influence of magnetic fields

It is has to be noted that strong magnetic fields pose problems for emissive probes use via inflection point method, a fact that was already stated when the method was proposed [25]. The for thinner probe wires, the whole potential measured

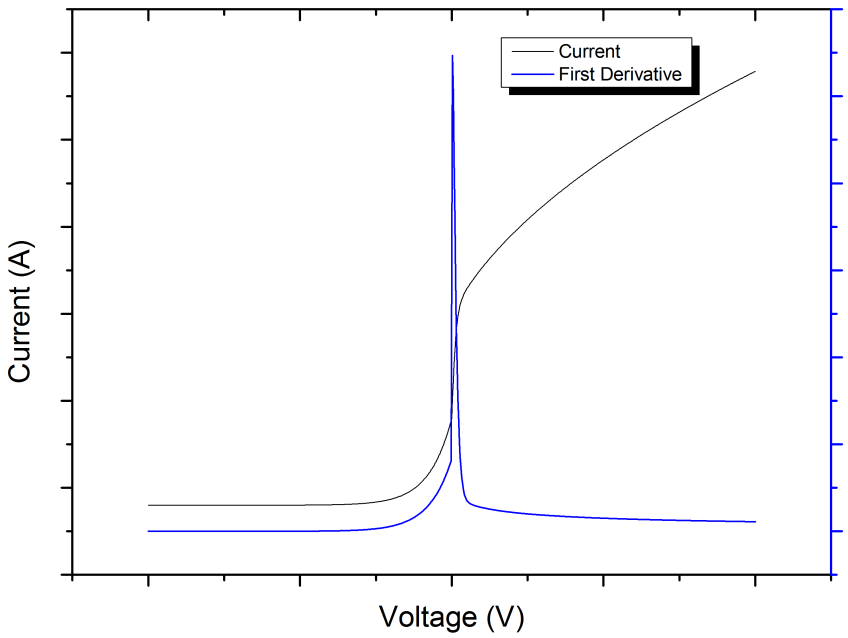

Figure 4.4: Peak obtained when differentiating an emissive probe trace, obtained via the simulation code given in appendix A

shifts downwards, independent of the heating, as the slope of the zero emission line stays more or less the same. For thicker wires however, it might be completly impossible to determine the potential at all. Also, reportedly, with higher magnetic field, the half width-half maximum value is increased and growth stronger for increased heating which has been attributed to space charge effects. Still, no detailed treatment of this problem has been reported [21], only qualitative notes that the problem is rooted in the fact that the magnetic field modifies the effective probe area as electrons that are emitted in a direction perpendicular to the magnetic field get trapped in a gyromotion, which can cause an impact on the measuremend if the probe is oriented along a field line. Also, it is advised to bear in mind that strong magnetic fields can deform the heating filament, if a current is used for heating. From the data published by Smith et al. [25] a rough estimate for the error can be made. For a 0.016 T magnetic field, the Φ_{Plasma} measured seems to be shifted by about 0.2V in the zero emission limit.

4.2.5 Emissive Probes in RF-Driven Plasmas

The RF oscillation has a strong impact on the sheath behavior. This also translates to influence on probe measurements. So, the most important effects are to be illuminated here as they have been treated in the basic paper by Wang et. al. [27]. First, as stated in chapter 3.1.1, the floating potential takes a shift to lower values. For sweep from 0V to 20V RF amplitude the floating potential was reported to shift by 5,2V. Without exact knowledge of the oscillation, it is hard to reconstruct the exact value of the shift. So in RF plasmas, floating emissive probes measurements have to be considered below the actual potential and to be viewed somewhat critically. Also, the rest of the current drawn to the probe behaves non-linearly, as the current bias relations is expanded by an oscillation term in the exponent like in the following:

$$I_{electroncollection} = \frac{n_0 e A_{probe}}{2}\sqrt{\frac{2\kappa T_e}{\pi m_e}}\exp\left(\frac{e(V_{bias} + \Phi_{oscillation}\sin(\omega t))}{\kappa T_e}\right) \quad (4.23)$$

In addition, depending on the chosen model for the emission current, also the current mechanics vary nonlinearly under RF, depending on the instantaneous potential in relation to the plasma potential. In a plasma with a tunable, variable RF oscillation, the proposed solution is to first take I-V traces with and without RF. Those should show a crossing point. Now using a resistor that forces the load line through this crossing point should by theory make the measured trace insensitive to the RF, irrespective to the applied RF. Limits to this methods are plasmas with density changes or when the emission current is to low. Also, in some experiments, like NJORD, there is no way to have a plasma without RF, as

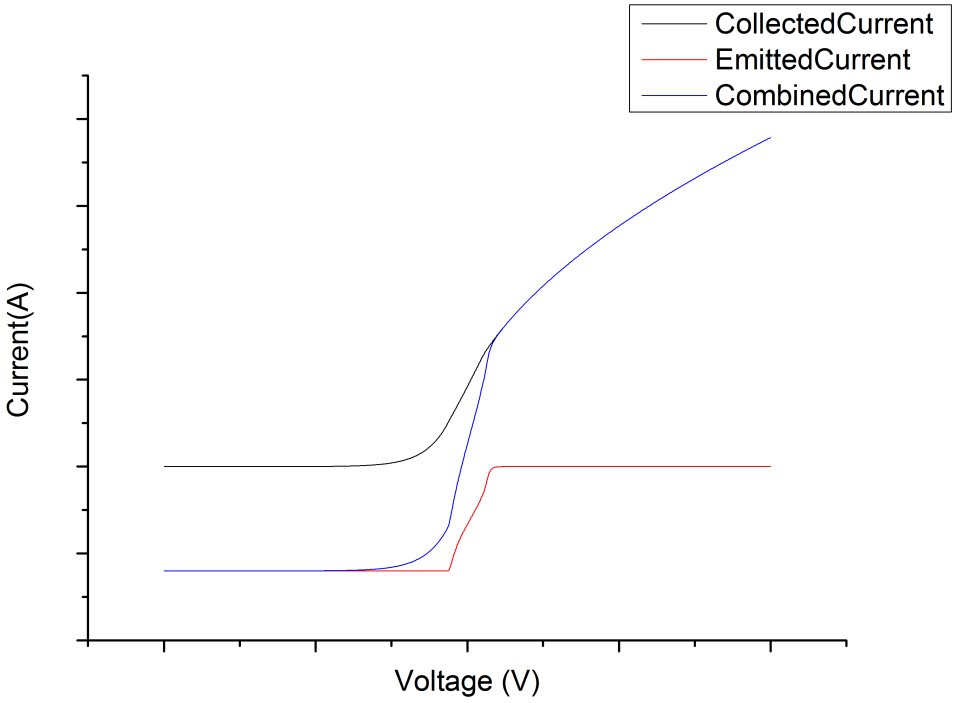

Figure 4.5: An I-V trace with the same parameters as in figure 4.3 but an added RF oscillation of the plasma potential,obtained via the simulation code given in appendix A

the RF is part of the plasma source. For comparison to normal emissive probe traces, in figure 4.5 a trace simulated with the same parameters as in figure 4.3 is given, with only the addition of an RF oscillation of the plasma potential.

Peak Broadening and Double Peaks when using the inflection method

The better method is to again use the inflection point method. The afore mentioned paper [27] reported that the single peak in the derivative separates into two peaks under RF oscillation. The mid point between those two peaks however is the same as the peak in a RF-free plasma. And while the lower peak is not influenced by changes in probe heating, the upper peak is. This one moves towards lower plasma potential with increased heating. The effect is a negative shift in measured potential with increased heating which fits to the peak shift used when applying the the zero emission current method. The broadening between the two peaks is roughly equal to twice the applied RF-amplitude, as will be shown for the two

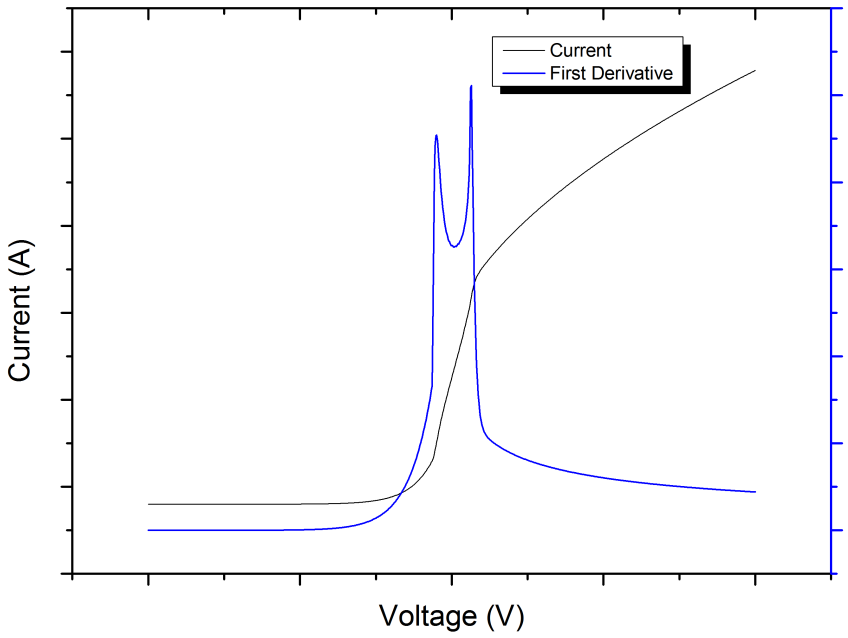

Figure 4.6: Peak broadening in the derivative of an emissive probe I-V trace due to RF oscillation, obtained via the simulation code given in appendix A

simpler emission models. See figure 4.6 for a sketch of how the derivative of the I-V traces broadens.

Numeric simulations done with the model 4.2.6 for this thesis also show that for oscillations concerning of several harmonics, the number of recognizable double peaks not necessary increases proportional with the amount of harmonics present.

Influence of RF-Waveforms

It should be pointed out, that taking midpoint between the two peaks is only a valid method, if the plasma is driven by a waveform that can be considered in good approximation sinusoidal. When the waveform was half wave rectified, the peak ratio changes significantly [27], with the lower peak dominating and the midpoint between the two peaks moved to a higher potential. To have an estimate of how deformed the waveform is, waveform monitoring is advised (see chapter 5.2.5). This can be understood in a more general sense by picturing that taking the derivative gives a histogram of the plasma potential over several oscillations

[28]. And when the driving waveform is imbalanced, this also reflects in how the histogram weighting shifts. Also, the impact strength of this shift on the peak ratio is linked to the RF frequency, as the experiments where carried out in the KHz range and it was stated that an increase in frequency means a behavior more similar to pure sinusoidal oscillations [27]. NJORD operates in the MHz range, so it can be taken to have a near sinusoidal oscillation.

4.2.6 Emission Models

Describing the emission properly is an act of balance between a thorough and correct model and one that is easy to handle when it comes to usability in the laboratory to make predictions while the experiment is running. In this thesis, an intermediate level of description complexity was chosen for all analytical and numerical treatment with an exponential decrease of the emitted electrons. An overview over other models used will also be given.

Heaviside Step

The simplest, yet useful model for emission is that of a step given by [27]. If the probe is below Φ_{Plasma}, the full emission current takes place. If it is above, no emission occurs at all, but the collection saturation current is drawn. If the potential now oscillates with a single frequency amplitude Φ_{osci} around the plasma potential, the average current for the emission can be determined for one full pass. This gives for the current an average over time for an electron emission current $I_{e_{emi}}$ and an collection saturation current $I_{e_{coll}}$:

$$\langle I \rangle = \begin{cases} I_{e_{col}} & for\ \Phi_{osci} < V_{bias} - \Phi_{Plasma} \\ \frac{1}{2}(I_{e_{emi}} + I_{e_{coll}}) + \frac{1}{\pi}(I_{e_{col}} - I_{e_{emi}}) \arcsin \frac{V_{bias} - \Phi_{Plasma}}{\Phi_{osci}} & \\ \qquad for\ -\Phi_{osci} \leq V_{bias} - \Phi_{Plasma} \leq \Phi_{osci} & \\ I_{e_{emi}} & for\ V_{bias} - \Phi_{Plasma} < -\Phi_{osci} \end{cases} \tag{4.24}$$

Taking the derivative gives the required double peak. Another step model is given by Wiebold et al. [28]. Under the assumption that the probe is not fast enough to follow the oscillation, they give a model for the time averaged current that is a bit more smoothed out and is described with a generic current I_0 and another scaling parameter Γ:

$$I(V_{bias}) = I_0 \tanh\left[\Gamma\left(V_{bias} - \Phi_{Plasma}\right)\right] \tag{4.25}$$

For modeling purposes, the parameters have to be set to match the measured values, and this model is more to explain than to give exact predictions. While being set up a little bit different with regard to the basic assumptions, both models fare well in explaining the basic phenomenon of double peaks in RF plasmas.

Smooth Step

A little bit more advanced, but still away from reality, Wang et al. proposed a more realistic model with a smoother transition too [27]. This model too, lacks to include how the electron flux changes due to sheath dynamics nor does it consider any kind of advanced effects discussed in this chapter. So, having the currents $I_{e_{emi}}$ and $I_{e_{coll}}$ again and defining two biases, when the emission and collection saturation is reached, Φ_{emi} and Φ_{coll}. The current in this case is not a step function but described by:

$$I = \begin{cases} I_{e_{coll}} & for\ \Phi_{coll} < V_{bias} - \Phi_{Plasma} \\ \frac{(I_{e_{coll}} - I_{e_{emi}})}{(\Phi_{coll} - \Phi_{emi})}(V_{bias} - \Phi_{Plasma}) + \frac{1}{2}(I_{e_{emi}} + I_{e_{coll}}) & \\ \qquad for\ \Phi_{emi} \leq V_{bias} - \Phi_{Plasma} \leq \Phi_{coll} & \\ I_{e_{emi}} & forV_{bias} - \Phi_{Plasma} < \Phi_{emi} \end{cases} \tag{4.26}$$

Calculating the average for an oscillating potential this leads to the expression [27]:

$$\langle I\rangle = \frac{1}{\pi}\begin{cases} I_{e_{coll}} \qquad for\ \Phi_{osci}+\Phi_{coll} < V_{bias}-\Phi_{Plasma} \\ \\ \int_{\frac{-\pi}{2}}^{\arcsin\left(\frac{V_{bias}-\Phi_{Plasma}-\Phi_{coll}}{\Phi_{Osci}}\right)} I_{e_{coll}}d\Theta + \\ \quad + \int_{\arcsin\left(\frac{V_{bias}-\Phi_{Plasma}-\Phi_{coll}}{\Phi_{Osci}}\right)}^{\frac{\pi}{2}} I(V_{bias}-\Phi_{Plasma}-\Phi_{Osci}\sin\Theta)d\Theta \\ \qquad for\ \Phi_{Osci}+\Phi_{emi} < V_{bias}-\Phi_{Plasma} < \Phi_{Osci}+\Phi_{Coll} \\ \\ \int_{\frac{-\pi}{2}}^{\arcsin\left(\frac{V_{bias}-\Phi_{Plasma}-\Phi_{coll}}{\Phi_{Osci}}\right)} I_{e_{coll}}d\Theta + \\ \quad + \int_{\arcsin\left(\frac{V_{bias}-\Phi_{Plasma}-\Phi_{emi}}{\Phi_{Osci}}\right)}^{\frac{\pi}{2}} I_{e_{emi}}d\Theta + \\ \quad + \int_{\arcsin\left(\frac{V_{bias}-\Phi_{Plasma}-\Phi_{coll}}{\Phi_{Osci}}\right)}^{\arcsin\left(\frac{V_{bias}-\Phi_{Plasma}-\Phi_{emi}}{\Phi_{Osci}}\right)} I(V_{bias}-\Phi_{Plasma}-\Phi_{Osci}\sin\Theta)d\Theta \\ \qquad for\ -\Phi_{Osci}+\Phi_{coll} < V_{bias}-\Phi_{Plasma} < \Phi_{osci}+\Phi_{emi} \\ \\ \int_{\arcsin\left(\frac{V_{bias}-\Phi_{Plasma}-\Phi_{emi}}{\Phi_{Osci}}\right)}^{\frac{\pi}{2}} I_{e_{emi}}d\Theta + \\ \quad + \int_{\frac{-\pi}{2}}^{\arcsin\left(\frac{V_{bias}-\Phi_{Plasma}-\Phi_{emi}}{\Phi_{Osci}}\right)} I(V_{bias}-\Phi_{Plasma}-\Phi_{Osci}\sin\Theta)d\Theta \\ \qquad for\ -\Phi_{osci}+\Phi_{emi} < V_{bias}-\Phi_{Plasma} < -\Phi_{osci}+\Phi_{coll} \\ \\ I_{e_{emi}} \qquad for\ V_{bias}-\Phi_{Plasma} < -\Phi_{Osci}+\Phi_{emi} \end{cases} \tag{4.27}$$

While this is a complicated model that does not even consider any kind of sheath formation or Boltzman retardation, it still fulfills one very important task. It gives an easy modeling understanding into why the potential shifts towards negative value when the heating is increased, and also why this phenomenon is perfectly conserved when using emissive probes in RF-plasmas. When increasing the heating of the wire, Φ_{emi} has to adjust downwards, as with a higher emission also a bigger virtual cathode forms in front of the probe, which required a higher potential pushing the electrons through it. Meanwhile, the collection current and thus the onset potential for this current is not affected. As such, the lower peak, which is determined by Φ_{coll} does not move but the higher peak, which is at $\Phi_{osci}+\Phi_{emi}$ moves towards lower potential, resulting in the total potential shift downwards.

Exponential

The perhaps most common model used for modeling emissive probes is composed of an exponetially increasing collection current and an exponentially declining emission current, as given in [21]. The equation for the collected current with a saturation current $I_{coll_{sat}}$ and geometric factor f as discussed in chapter 4.1.2:

$$I_{coll} = \begin{cases} I_{coll_{sat}} \cdot \exp\left(\frac{-e(\Phi_{Plasma}-V_{bias})}{\kappa T_e}\right) & for\ V_{bias} \leq \Phi_{Plasma} \\ I_{coll_{sat}} f(V_{bias} - \Phi_{Plasma}) & for\ V_{bias} > \Phi_{Plasma} \end{cases} \tag{4.28}$$

Quite analogue, the emission current is defined with a geometric factor g, a wire temperature T_w determining the emission current (see eq. 4.19) and a saturation current $I_{emi_{sat}}$:

$$I_{emi} = \begin{cases} I_{emi_{sat}} & for\ V_{bias} < \Phi_{Plasma} \\ I_{emi_{sat}} \exp\left(\frac{-e(V_{bias}-\Phi_{Plasma})}{\kappa T_w}\right) \cdot g(V_{bias} - \Phi_{Plasma}) & for\ V_{bias} \geq \Phi_{Plasma} \end{cases} \tag{4.29}$$

With no analytical solution given and the nonlinearities making it more difficult to obtain such, numerical simulation was chosen. This model is able to reproduce important phenomena, while being very easy to implement and fast to execute in numerics. The full code is given in appendix A. Whilst comparing with other models and real data, one mistake of this model sticks out. The order of relative height between the peaks in main electron distribution seems to be mirrored. This stems from the fact that in reality and other models better suited to this detail, the potential correlating to full saturation current is negative in relation to the plasma potential and the emitted current onset is at $V_bias = \Phi_{Plasma}$. In the exponential model, this is shifted and the emitted current is fully saturated at $V_{bias} = \Phi_{Plasma}$ while the onset is already at a higher bias. This can be seen as if the onset behavior has been mirrored around Φ_{Plasma} and as such, also the peaks in the derivative trace are mirrored. Knowing this flaw and accounting for it, the model is very useful and fits the observed data very well.

Exact Modelling

The up to date most thorough and complex simulation of the situation in an emissive probe was done by Ye and Takamura [26], and while a lot of thoughts behind it are not fully represented, the mathematics are given for comparison to the other models. The collected current was combined from three currents, an electron emissive current I_{emi}, an electron collection current $I_{coll_{electron}}$ and an ion collection current $I_{coll_{ion}}$ and the whole calculations where carried out for a cylindrical geometry. The emissive current was broken down into three distinct regions. One region

where it is zero because the probe is biased above the plasma potential, one region where the current is governed by space charge effects, and one where it is governed by temperature limit. In the temperature limited region $I_{emi_{T-Region}}$ it is simply the current given by Richardson emission discussed previously in the Richardson equation 4.19. In the space charge limited region, the current, $I_{emi_{S-Region}}$ was derived by enforcing that the electric field on the probe has to be zero and gives:

$$I_{emi_{S-Region}} = 0,5 \cdot G(1+G)^{-1} e n_{e_{sheathedge}} \sqrt{\frac{8T_e}{\pi m_e}} \sqrt{\frac{e(V_{bias} - \Phi_{Plasma})}{\kappa T_e}} \tag{4.30}$$

With:

$$G = \frac{-\beta_1 + \sqrt{\beta_1^2 - 4\beta_0\beta_2}}{2\beta_2} \tag{4.31}$$

And a normalized sheath voltage:

$$N = \frac{e(V_{bias} - \Phi_{Plasma})}{\kappa T_e} \tag{4.32}$$

Using the definitions:

$$\begin{aligned}
\beta_0 =& -4\,(N)^2 - 2N(F^2 - 2F) && (4.33)\\
\beta_1 =& 4(-2F-1)\,(N)^2 + 8F \cdot N - F^2 && (4.34)\\
\beta_2 =& \,(N)^2 - 8\,(N)^3 && (4.35)\\
F =& \exp((N)) - 1 && (4.36)\\
& && (4.37)
\end{aligned}$$

The potential Φ_s at which the transition from S-region to T-region takes place is simply defined as the the value V_{bias} fulfilling $I_{emi_{T-Region}} = I_{emi_{S-Region}}$ and is as such depending on the probe temperature. The ion current is given by:

$$I_{coll_{ion}} = \begin{cases} -e n_{i_{sheathedge}} \sqrt{\frac{1+g}{1+\frac{g}{2N}}} v_s A_{probe} & for V_{bias} < \Phi_{Plasma} \\ 0 & for\ V_{bias} \geq \Phi_{Plasma} \end{cases} \tag{4.38}$$

With g a parameter depending whether V_{bias} is above or below Φ_s:

$$g = \begin{cases} \frac{I_{emi_{T-Region}}}{e n_{i_{sheathedge}} \sqrt{\frac{8T_e}{\pi m_e}} \sqrt{-0,25\pi N} - I_{emi_{T-Region}}} & for\ V_{bias} < \Phi_s \\ G & for\ \Phi_s \leq V_{bias} < \Phi_{Plasma} \end{cases} \tag{4.39}$$

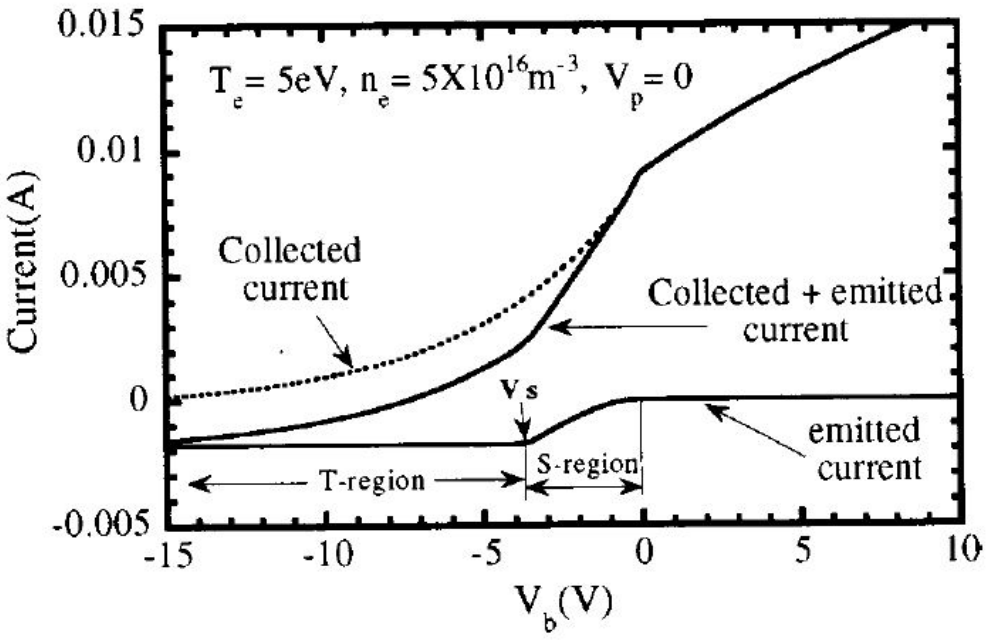

FIG. 1. Ideal emissive probe current is composed of two parts, collected current and emitted current. *T*-region in the $I-V$ curve is characterized by the temperature limited current. In *S*-region the emissive current is determined by the space-charge limited condition.

Figure 4.7: I-V Trace with exact modelling, taken from [26]

With the electron saturation current given as $I_{electron_{sat}} = \frac{1}{4} e n_{sheathedge} \sqrt{\frac{8T_e}{\pi m_e}} A_{probe}$, the collected electron current $I_{coll_{electron}}$ is expressed as:

$$I_{coll_{electron}} = \begin{cases} \frac{I_{electron_{sat}}}{1+g} & for\ V_{bias} < \Phi_{Plasma} \\ I_{electron_{sat}} \sqrt{1 + \frac{e(V_{bias} - \Phi_{Plasma})}{T_e}} & for\ V_{bias} \geq \Phi_{Plasma} \end{cases} \tag{4.40}$$

As long and over the top for application in the laboratory this model seems on the first glance, it delivers a very important insight into the boundaries of precision and accuracy of emissive probes. Also, with this model, the limiting conditions can be determined, for which useful emissive probe characteristics are obtainable. The model predicts, that the inflection point methods underestimates the plasma potential by $\approx \frac{T_e}{10e}$. A graphic of an I-V trace calculated with this model is shown in figure 4.7.

Chapter 5

Experimental Setup

In this chapter the peculiarities and design specifications of the NJORD experiment as well as considerations about the construction of plasma probes are presented. RF-driven plasma-sources are a common sight in laboratories around the world, but lack a level of standardization so that direct comparison between the sources is often made difficult by differences in design and dimension. In the case of NJORD, the most similar devices are the Chi-Kung [20], Wombat [12] and Piglet [29] operated by the ANU. This chapter consists of three parts: an overview of NJORD, emissive probe operation and retarding field analyzer operation.

5.1 NJORD

NJORD consists of several parts of distinct function. A rough overview over the specifications and physical principles is given here. A schematic drawing of NJORD is given in chapter 3.4 with figure 3.5. The exact measurements for dimensions of the vessel and further technical details can be found in the Tribulato master thesis [30]

5.1.1 Vacuum-System

The vacuum system consist of two parts. First, a pump system is in place to create the necessary pressure range for experimental operation coupled with a controllable gas inlet to fill the chamber with a known gas mixture. Second to be describe is the vacuum gauges and monitoring system to enable reproduction of the same conditions repeatedly and to enable calculations for comparison, as in chapter 2.1, pressure and density have already been noted as fundamentally important.

Pump System and Gas Inlet

In general, two main principles can be used to create lower pressure as stated in [31]. Those two principles are compression pumps, that remove gas from the area to be pumped down via mechanical means or a momentum change, and getter pumps, that condense, adsorb or absorb the gas. In NJORD, only pumps of the first type are used, so no large explanation is given about the later type, that includes pumps with extremely large absorption areas and cryopumps that freeze out the remaining gas via condensation.
There are several pumping mechanisms, and each of them has its specific work range for its intake and output. Hence the vacuum system has to be made up from different pumps, that work in stages. First, one or several roughing pumps creates a prevacuum. Only in this prevacuum, the high-vacuum pumps can operate, as the principles guiding the pumping mechanism are very susceptible to too high pressures (for example, condensation pumps would cover up extremely fast and in turbomolecular pumps the friction becomes too large, which can damage the rotor mechanism).
In NJORD the system consists of a turbomolecular pump and an rotary pump to provide the prevacuum. The principle of a rotary pump is a two step mechanism. In the first step, the certain volume is opened up to allow gas from the inlet side to flow in. Then this section is sealed off and the volume compressed towards the exhaust. There are several geometrical configurations to utilizes this, ranging from the Gaede rotary mercury pump of 1905 to more evolved designs like the trochoid pump. The used pump is a rotary-vane pump. Two extending vanes provide sealing to the area that is first opened up to the inlet and then compressed outwards through the exit. A schematic drawing of this concept can be seen in figure 5.1. It is worth noting, that to make the sealing better and to keep the pump system lubricated, the whole pump-body is immersed in oil. This makes it necessary to have a shutter between the rotary vane pump and the turbomolecular pump. Once the turbomolecular pump is switched off, the shutter is closed to prevent oil from polluting the experiment chamber. In NJORD, this shutter is pressure operated and directly connected to the computer controlling the pumps, making the closure automatic and instantaneous once the turbomolecuar pump is switched off.

Utilizing such kind of a pump, it is easy to reach the pressure range of $10^{-1}mbar$, also called a *rough vacuum*. From that range on, turbomolecular pumps can be run. The principle behind turbomolecular pumps is not compression and exhaustion but rather a continuous change of momentum for every particle that hits the pumps fans. Several fan-blades in a tower-like row change the momentum more and more downwards. The blades are separated in the rotor-set used for the active act of molecule removal and the stator-set for guidance, like in most turbine

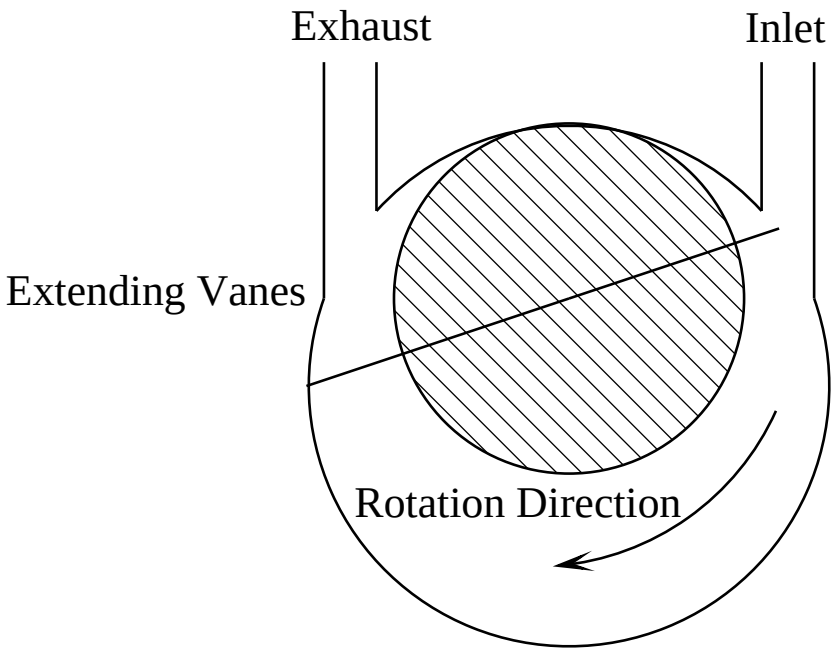

Figure 5.1: Simple schematic of the rotary vane pump principle

like arrays. Trying to hit particles moving at thermal speed requires fast moving fan-blades. A simple calculation from [31] gives a good estimate for the minimum rotation frequency needed for this pumping system to work properly. A molecule at room temperature moves with a speed in the vicinity of $500\frac{m}{s}$. An ordinary turbo pump has a radius of something near 5cm. For the blades to rotate with this speed, simple math gives a frequency of 1,6 kHz, which translates to about 90000 revolutions per minute. These high speeds require special magnetic bearings to reduce friction. Also, for this concept to work properly at gas removal, the gas flow has to be in the molecular range to be dominated by the interaction between walls and the gas particles. This is expressed in the Knudsen number, which is defined as $K_n = \frac{Mean\,free\,path}{characteristic\,dimensions\,of\,system}$ being above unity. A quick check at NJORDs pressure measurement setup while under full operation and a measurement of the inlet diameter yields a Knudsen number above one. So, this condition is clearly fulfilled.

Measurement System

There is a wide variety of measurement methods available to determine the pressure. In this work, only the systems used in NJORD are described. The principles applied in vacuum gauges can be generally separated into two categories apart

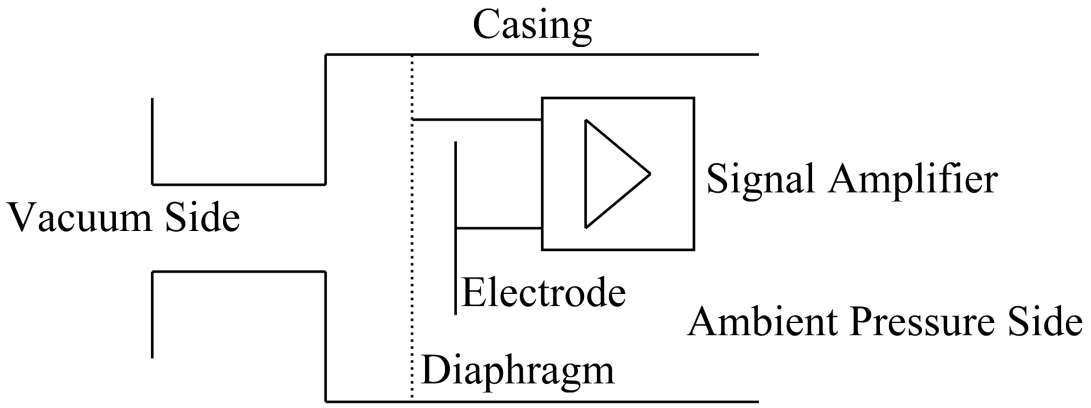

Figure 5.2: Schematic of a basic capacitance vacuum gauge

from the different ranges they operate in. First, there are systems that deliver a pressure reading independent of the gas in which the gauge is measuring. A second class are systems with readings dependent on the type of gas.
In NJORD, one gauge of the first type is installed, a capacitance manometer. This consists of a diaphragm facing the vacuum, and an electrode behind it. Diaphragm and electrode together form a capacitor. As the diaphragm bulges due to the pressure difference, the capacitance changes, and this can be read out as the pressure. The principle of construction is also detailed in figure 5.2. The advantage of this gauge is the fact that it is completely independent of the gas used. The downside is that this principle can be applied until $10^{-4}mbar$ is reached but not further, as it grows inaccurate at lower pressures. It is the only independent method to be able to measure at such low pressures, but in NJORD, experiments are conducted at pressures between from $1,3 \cdot 10^{-3}$ down to $0,24 \cdot 10^{-3}mbar$, so the validity of measurements given is to be questioned, especially considering the fact, that the used device, a MKS Baratron, is only rated down to $0,27 \cdot 10^{-3}mbar$. So the lowest pressure measurements are out of range and this makes the Baratron more useful to ensure proper reproducible conditions in the experimental chamber at higher gasflows.

Of the gas type dependent gauges, NJORD has a Boc Edwards WRG-S. This is a sophisticated wide range gauge utilizing two different concepts to cover a larger range. Further, a micro controller automatically switches between the gauges and normalizes the readings into a voltage that can be converted to an accurate pressure reading and also displayes a detailed error code in case of malfunctions. The first step for pressure ranges between 1013 mbar and $10^{-4}mbar$ is a thermal conductivity gauge. The notion behind this concept is that the heat conductivity of

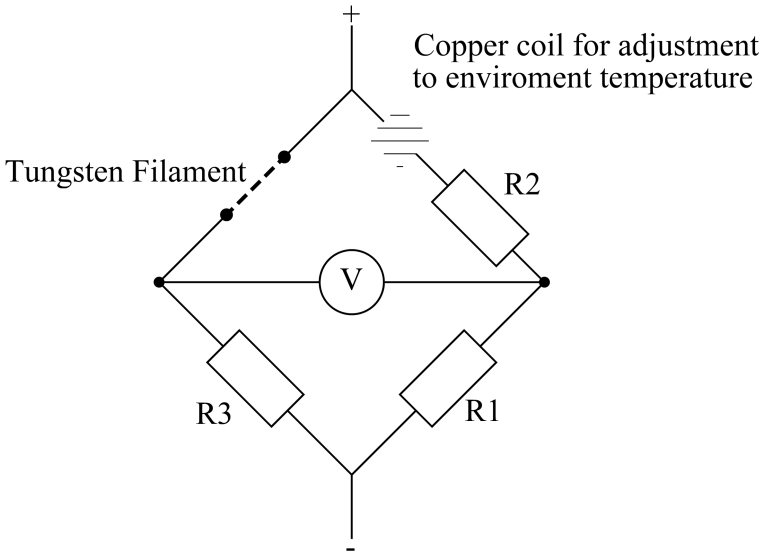

Figure 5.3: Schematic of a Pirani gauge

a gas can be seen as reasonably constant until the gas is showing molecular flow. At this point, it drops rapidly and in relation to the mean free path length. This continues until the mean free path length is larger than the distance from the hot source to the cold, where it is constant again, as it is now dominated by radiation and heat conduction through the connection of the hot source. In gauges of the Pirani type this is used by constructing a Wheatstone bridge as shown in figure 5.3. The bridge is alway kept balanced, which means that the temperature is kept constant irrespective of the heat loss taking place. The change in voltage required to do so is correlated to the pressure inside the gauge. This method allows us to measure from 1013 mbar down to $10^{-4}mbar$, with the constriction that the measurement uncertainty change strongly over this range. The best range for application is between 1 mbar and $10^{-3}mbar$. Also, after obtaining the pressure on a scale calibrated for an Oxygen-Nitrogen mix as in air, it has to be converted into the corresponding pressure in the used operating gas, like Argon. For this, calibration curves are available from the manufacturer.

The second gauge included is a cold cathode in the inverted magnetron configuration. The basis is a self sustaining discharge between two unheated electrodes. And the current running through the discharge links a given voltage to pressure as it is proportional to the particle density. There is no electron source,so the initial charge has to be randomly created by cosmic radiation or radioactive decay or in the WGR-S, a separate striking filament to supply the initial electrons. The

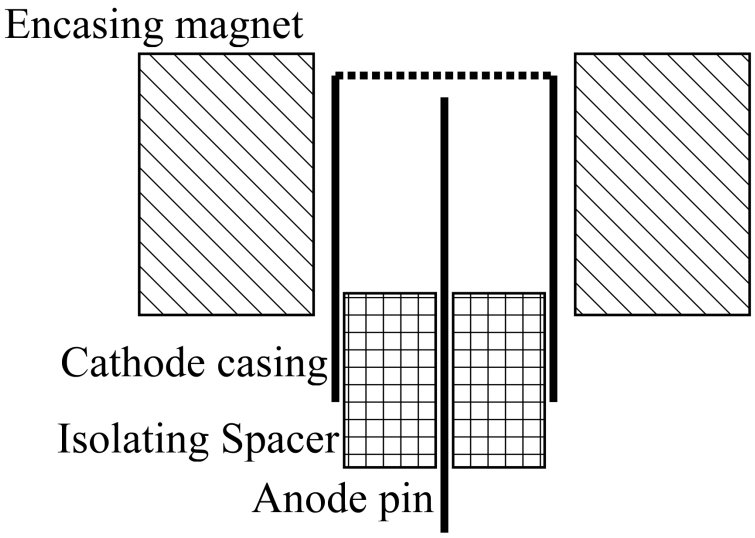

Figure 5.4: Schematic of a Cold Cathode in inverted magnetron setup

geometry consists of a strong magnet encasing the whole setup. Inside this magnet is an outer cathode, then to reduce the influx of field emission electrons some kind of ceramics spacer and finally an anode pin. See figure 5.4 for a schematic drawing. The strong magnetic field forces the charge carriers on a gyrating orbit. The added electric field, which is perpendicular to $\vec{B}$ for the most part of the gauge this creates an $E \times B$ drift spiraling around the anode pin, increasing the chance of collisions to keep up the discharge. Between the electrodes several kV are applied to keep the discharge up, limiting the use in higher pressure ranges, as the discharge would change into a glow discharge that has only a very weak dependence on the pressure. So, usefull operation should only begin in the vicinity of $10^{-2} mbar$. The inverted magnetron, as a special case of cold cathode geometries can be used to measure down to the ultra high vacuum regime of $10^{-11} mbar$ without any bigger loss of precision, even though trying to start the gauge discharge unassisted might take hours up to days. In addition, it is an easy, robust principle, resistant to mechanical shocks and sudden air intake that is not to costly to install. Sadly, the cold cathode suffers from one big drawback. The principle of operation is the same as that of an ion sputter pump with pump rates up to $10^{-2} \frac{l}{s}$ [31]. As such, first of all, the gauge acts as such and can show significant pumping speed because discharge ions are retained in the cathode wall and also because sputtered cathode material acts as getter particles. This leads to a high inaccuracy in the measurement, that can amount up to 50%. Also, like the Pirani gauge, a calibration for the the different kind of gas used is necessary. Further, as it is a discharge to be measured, this gauge should not be facing the plasma directly to avoid drawing

Ar flow in sccm	WRG-S , for O_2N_2 in 10^{-3} mbar	for Ar in 10^{-3} mbar	MKS B. in 10^{-3} mbar
1,2	0,14±0,07	0,11± 0,04	0,25
1,5	0,27±0,135	0,22± 0,1	0,31
2	0,54±0,27	0,48± 0,21	0,39
2,5	0,8 ±0,4	0,74± 0,34	0,5
3	1,1 ±0,55	1,05± 0,49	0,6
4	1 ±0,5	0,94± 0,44	0,77
5	1,1 ±0,55	1,05± 0,49	0,99
7	1,1 ±0,5	1,05± 0,49	1,38

Table 5.1: Conversion table between gas flow and pressure

current from the plasma, and is installed in a small setup slightly removed from the main chamber.

For the WRG-S the calibration data to convert from shown pressure (which is the pressure for a O_2 N_2 mixture) to the pressure that is prevalent in the chamber with Argon was supplied by the manufacturer. From this the graph 5.5 was calculated. The fitting power relation between the pressures in mbar is found to be:

$$P_{Argon} = 2,1424 \cdot P_{O_2\ N_2\ Mix}^{1,118} \tag{5.1}$$

Note that arround 10^{-3} mbar,the system switches from Pirani to cold cathode system, as the pressure relation show a knee that is not visible when looking at the calibration graph between pressure and gauge output voltage. As such, the power law can be seen as systemic error source in that region, due to lack of finer data for calibration.

The gas flow into the experiment chamber is regulated through an automated flow controller. A flow rate can be chosen, so that the system goes into a pressure range, where an equilibrium between gas flow inwards and pump speed is created. As it is simpler to use the gas flow that can be set directly by PC, a conversion table between gas flow and pressure is given here. When the experimental data is analyzed, only the gas flow is given for convenience reasons. A variety of different gas types can be selected for experimentation, albeit in this thesis only argon was used.

This table also shows how the ranges detailed before are behaving in experimental operation. In the area of $10^{-4}mbar$ the wide range seems to operate the cold cathode with evenly spaced pressure steps, and the capacitance seems to jump in its pressure steps. Upon reaching a gasflow that results in a pressure around

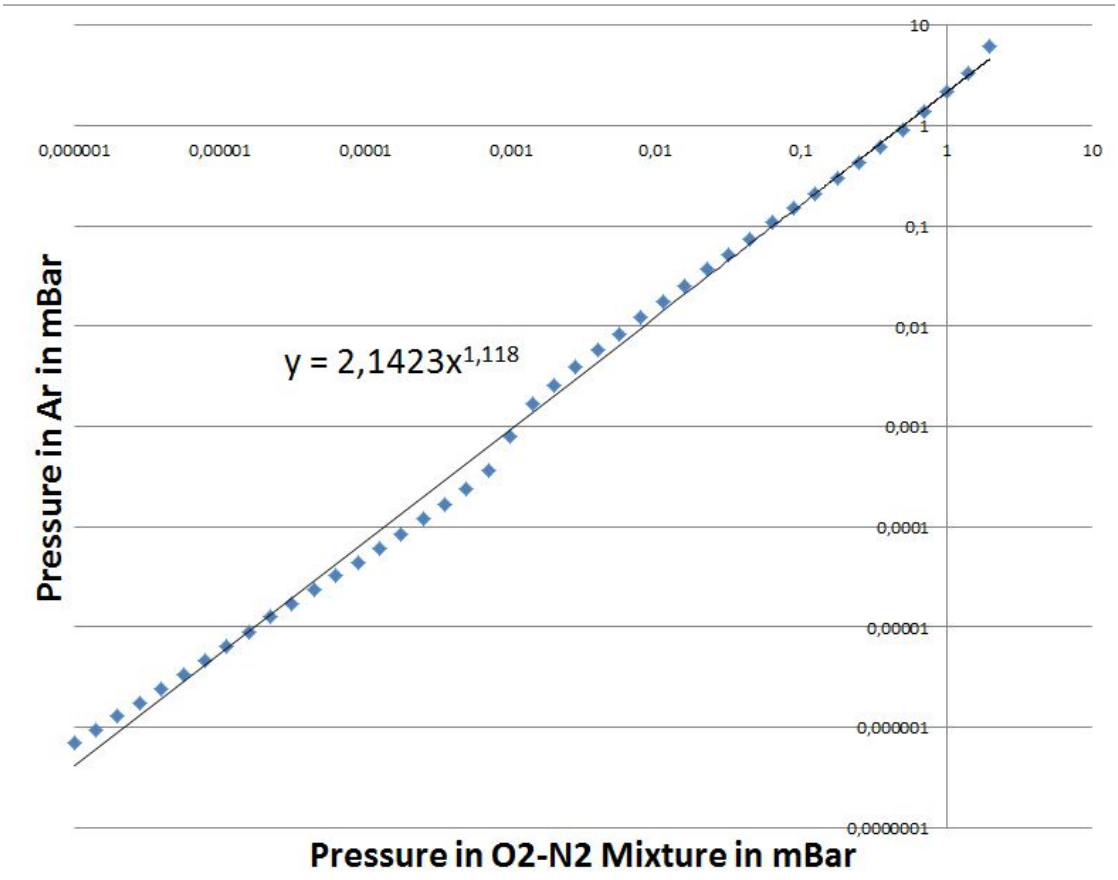

Figure 5.5: Pressure conversion graph for Boc Edwards WRG-S between Air Mixture and Argon

$10^{-3}mbar$, however, the wide range gauge seems to switch to the Pirani system and does not show any change at all. The capacitance principle reaches the range for which it was designed and the pressure steps are evenly spaced.

5.1.2 Source Region

There are several plasma generation concepts. One major category is sources that inject charge carriers and accelerate them to ionize the background gas and the other one is the group of sources that use existing charge carriers from ionization through e.g. cosmic radiation or a radioactive decay source and apply strong oscillating fields to those [32]. NJORD is of the latter type and its source consists of magnets to create a B field to enable helicon modes to propagate as discussed in chapter 3.3 and a RF antenna.

Magnetic Field Coils

NJORD has several coils to create the desired magentic fields. Two coils in the source region and three coils in the expansion chamber. The expansion chamber coils have not been used in this thesis, as too strong magnetic fields pose a problem (see chapter 4.2.4). The source coils consist, starting from the gas inlet, of a coil with 525 windings and a second coil with 550 windings. The wire used has a diameter of 2mm, and as such, the physical extention of the coils has to be considered, rendering the classical approximative coil formulas imprecise. To determine the magnetic field on the center axis, a numeric code is employed. In this thesis, both coils were run at 5A for all experiments, giving the magnetic profil in figure 5.6. Detailed simulations for other current configurations are available [30].

RF-Source

The NJORD RF source is a RF antenna in what is known as Boswell or saddle type antenna. For the basic geometry see figure 5.7. This antenna is designed to evoke a helicon wave in a field configuration known as m-1 mode. See 3.3 for further details. The length in z-direction determines, which kind of ξ-modes can and will be evoked. The antenna is driven by a setup of several radio frequency amplifiers. A small signal with a frequency of 13,6 MHz is created by a waveform generator and guided through several amplification steps until it is finally coupled to the antenna. The antenna is connected via two variable capacitors, to minimize reflectionl. It is necessary to ensure good coupling of the RF signal to the plasma and prevent to0 much reflection back into the amplifier stack, as it could damage them. Also, over the course of an experiment, especially short after having initiated the plasma discharge, regular checks of the refections are of importance, as the coupling can

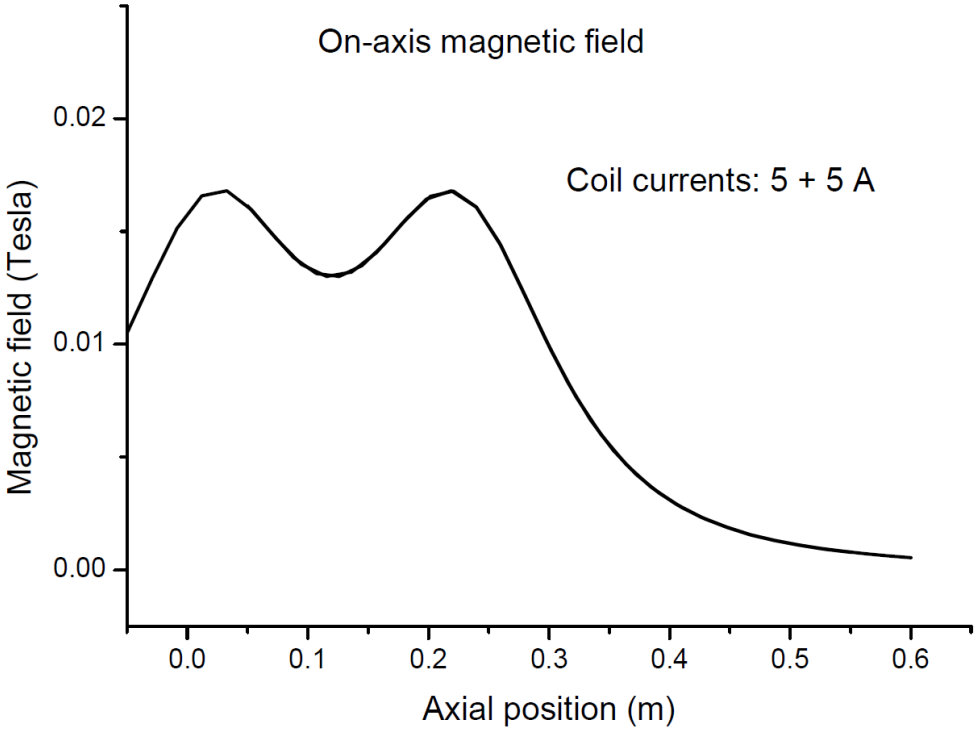

Figure 5.6: Plot of the magnetic field strength along the center axis in the source of NJORD. Sourcecoils set to 5A current,

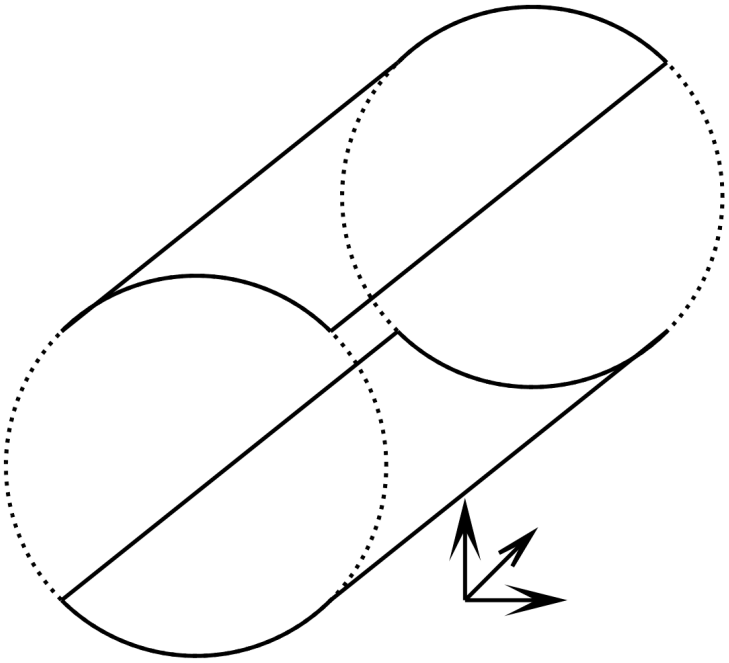

Figure 5.7: Geometry of a saddle type antenna

change a bit as the experiment runs. The amplifiers can provide a RF-wave with a power from 300W to 1kW. Under normal operation with 600W a minimum of about 5W are reflected back. For further details of the RF setup see [30].

5.2 Emissive Probe

5.2.1 Electric Setup

Historically, the emissive probe underwent a pragmatism shift in construction. In earlier days, the dominant design was one where a sinus waveform current was used to drive the heating. One half-form of the current would be used to heat the probe tip, while the other half was held back by use of a diode and the measurement was taken in this short window. The major problem with this approach is the fact, that for a plasma not dense enough, the current drawn when taking the I-V traces is not strong enough to keep up the temperature, thus resulting in a drop of temperature while measuring. Modern-day setups circumvent this problem.

As shown in figure 5.8, the heating is continuously provided by the heating circuit. Attached to this circuit is between two resistances an exemplary Langmuir probe setup to take the I-V trace. When the resistances for taking the measure-

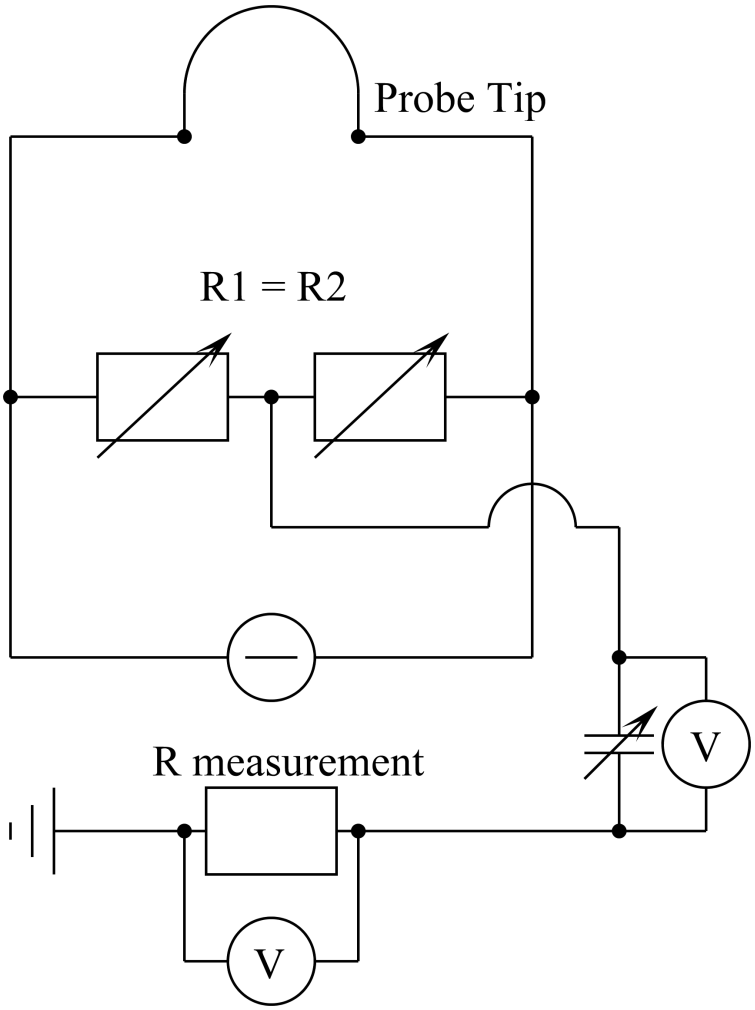

Figure 5.8: Schematic of the heating setup used and a simple setup to take I-V traces

ment are balanced properly, only a minimal current runs to the ground and the applied voltage bias corresponds to the middle of the probe tip. By increasing the bias voltage on the connection from the ground, the whole circuit is biased. Then, a current can be drawn from probe tip to ground. This setup enables a continuous heating, so that the problem of dropping temperatures and short time frames to take a measurement are avoided

The probe data is sampled via an automated system. The probe is biased at a certain voltage, the current then sampled and then the process repeated. In this thesis, 201 samples were taken per bias voltage before moving on to the next bias voltage. In a second automated step, the average of those 201 samples is taken. This serves to compensate for the noise that would occur without averaging. Methods to compensate for the RF noise include compensation circuits, that filter out the main RF frequency and some higher harmonics. In addition, some probe rods are shielded against the RF influence on the wires leading up to the tip by a metal casing. After one bias has been saved to disc, the next bias voltage is set and the process repeats. The Labview program is set to take 201 evenly spaced steps between the minimum and maximum bias voltage. This is done for the whole sweeping range and afterwards saved in a txt file containing all measurements. If set, afterwards a step motor moves forward and repeats the measurement process. Although full radial profiles over the entire diameter were taken, only the positions when moving up to the center where considered for further analysis, as a quick preliminary view revealed that after moving through the center the probe seemed to influence the plasma significantly and a constant distortion in the derived traces could be observed. Dropping this data should amount to no information loss, as the experiment is rotational symmetric around the center axis. It can be further argued for this drastic measure of dropping half the readings, when looking at the measurements performed by Takahashi and Charles [33] on the CHI KUNG device, which has the same geometric layout and antenna setup as NJORD. They show exactly the same "drag along"' effect, that distorts the profile in a way that is difficult to bring into overlap with a source that is cylindrically symmetric. To get the maximum data within the range of a proper system response of the sweeping voltage source, the whole probe bias voltage was shifted upwards with respect to the ground via a battery box consisting of several batteries connected in a row. This is necessary, because Φ_{Plasma} was anticipated to be in the area of 50V to 70V while the voltage source could only sweep from -60V to 60V. The battery shift voltage was measured and added to all bias voltages afterwards.

The way of averaging is easy to implement, but bears the danger of a small systematic error when determining the bias voltage of roughly up to 1,5V (see chapter 5.2.5 for measurments of the oscillation amplitude). The explanation lies in the beat between the frequency of measurement and the RF-oscillation. If the mea-

surement on average takes place more often when the potential is raised above the set bias voltage than below, the whole measurement can be seen as shifted upwards. The huge difference between the the two frequencies as well as the fact that the RF-oscillation can be made up of several strong harmonics, whose composition change between measurements, further complicates this problem. So far no easy laboratory applicable solutions is found, so that for all measurements this systemic error is always assumed to be maximal, which is probably an overestimation.

5.2.2 General Considerations in Probe Design

But also the design of the probe tip and rod needs some consideration, as not every design is viable. Several factors have to be taken into account and balanced against each other. The criteria used to compare the two designs tested in this thesis had to fulfill the following points:

- Easy to manufacture, as it is not uncommon that a probe tip burns up and has to be replaced.

- Mechanical stability, because there is some vibration and tugging while inserting the probe as well as when it is moved by the step motor. Also, heating produces some mechanical stress on the probe.

- Precise control over the length of wire that is heated. Else, unwanted heating in the probe tube is to be considered. Those two last points make the method of friction connection, that is often used for quick probe setups, unfavorable.

The heating filament of choice was in both cases a 0.125mm diameter Tungsten wire. Thicker wires are more robust and last longer in plasma thrusters. Thinner wires produce a steeper slope when interpolating the true plasma potential via the zero emission limit method (see chapter 4.2.4) [25] . The chosen wire strength has shown itself as a good compromise between these two requirements in the laboratory. Also, the shape of the head has some influence. Again, the same shape was chosen for both probes, the commonly used hairpin-style, as shown in figure 5.9. This is by far the most widely used shape as it excels in ease of fabrication. Nevertheless, some limitations should be remembered. First and foremost, the hairpin is becoming unreliable once the radius of the bend is within range of r_L. Also, a U-turn is quite a step removed from the underlying probe theory assumption of

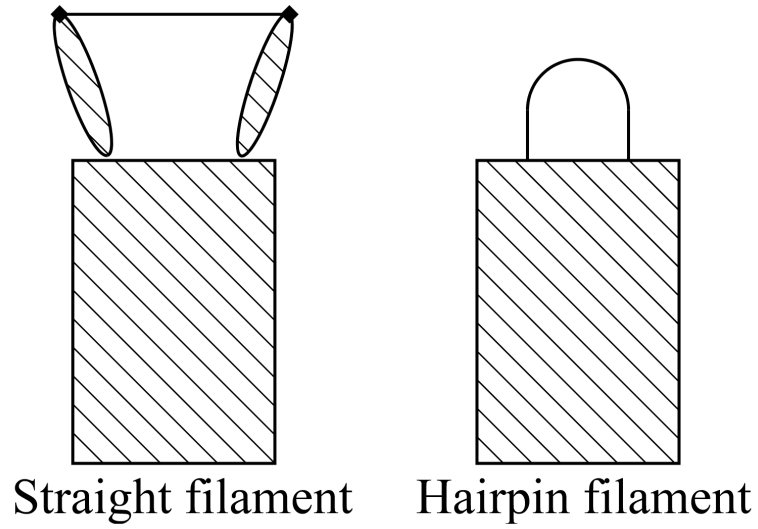

Figure 5.9: Hairpin and Straight Shape for Probe Tips

a cylindrical probe head. The lower the density of the plasma the more impact those effects have, up to an error of 0,2V in a plasma density of $10^6 cm^{-3}$. At last, the spatial resolution suffers under the more complex shape of the probe tip. A probe tip that is closer to the basic assumptions is the straight wire as introduced in the paper by Kemp and Sellen [22], which eliminates this unfavorable geometric attribute and gives a far higher spatial resolution. The problem with this design is its higher complexity when fabricating it and the fact that the mechanical stress due to heating coupled with the increased brittleness of a Tungsten wire after heating, that the probe will break after one use (unless one curves the wire again). This way it stays more of a concept in comparison to the hairpin design until an easier way to fabricate it is devised.
The wire leading up to the tip was in both cases a Nickel wire of 0.5mm. Nickel is easy to solder, a fact that make the connection of the probe end to the Lemo plug far easier. The size of the Lemo plug connection area as area to solder in while avoiding strong mechanical stress to the probe tip so it does not break, already amounts to a mechanical task of certain difficulty, without an "unsolderable" wire as added obstacle. The diameter ratio between the two wires ensure, that the biggest voltage drop is only over the Tungsten tip part.

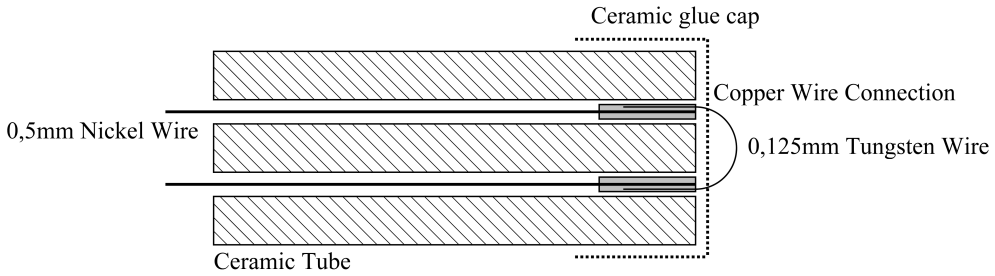

Figure 5.10: Schematic of first used Probe Design

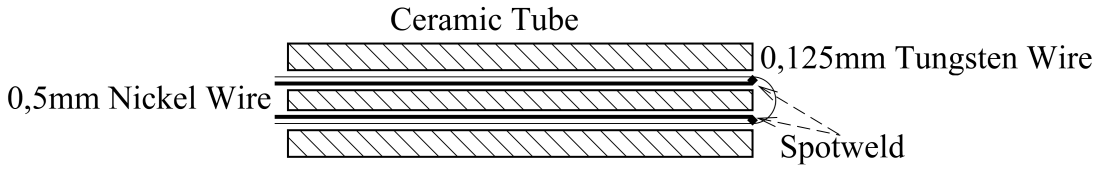

Figure 5.11: Schematic of the second used Probe Design

5.2.3 First Design

The first design, shown in 5.10 is in resemblance to the design published by Siebenforcher and Schrittwieser [34], in which the connection is made by a Copper braid wire. In addition, a cap of ceramic glue was added. This was supposed to prevent any contact between the ends of the Copper braid and the plasma, as the ends are very thin, fine tips. Those very fine, pronounced ends could build up significant charge when the probe bias is applied. The probe design proved not viable due to two main reasons. The probe showed unpredictable behavior when heated, leading to jumps in the heating current needed. Further, and far more grave was the response of the ceramic glue to the attempts to heat. Every probe showed cracking in the ceramic glue cap that had enough force to destroy the tip. After several tries, this design was abandoned as no other way to fabricate a cap was within reach.

5.2.4 Second Design

The second design proved easier to fabricate and mechanical more stable, and has in akin ways been used since 1966 [22]. To understand details of the design in figure 5.11, it seems in order to describe the fabrication process in little more detail. First, a long stretch of the thin Tungsten wire is inserted into the ceramic tube and the tip is shaped by pulling it down until only the hairpin tip of intended size is visible. Then the two Nickel wires are shoved down the tube hole from the

tip direction, while the tip is kept in position by a tweezer. Once the Nickel wires are extending only about 1-2cm, the tweezer is used to pull out the Tungsten wire again. Then, the tip of the Nickel wires are spot welded to the Tungsten wire. This is done to have some maneuvering space while welding, as it is feasible e.g. to turn the angle from time to time when trying to weld wires of this size. After the two welds are in place, all four wires have to be pulled down the ceramic tube. This has to happen very evenly, else the Tungsten wire might break. A good suggestion is to take a flat nose plier and grip all wires at the same time. Once the Nickel tips are sunk just a little into the tube, the probe tip is done, the remaining part of the wires at the plug end can be pinched off and the Lemo plug soldered on. On a side note, it is a good way to get rid of the Tungsten wire end by applying a drop of solder between Nickel wire and Lemo connector. While this drop is still liquid, the Tungsten can be pressed into it, trapping it mechanically into position once the solder cools down. The resulting probe is complying with all points stated in 5.2.2. The only complication that could arise, apart from the Tungsten wire breaking if pulled too uneven, is if too much torque was applied on the Nickel wires. The torsion is translated via the welding spots into an already tense Tungsten wire, where this can lead to the wire cracking into several smaller strands, that are not visible by eye. This fault shows itself once heating is applied, and the probe burns up extremely fast and sudden at relatively low heating currents.

5.2.5 Measurement Data Post Processing

Despite the steps taken prior to the measurements to ensure accuracy and a low noise level, some post processing is necessary. All data analysis and clean up is carried out via the commercially available software package Origin Lab. This package has several functions useful for the determination of Φ_{Plasma} already built in, and it is designed to handle large datasets. In some works with emissive probes in RF plasmas, before determining the peaks, the data is smoothed out using filter packages for Savitzky Golay smoothing and related approaches. However, in this work this is not done. Doing so has a massive impact on the accuracy of the analysis, as in NJORD, the signal is on the level of the noise. So, if the noise is smoothed out, the peaks needed to determine Φ_{Plasma} via the inflection method are completely lost. Also, the smoothing can create a distortion in the identified medium peaks, as illustrated in 5.12. As the peak ratio in the unsmoothed function changes, the peak of the smoothed out function changes to. This change in peak ratio can for example be observed when moving the probe tip inwards, leading to the impression of a far greater change in potential than can be accounted for when using a more thorough approach without smoothing. Two techniques to improve the quality of the obtained results are presented here in detail as they are unique responses to the challenges of emissive probe measurements in RF plasmas. They make it

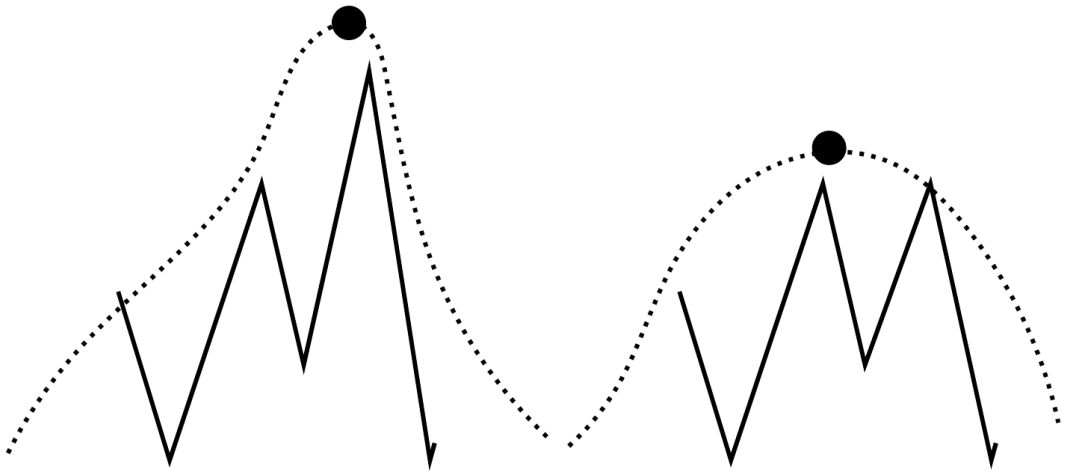

Figure 5.12: Shifting of a peak when smoothing out due to different peak height ratios

possible to improve the data-quality, but so far, no automation has been done so the process of analysis is very long and cumbersome.

Waveform Monitoring

The first method is no pure post processing method, but needs some preparation by taking an actual measurement. The emissive probe is set to floating potential and the time evolution of the floating potential is observed on an oscilloscope. Two types of information can be obtained. First, the distance between minimum and maximum floating potential gives a good estimate of the amplitude of RF caused oscillation effects reaching the probe. This is very useful, as this is also determining the distance between the outer most double peaks [27] (see chapter 4.2.5 for explanation). With this knowledge it is possible to sort out strong peaks that are too far away, and thus have to be caused by other reasons and focus on identifying peaks within plausible range. A small graph with the amplitudes at increasing gas flow (and as such, pressure) is given in figure 5.13. The conditions under which the graph was taken are in Argon, both source coils supplied with 5A, 600W forward RF-power and 5W reflected RF-power. The graphs were taken over several days, with the plasma switched off in between. Regardless, the oscillation amplitude for this voltage proves to be stable between 1,5V and 2V. This is in accordance this the recorded I-V traces, so this can be seen as a good first sift for useful data points.

Second, the waveform created by the floating potential can be recorded to

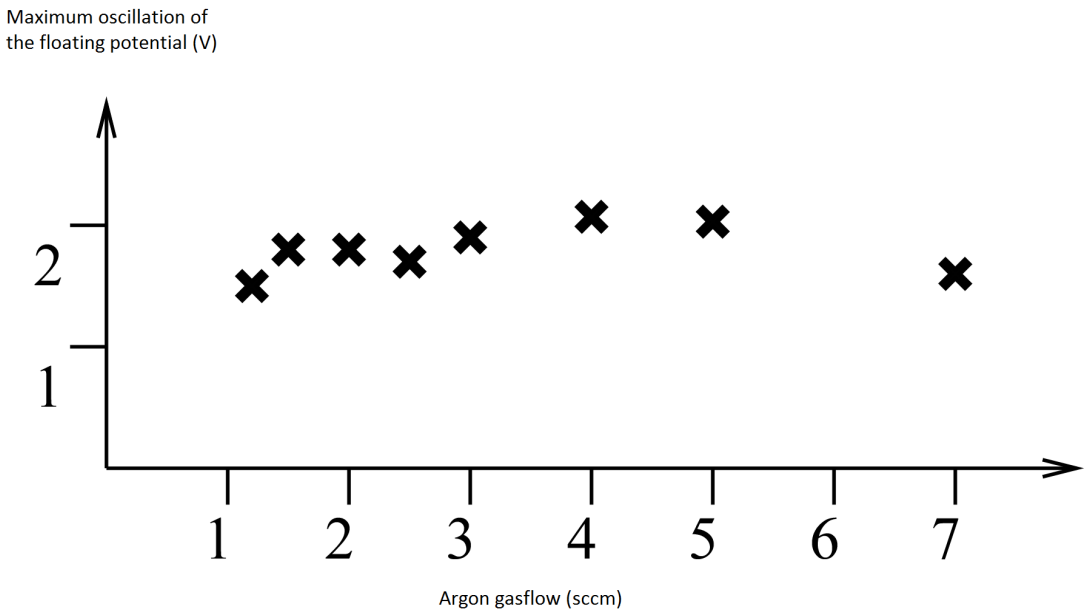

Figure 5.13: Graph for the floating potential oscillation amplitude

reveal more about the peak ratios. By using Fourier transformation, the frequency harmonics driving the particular waveform can be estimated (see figure 5.14 for an example of a time dependent floating potential taken at 4sccm. This is a common quiet plasma with only one harmonic present). The composition can not be determined exactly from this, as for phase locked harmonic waveforms the total self bias dampens out a bit, as explained in [5]. Compared to how the self bias would behave, if all components would be treated on their own and then added up, the floating potential is a bit lower. Still it is of particular use to have a comparable size when trying to match numerical simulations to the data for explanation of the phenomena observed. In those numerical simulations it can also be observed, that when having an oscillation with several harmonics in the potential oscillation, the actual amplitudes do not show up as the peak to peak distance in the $\frac{dI}{dV}$ graph, but rather combinations of the several amplitudes, added up nonlinearly. See figure 5.15 for an illustration. In this run, 3 harmonics are oscillating (Base with an amplitude of 2,5 V, 1st harmonic with an amplitude of 2 V and 2nd harmonic with an amplitude of 1,5V), and if added up linearly, they should amount to a maximum oscillation of 12V between the peaks. The max distance between the peaks however, amounts only to 9,3V.

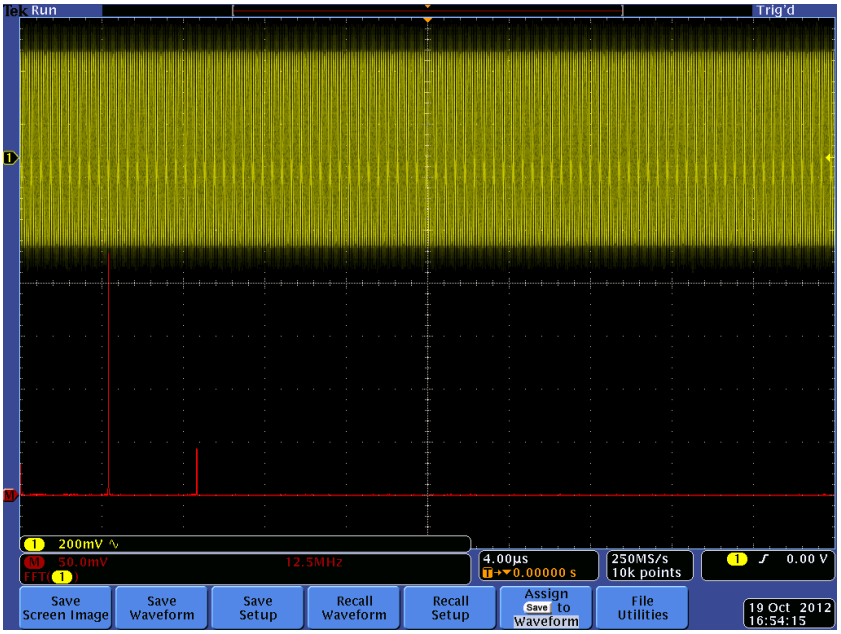

Figure 5.14: FFT of a floating potential, taken at a gas flow of 4sccm, to monitor the behavior of the RF in NJORD. The FFT (in red) shows that the base frequency of 13,6 MHz is the strongest peak with the first harmonic at 27,2 MHz also containing significant power

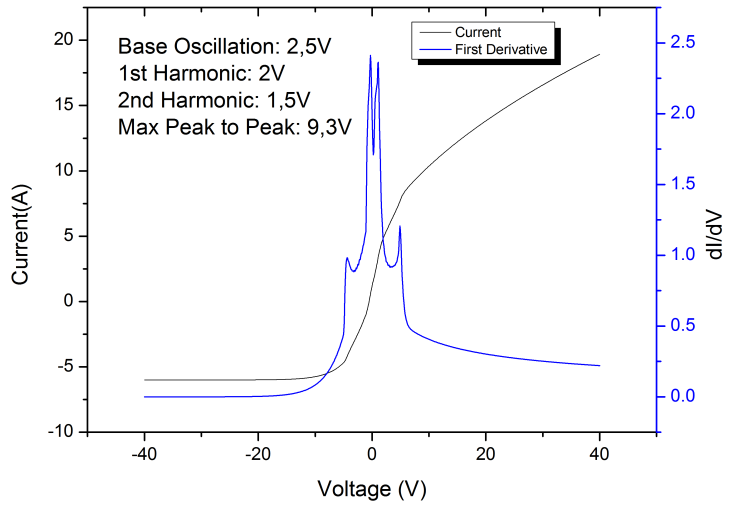

Figure 5.15: Illustration of the nonlinear addition of several harmonics concerning the peak to peak distance. Obtained via the simulation code given in appendix A

5.2.6 Peak versus Noise discrimination

A big advantage in trying to reduce noise and erroneous identification of peaks is the fact that several I-V traces are taken at several positions in one experimental run. Comparing those sets of data from one run against each other provides a possibility to identify re-occurring peaks and separate them from random peaks only present in one specific characteristic or peaks that got lost due to too small intensity (see figure 5.16). A far more powerful tool however, is to utilize the fact that in the derivative of the I-V-trace, even for several peaks the middle point between every pair should be the same. So the procedure proposed in this thesis is to take pairs around the expected potential. Monitoring the waveform or assessing the floating potential are helpful to do this, as is simple inspection of shape of the derived trace. The mid points of all pairs are then compared. If the midpoints show strong fluctuations, then one of the pair points chosen was a random peak due to noise and not a peak created by the RF distortion of the I-V-trace. An illustration of this is given by figure 5.17 and 5.18. As in figure 5.17 the peak pairs are chosen properly, the mid point is moving only 0,2V. In comparison, to illustrate, in figure 5.18 a fourth pair was chosen, to include a peak that was noise and not signal. The midpoint in this example is moving by a total of 0,65V. Also, the statistic spread is clearly higher.

5.2.7 Empirical Mode Decomposition

Another method that was explored in the process of this thesis is application of the EMD. The idea is based around a concept used recently by the Max Planck Institute in Greifswald, but apart from being mentioned in a talk at the EPS/ICPP 2012, it has not been published [35]. The goal is to apply strong signal processing to clear up the data and get a better I-V trace. The empirical mode decomposition method is detailed in a base paper by Huang et. al. [36]. It actually consist of two steps, the sifting of a signal into several intrinsic mode functions and the Huang-Hilbert transform to obtain amplitude and frequency resolved spectra from these. The EMD is far more robust than the commonly used Fourier transform, as it does not have the same set of strict prerequisites. For a Fourier transformation to be truly valid, the signal is required to be either periodic or stationary. Also, the underlying system generating the signal must behave linearly [36]. In the method presented by Sarasola [35], a probe was swept very slowly in a RF plasma with respect to the RF. Afterwards, the main mode was extracted by sifting and the phase was determined for every point in the main mode. Afterwards, points of same phase where binned together to obtain I-V traces at different phases of the oscillation. In NJORD, this scheme is not directly applicable, as often the signal consist of several equal harmonics plus a good deal of noise that make it hard to

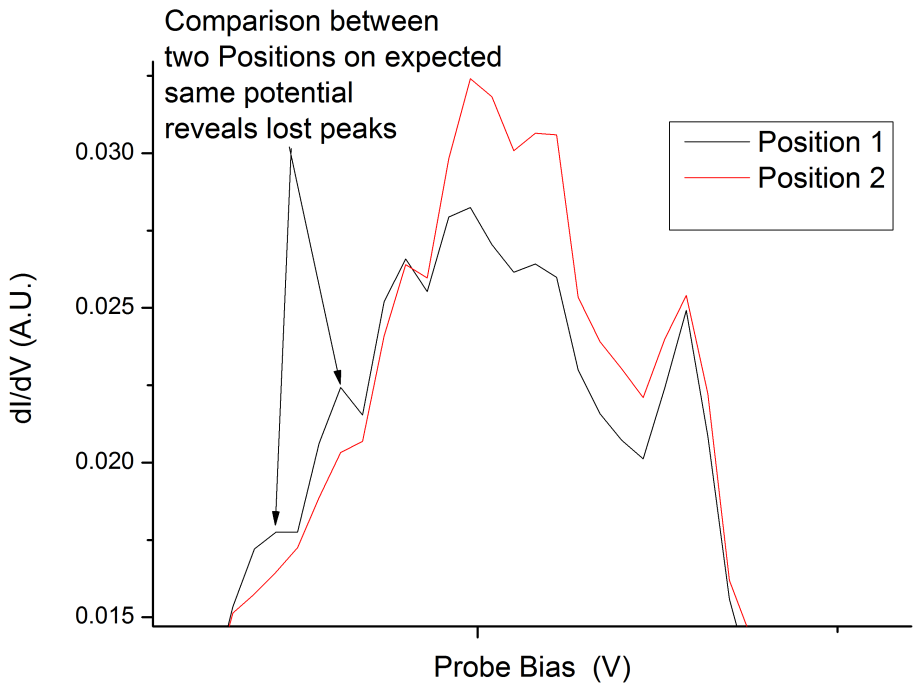

Figure 5.16: Peak identification via comparison between two probe characteristics that are presumed to be on the same potential

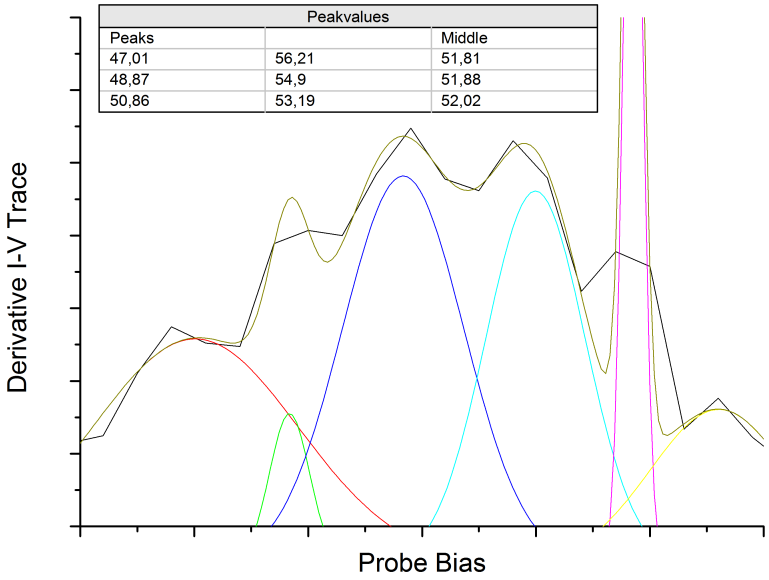

Figure 5.17: Fitting of several properly chosen peak pairs and their midpoints.

identify a dominant mode and the measurment system was not originally designed to do this. However, it is proposed here to just extract the general trend and try to analyze it. The assumption is that the oscillations are of such high frequency compared to the sweep that when sifted out, they should not impact the probe characteristic. Then, the base mode should reproduce a clean I-V trace with all important phenomena conserved. A free available EMD package for Mathlab was used, offered to the public online by Rilling from the ENS Lyon. In short, the concept of the EMD can be seen as a more powerful, generalized Fourier transformation. A time dependend signal is represented via Fourier transformation as follows:

$$X(t) = \sum_{j=1}^{\infty} a_j \exp\left(i\omega_j t\right) \tag{5.2}$$

The EMD in comparison is representing the signal with a time variable a_j and ω_j:

$$X(t) = \sum_{j=1}^{n} a_j(t) \exp\left(i \int \omega_j(t) dt\right) \tag{5.3}$$

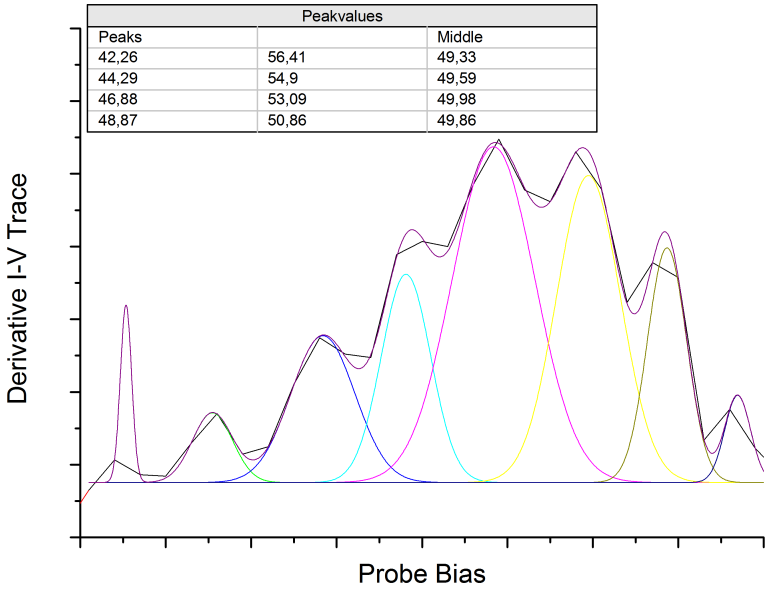

Figure 5.18: Fitting of several peak pairs, but with wrongly chosen pairs.

Sifting for intrinsic mode functions

The most useful part of EMD for this thesis was the sifting process. To sift for an intrinsic mode the following steps are taken to obtain the several modes.

1. The maxima of X(t) are determined.
2. The maxima are connected via cubic spline, giving the upper envelope.
3. The minima of X(t) are determined.
4. The minima are connected via cubic spline, giving the lower envelope.
5. The mean m_1 between upper and lower envelope is determined.
6. Calculate the first sift, $h_1 = X(t) - m_1$.
7. Repeat steps 1 to 5 with h_1 instead of X(t) to determine m_{1_1}.
8. Calculate $h_{1_1} = h_1 - m_{1_1}$.
9. Repeat steps 7 and 8 until the sifting process gives $h_{1_{k+1}} = h_{1_k} - m_{1_k}$.

10. Take h_{1_k} as c_1, the first intrinsic mode function
11. Calculate the residue $r_1 = X(t) - c_1$.
12. Repeat the whole process with r_1 instead of X(t) to determine c_2 etc.
13. At the end, the signal should be decomposed into n intrinsic mode functions and a base trend, $X(t) = \sum_{i=1}^{n} c_i + c_{base\,trend}$

It is pointed out, that while this rigorous sifting is mathematical valid, in real physics care should be taken not to over-sift [36]. As such, as a stop condition for the sifting process to obtain an intrinsic mode function, the standard deviation SD is used:

$$SD = \sum_{t=0}^{T} \left[\frac{\left| (h_{1_{k-1}}(t) - h_{1_k}(t)) \right|^2}{h_{1_{k-1}}^2(t)} \right] \tag{5.4}$$

The recommendation is to take a value of SD between 0,2 and 0,3 as an abort parameter for the sifting to proceed and take $h_{1_{k-1}} = c_1$ and continue to sift for the next intrinsic mode function. The mode functions are by this sifting ordered hierarchical by frequency. Care has to be taken as to what functions are used to initiate the sifting, as discrete steps can throw the process of balance, and thus create artifacts that are not existent in the original data. Also a critical thought about phenomena observed in the intrinsic mode functions is in order, as the data EMD makes it easy to fall for false assumptions. It is worth a notion too that this step requires far more computing power than e.g. FFT.

Hilbert Transformation and instantaneous frequency

For an arbitrary time series X(t), the Hilbert transform Y(t) can be determined with P indicating that the Cauchy principal value is taken to get a solution to the improper integral:

$$Y(t) = \frac{1}{\pi} P \int_{-\inf}^{\inf} \frac{X(a)}{t - \tau} d\tau \tag{5.5}$$

If this transform exists (note that this is not always given), a complex number Z(t) is defined as:

$$Z(t) = X(t) + iY(t) = a(t) \exp\left(i\theta(t)\right) \tag{5.6}$$

With:

$$a(t) = \sqrt{X^2(t) + Y^2(t)}\, and\, \theta(t) \arctan\left(\frac{Y(t)}{X(t)}\right) \tag{5.7}$$

From this, finally the instantaneous frequency can be determined as:

$$\omega_{instant} = \frac{d\theta(t)}{dt} \tag{5.8}$$

This should then be done for all intrinsic mode functions. Knowing the instantaneous frequency, the phase can be determined and as shown by Sarasola [35] when there is only one dominant intrinsic mode, with a slow sweep it is even possible to obtain several I-V traces corresponding to certain points in the RF oscillation. This however was not done in this thesis as explained earlier, but given an experimental setup specifically towards this goal, it should be possible too.

5.3 Retarding Field Analyzer

The reference tool used in most HDLT experiments is the retarding field energy analyzer, RFEA or sometimes called ion energy analyzer, IEA, capable of giving reliable information about the ions in the experiment. Like Langmuir and emissive probes, RFEAs belong to the group of measurement to determine plasma parameters by measuring a current drawn with a certain bias. But the design of a RFEA is more intricate. Going through the probe coming from the plasma, first comes a housing, which can be set ground to provide shielding against the RF in a helicon driven plasma. Also, the entrance hole (or slit depending on manufacturing method) has to be as small as possible, but still big enough to allow a reasonable number of particles to enter into the analyzer. The opening angle also impacts to an extend the form of the real energy distribution measured in comparison to an ideal, one-dimensional distribution [37]. Then comes after a short distance (inside the probe head, Hutchinson recommends under the assumption of a one dimensional distribution at a max a distance of $\approx 4\lambda_D$[6]), a grid. This first grid is biased appropriate negative with regards to the plasma to repel electron so that only ions enter the probe. Then comes a second grid, that is biased positive in relation to the first grid. This is to repel ions below a certain kinetic energy. Sweeping this grid bias gives the current to relative voltage characteristic that gives as a derivative the ion energy distribution. The third and last grid is biased negative again, being biased more negative than the collector which comes after the grid. This is to suppress the collection of electrons to the second grid, that stem from secondary electron emission as the ions hit the collector. Without, every electron emission from the collector would add to the ion current, effectively increasing it. A schematic of this concept as well as the potential inside the probe can be found in figure 5.19. The small opening angle gives the option to measure ion energy distributions in several directions. By doing so, ion beams can be distinguished from the background plasma as well as their direction can be calculated. In addition, from this distribution functions Φ can be determined. Not having to rely on assumptions like Maxwellian distribution but instead being able to access the real distribution is also a big plus, and as lot of data about HDLTs is won by means of RFEAs. As stated in [37], a bit of caution is still appropriate about

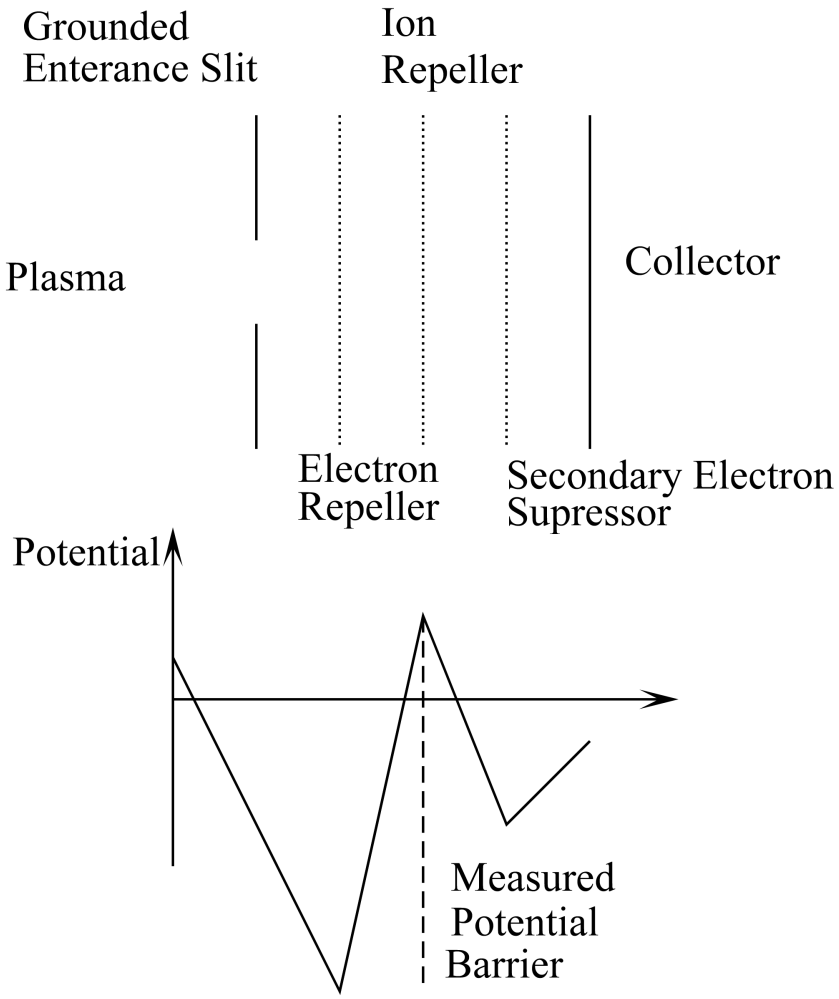

Figure 5.19: Schematic of the RFEA principle and the potential inside

the values for Φ_{Plasma}, as simulation of RFEAs show the peak in the derivative of the obtained distribution functions to be shifted downwards in real plasma with multidimensional velocities, which corresponds to a lower Φ_{Plasma} measured. Also the construction, compared to emissive probes, is a more demanding mechanical task.

Chapter 6

Experimental Results via Inflection Point Method

When using an emissive probe in an experiment like NJORD, the obtained I-V traces and their derivatives are different from the standard traces described in literature. In figures 6.1 and 6.2, an exemplary cold trace as well as traces at different heating currents are given for a gas flow of 2sccm. In figure 6.3 and 6.4 the corresponding derivatives are given. In figure 6.5 and 6.6 I-V traces taken at the same heating currents are given with a gas flow that has been doubled to 4sccm. The corresponding derivatives are given in figure 6.7 and 6.8. While the cold trace is in qualitative accordance to the discussions in chapter 4 and the simulations, the heated I-V traces reveal a more complicated situation. Identifying, explaining an modeling the physical principles that amount to the measured I-V traces is the main goal of this chapter.

6.1 Classification of Features

The original goal of obtaining good potential measurements is difficult to attain with an emissive probe in NJORD, but insight into the physics of the discharge is a benefit. The three features deviating from standard characteristics are shown in figure 6.9. They consist of a capacitance effect, a second peak shaped feature, that has been linked to a second electron distribution and a distinct peak in the set of peaks used for the inflection point method. While varying heating and pressure, the impact of the features varied too. So in chapter 6.8 an overview of the behavior over different pressure is given. Those features in combination with noise and strong restraints on what constitutes a good heating current reduces the amount of well and unambiguously determined potential points. The capacitance effect is of no greater interest, as it is just caused by the electronics, an artificially

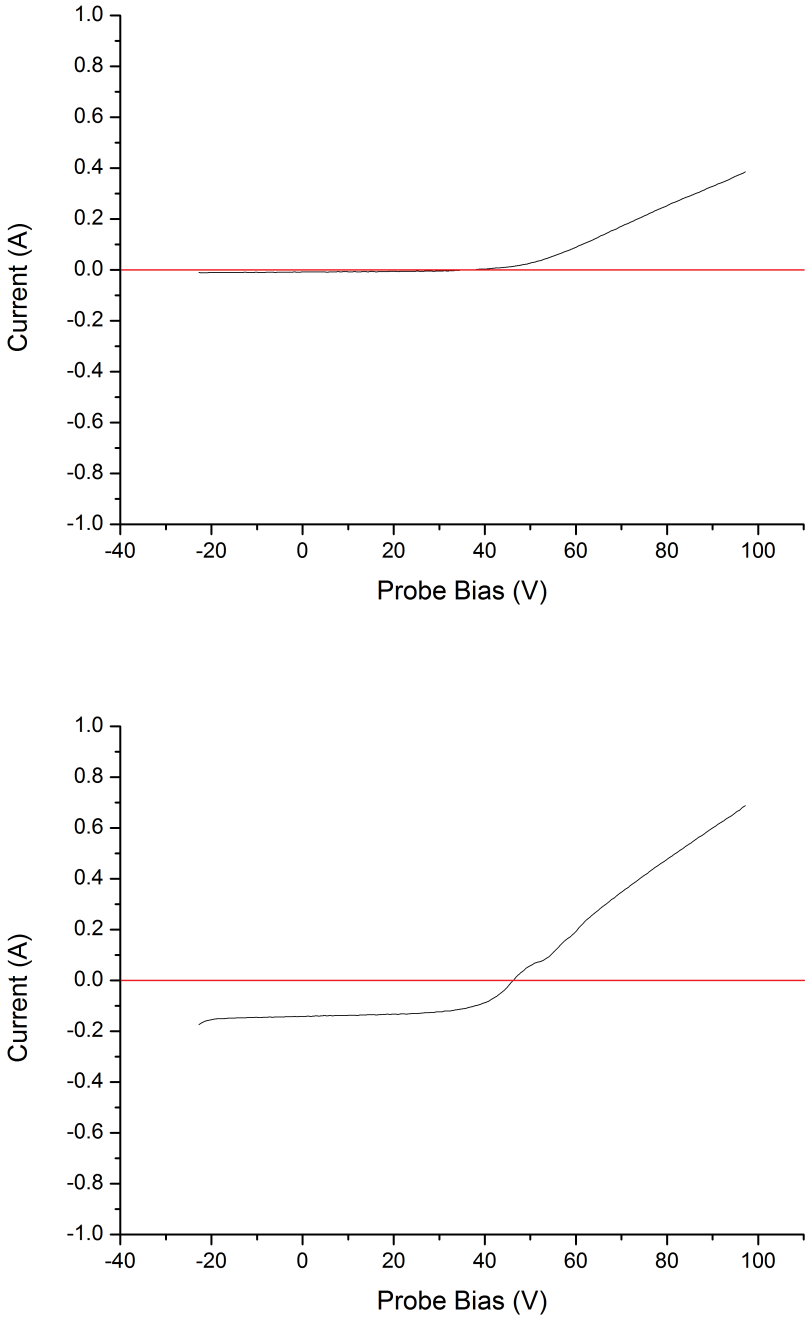

Figure 6.1: The I-V traces of a cold probe (top) and at a heating of 2,55A (bottom).Taken at a gas flow of 2sccm Argon, with 5 A in both source coils.

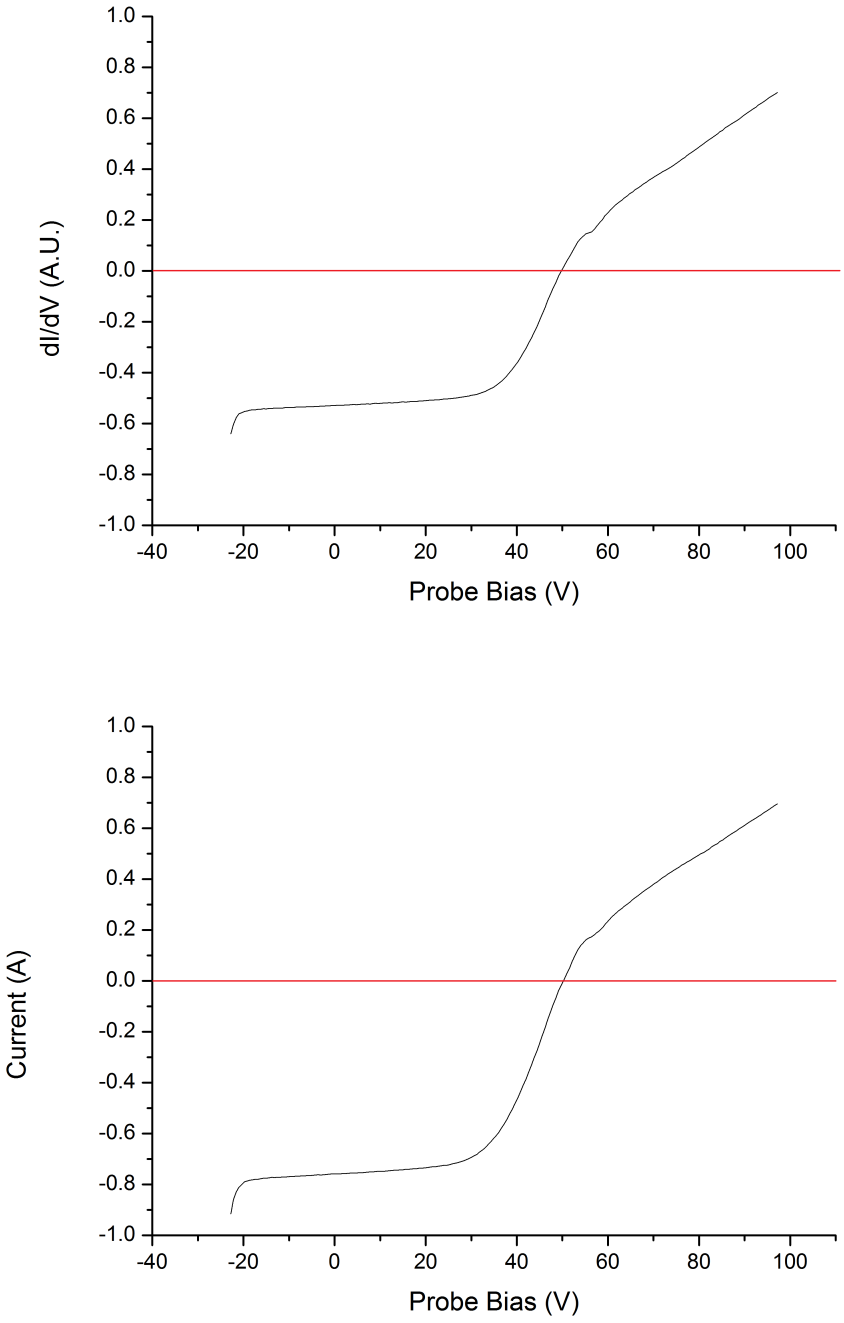

Figure 6.2: The I-V traces of a probe heated with 2.65 A (top) and at a heating of 2,7A (bottom). Taken at a gas flow of 2sccm Argon, with 5 A in both source coils.

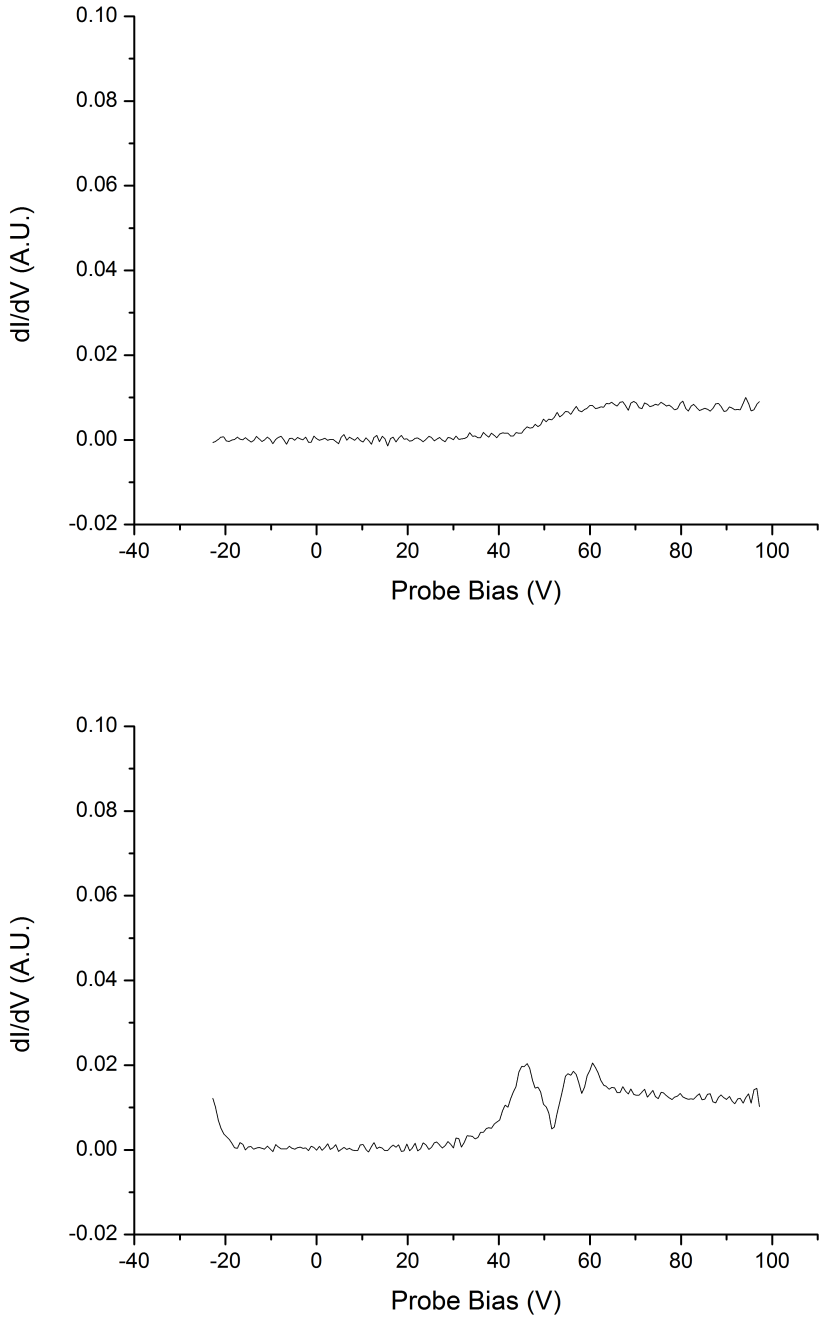

Figure 6.3: The derivatives of the I-V traces given in figure 6.1

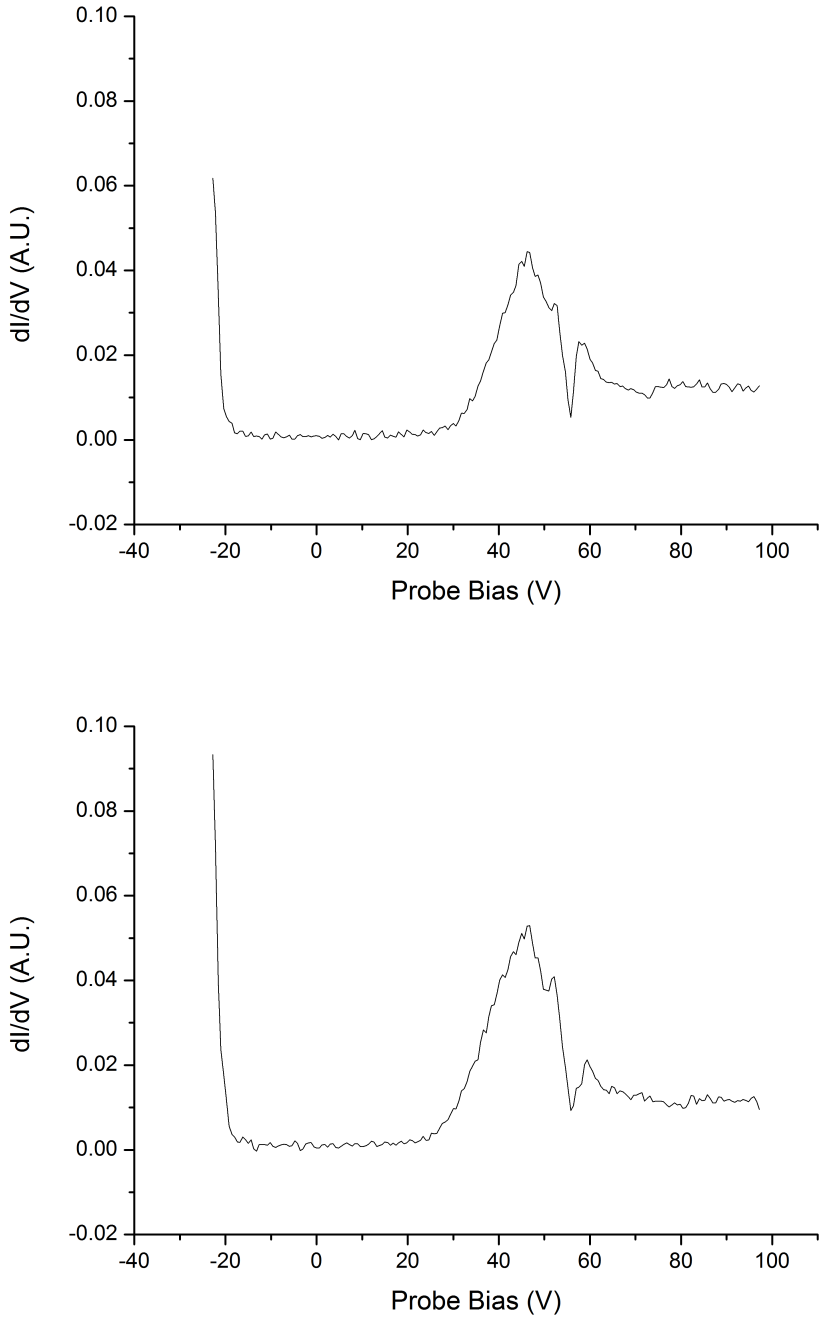

Figure 6.4: The derivatives of the I-V traces given in figure 6.2

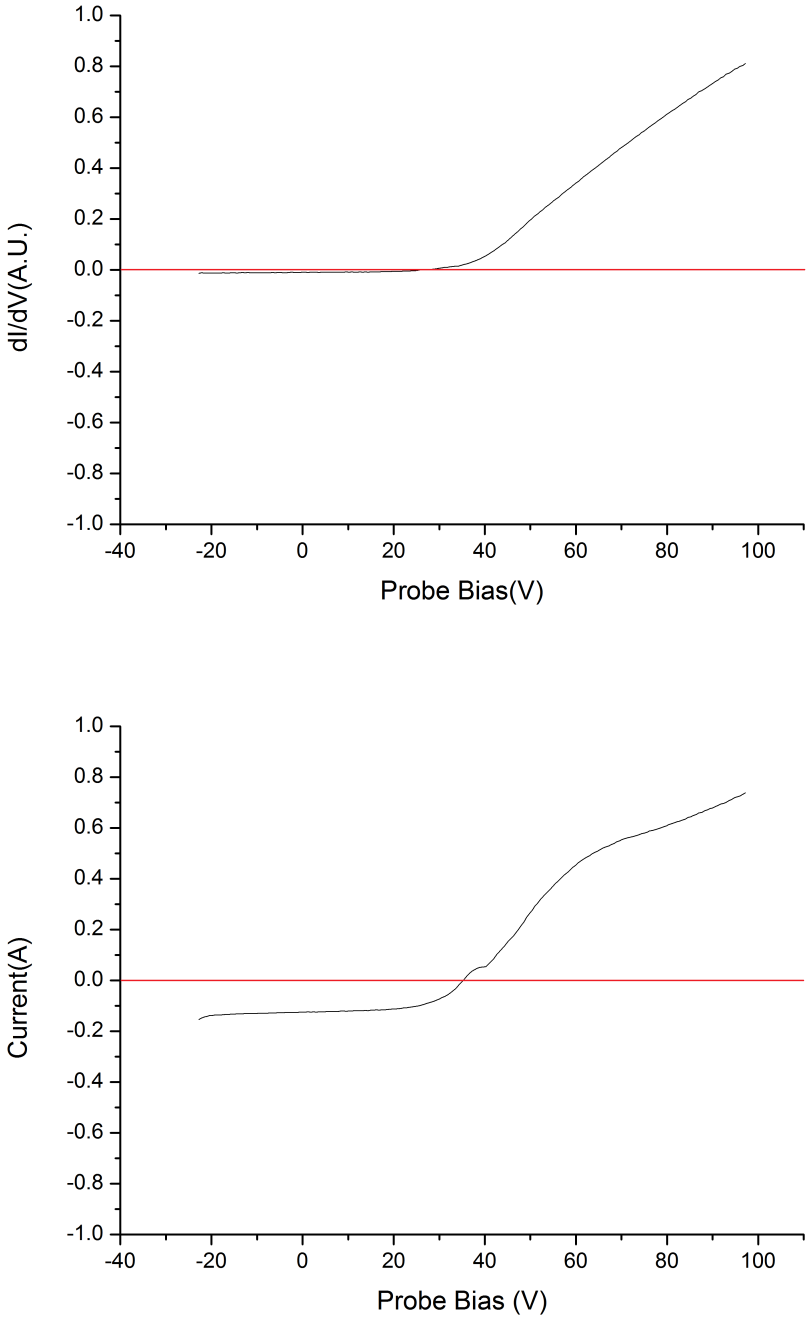

Figure 6.5: The I-V traces of a cold probe (top) and at a heating of 2,55A (bottom).Taken at a gas flow of 4sccm Argon, with 5 A in both source coils.

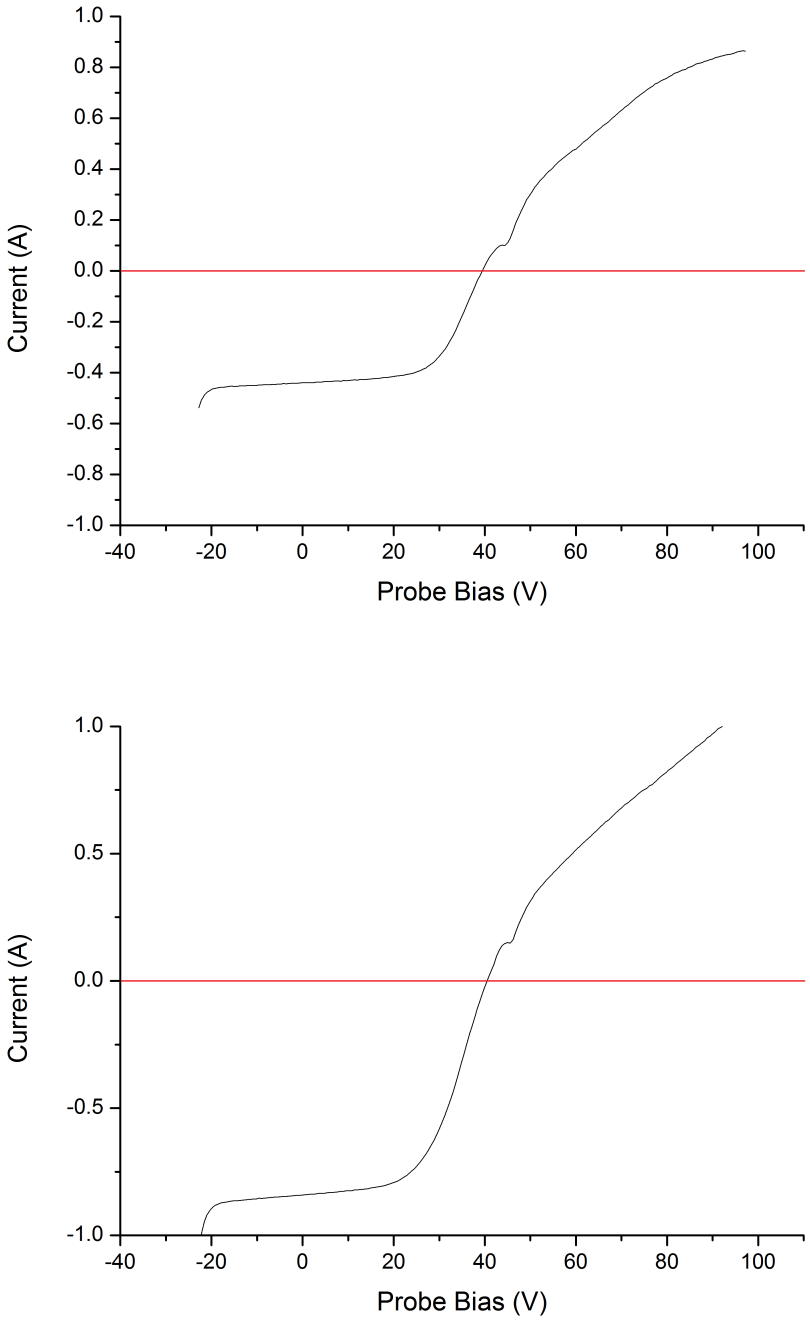

Figure 6.6: The I-V traces of a probe heated with 2.65 A (top) and at a heating of 2,7A (bottom). Taken at a gas flow of 4sccm Argon, with 5 A in both source coils.

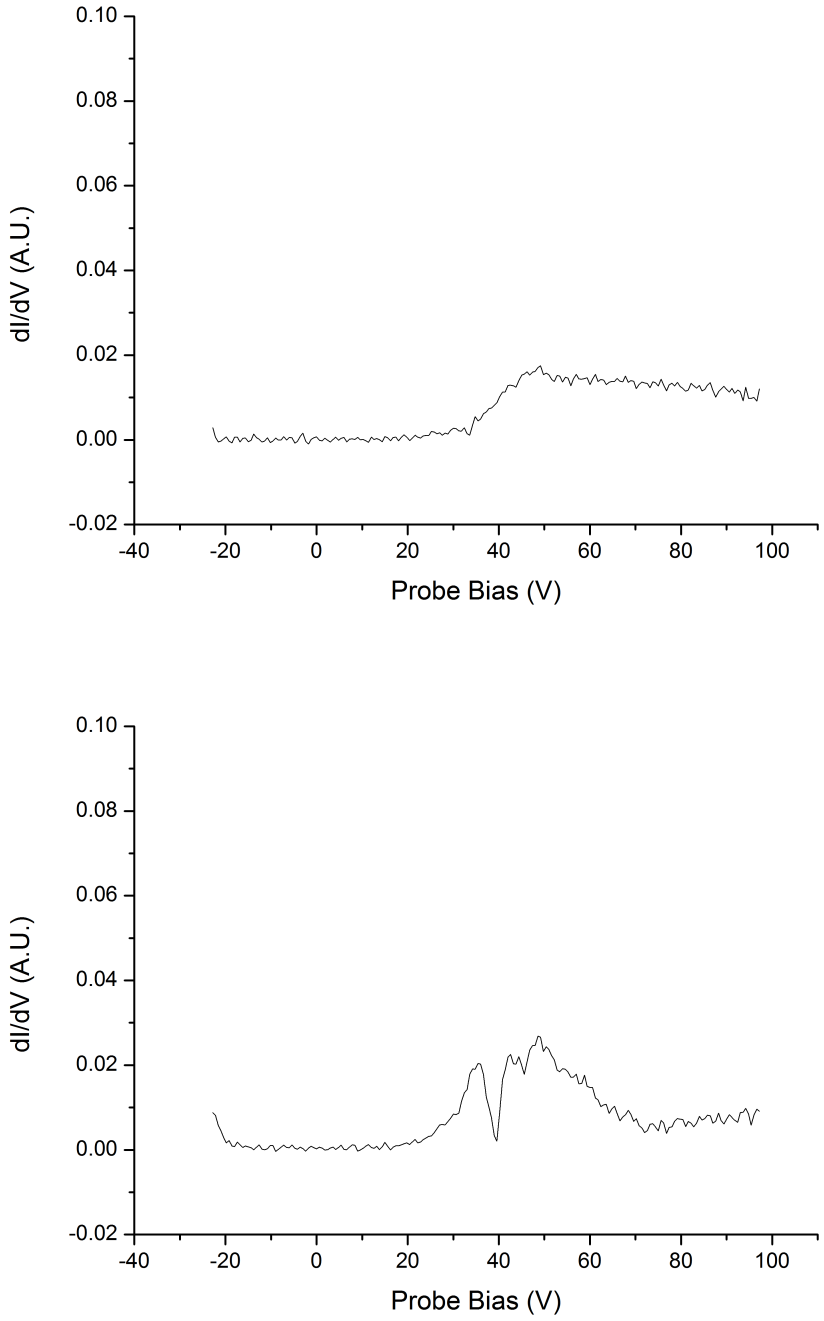

Figure 6.7: The derivatives of the I-V traces given in figure 6.5

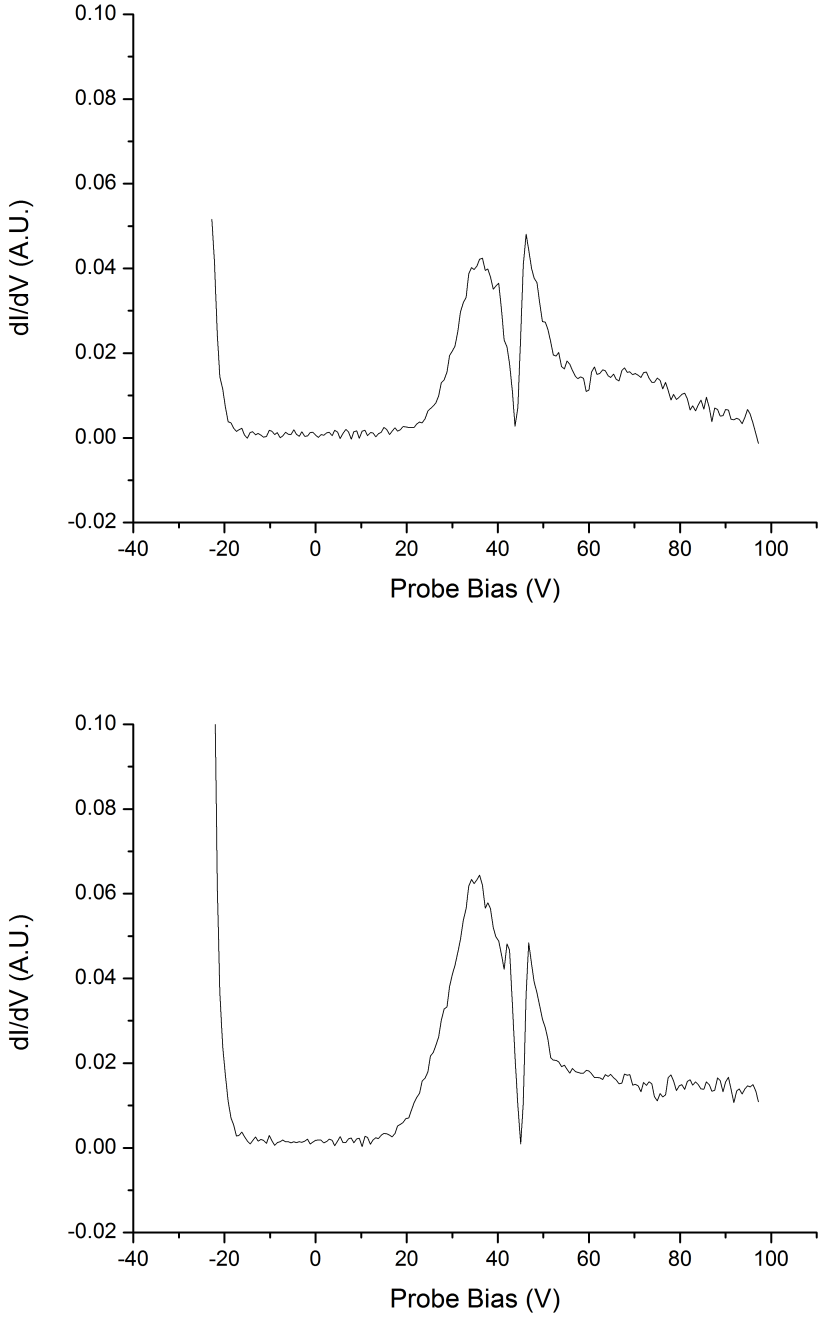

Figure 6.8: The derivatives of the I-V traces given in figure 6.6

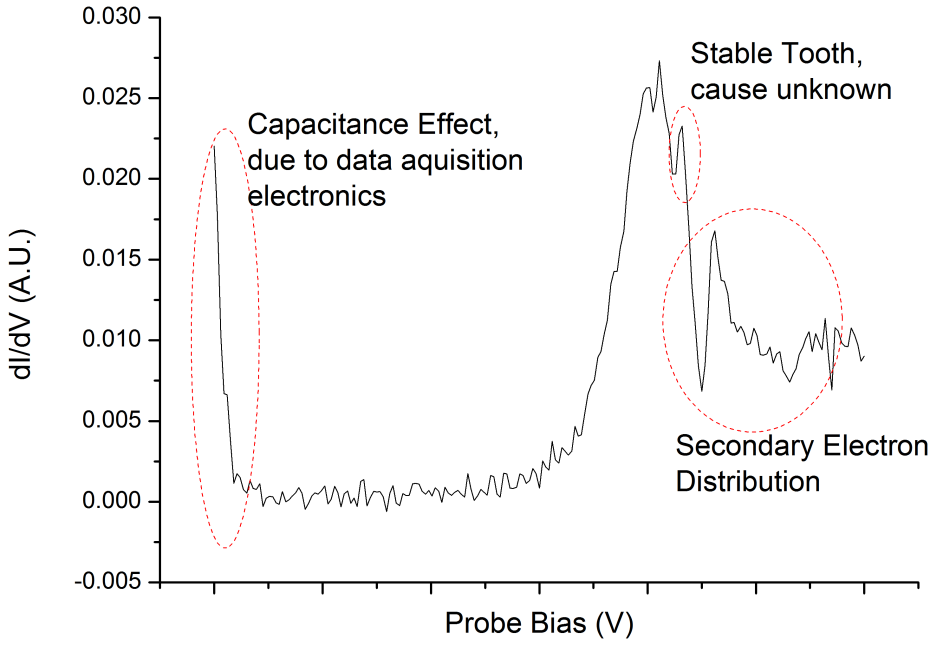

Figure 6.9: Exemplary differentiated I-V trace marking important phenomena deviating from a standard characteristic expected by modeling

induced artifact. The second shape always consists of a sharp peak and an extended hump. Quicker, less discriminating analysis might yield better results at first, however it might take in the features and as such miss the real potential by quite an amount. E.g. is it very tempting for the human eye to follow an imaginary curve that includes both features as one double peak predicted by the models for the in inflection point mehtod in some of the differentiated I-V traces (see chapters 4.2.5 and 6.3), taking the imagined curve peak as the potential while ignoring the steep drop in the differentiated trace. Investigating the cause for those disturbances however confirms physics that have been observed under certain difficulties with other methods. The last effect mentioned is a peak of unexplained, but reproducible behavior in the peak set of the derivative caused due to the transition from emitted current to collected current, which is the set used for the inflection point determination. Lacking a good explanation, this peak is referred to as the "stable tooth" in this thesis.

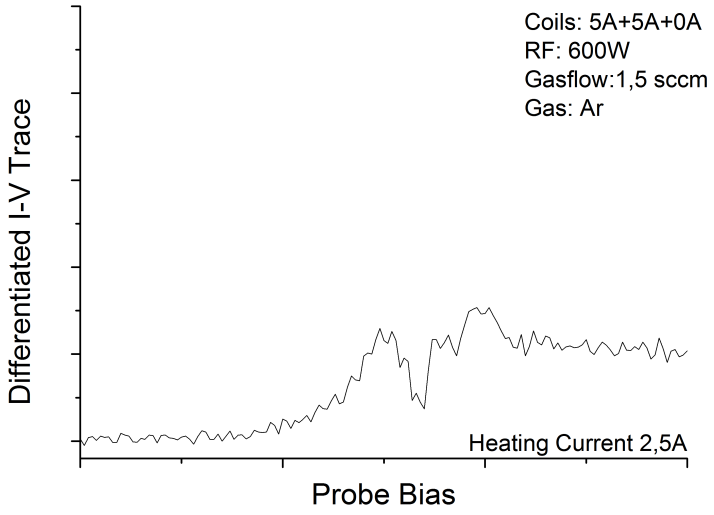

Figure 6.10: Derivative of a probe that, with 2,5 A, is heated too low. It is hard to discern the inflection point of the first distribution from the noise.

6.2 Probe Heating

As stated, the heating current is crucial in obtaining good results. If the probe is heated too little, no useful details can be obtained from the derivative of the I-V trace. The inflection point of the base electron distribution and the peak caused by the second electron distribution are on the same low level and it is very hard to discern them. If the probe is heated too much, the derivative is completely dominated by the first peak. This suppresses any clear signs of the second electron distribution. Also, the "stable tooth" forms and increases in intensity with increased heating. This distorts the inflection point peak, and makes peak identification more and more difficult. Factoring in this, the viable range for probe heating for the probe design used in this thesis was found to be between 2,55A and 2,65A. See figures 6.10, 6.11 and 6.12 for an illustration of this and figure 6.13 for a direct comparison between the derivative traces of different heating currents.

6.3 Second Electron Population

When the probe is heated, in a medium heating range a secondary peak formation can be observed (see e.g. figure 6.13) in addition to the peaks expected via inflection method. In figure 6.14 and 6.15,more detailed traces are given to compare

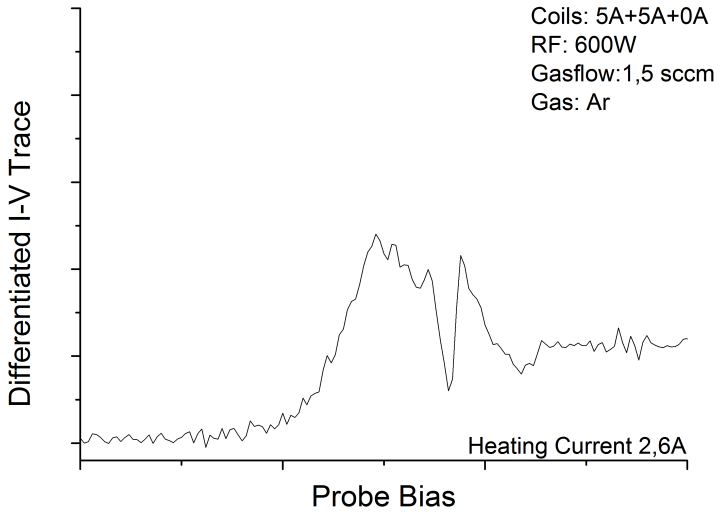

Figure 6.11: Derivative of a probe that is at a good temperature with 2,6 A. The inflection point for the first distribution is visible as well as the second electron distribution

the derivative with the original trace. As pointed out before, the second peak that is getting distinct with heating carries information about the plasma. From monitoring of the floating potential (see chapter 5.2.5), an effect linking to a strong oscillation can be ruled out. With numerical simulation, it is possible to link this peak to a second electron distribution appearing at a higher potential. In figure 6.16 a comparison between the derivative of a measured I-V trace an a numerical simulation via the code given in appendix A, set to fit the peaks of this trace, is given. No second electron population was considered, to rule out the possibility of the second peak being a result of nonlinear interaction between the different harmonics. In figure 6.17, the same trace is given, but in the simulation, a second electron population was considered. Note that the second peak in the derivative always consists of a sharp peak followed by a drawn out hump. Using the same model as for the base electron distribution and applying an RF-oscillation, this is reproduced in the simulated derivatives. The shape of the second distribution makes it easy to take the two distributions as one and to ignore the distinct separation between them, especially as it is drowned in the derivative when increasing the heating due to dominance of the emissive population. No reports of this kind of feature in emissive probe traces was found in literature published.
However, in support of the theory of a second electron distribution are measure-

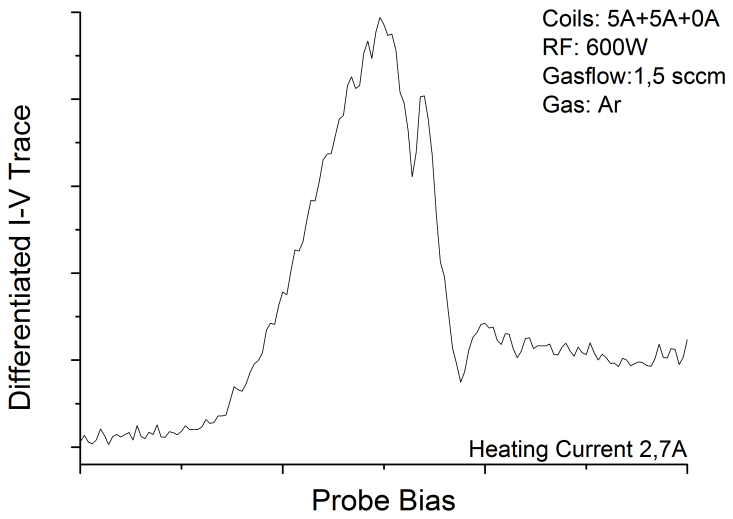

Figure 6.12: Derivative of a probe that, with 2,7 A, is heated too strongly. The inflection point of the first distribution and the stable tooth suppress the peak caused by the second electron distribution.

ments published by Charles [20] taken in an experiment of same geometry.In this paper, the electron distribution function was determined, and change in inclination was found on the higher velocity side, which was linked to a second electron distribution at a higher temperature bulging out the distribution function on one side. Combining the two observations, it is proposed here, that it is not a higher temperature, but electrons moving away from the probe in yet undetermined direction. The qualitative argument for this is as follows: Observing an electron distribution at a higher potential within the same plasma is from a physics point of view not very reasonable. A plasma should have one potential only. Temperatures might be different, but there can only be one resulting potential. But trying to pull in an electron current from electron that move away from the probe at a certain speed should result in a shift of observed potential equal to the energy needed to compensate for the kinetic energy. This fits with the observation of a higher temperature, that in essence, as explained in chapter 2.2, is a direct link to kinetic energy too.
From a theoretical point of view, this kind of electron motion is useful too. As stated in chapter 3.4.2, the model for double layer formation in experiments having a geometry like NJORD is not balanced concerning the energy flux to the walls, as for the electron energy flux, the term is too small. With this energetic

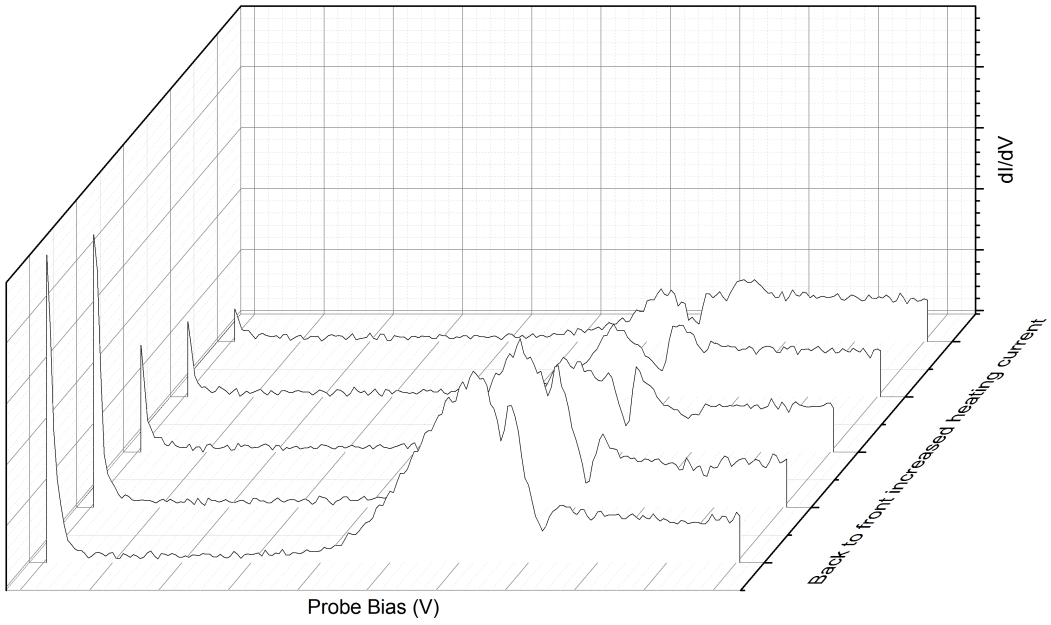

Figure 6.13: Direct comparison between different probe heating currents

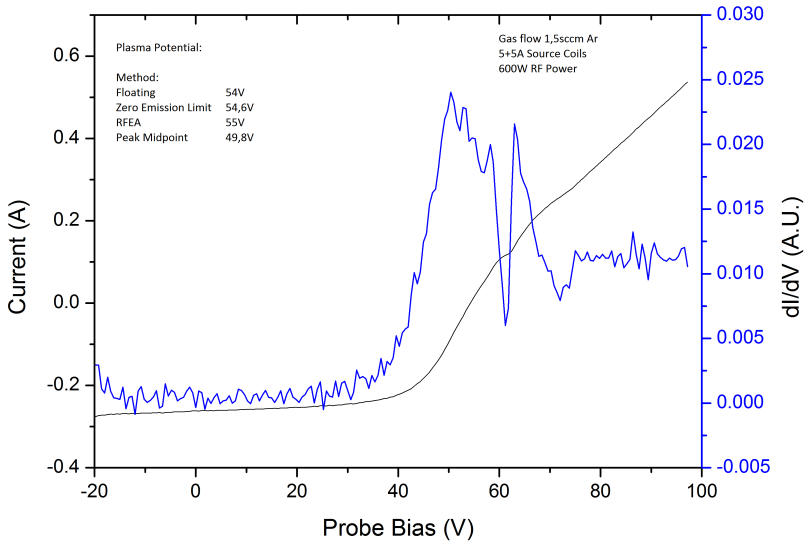

Figure 6.14: I-V Trace and derivative of a probe heated at 2,6 A positioned in the middle of NJORD at a gas-flow of 1,5 sccm. Potential calculated by different methods is given.

electrons, an explanation could be given from the experimental side, which was already hinted at by Chen when noting that in helicon devices there seems to be a mechanism that transfers temperature directed radially outwards in the source cylinder geometry into temperature directed parallel along the main axis.

6.4 ”Stable Tooth” Phenomenon

Over the course of this thesis, no satisfying explanation for the phenomenon named ”stable tooth” was found. It is a strong peak in the derivative of the I-V trace that forms, when the heating current in the probe is increased. Stronger heating makes the peak more distinct. The name stable peak was chosen, because the peak stays at the same potential while the probe tip is heated further. If the peak would be only linked to the multiple peaks created by RF oscillation, it would move towards lower potential with increased heating. This however is not the case, and the peak stays pretty much at the same potential with increased heating. With higher pressure the peak also appears but moves downwards, indicating a link to the plasma potential. Also, it takes more heating current to see the peak form, which is in accordance with the need for a higher heating to archive good I-V Traces

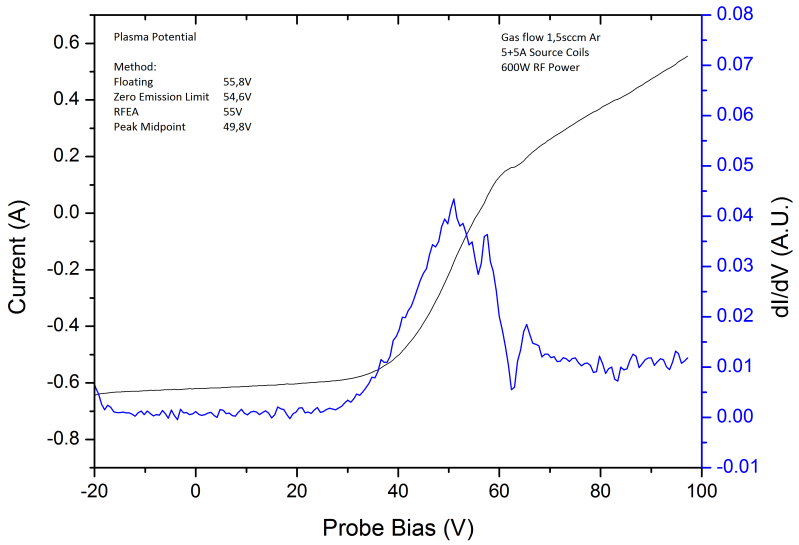

Figure 6.15: I-V Trace and derivative of a probe heated at 2,65 A positioned in the middle of NJORD at a gas-flow of 1,5 sccm. Potential calculated by different methods is given.

at higher pressure. If the physics driving this phenomenon can be uncovered in full, this might be another easy way to determine the plasma potential. At the moment, however, the modeling of emissive probes does not reproduce this peak fully and the secondary electron distribution might have an influx too. Assuming that the stable tooth is linked to the oscillation, however, it should be above the plasma potential, which can be seen in chapter 6.6.

6.5 Loss of saturation current at high bias and pressure

When the probe tip is strongly heated, and the pressure is comparatively high (gasflow rates of 5sccm and above) another deviation from ordinary I-V traces appears, that has not yet been mentioned in this thesis. At higher probe bias, only the electron saturation current governed by the orbit collection scaling factor should be visible. This however is not the case. As illustrated in figure 6.18, the saturation current declines for a probe bias roughly 20V above the plasma potential (when taking the floating potential as reference). As explanation for this phenomenon was proposed [38], that the electrons in the saturation area hit the

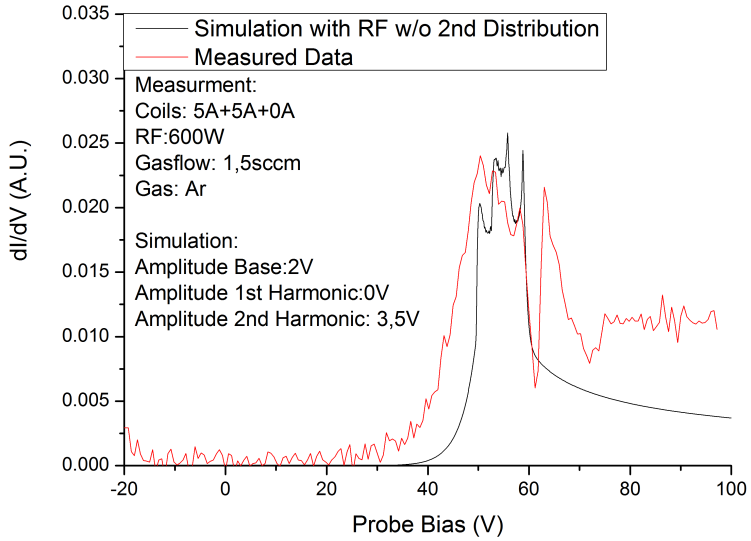

Figure 6.16: Derivative of a measured trace compared to the derivative of numerical simulation of a trace with two harmonics. No second electron population was added.

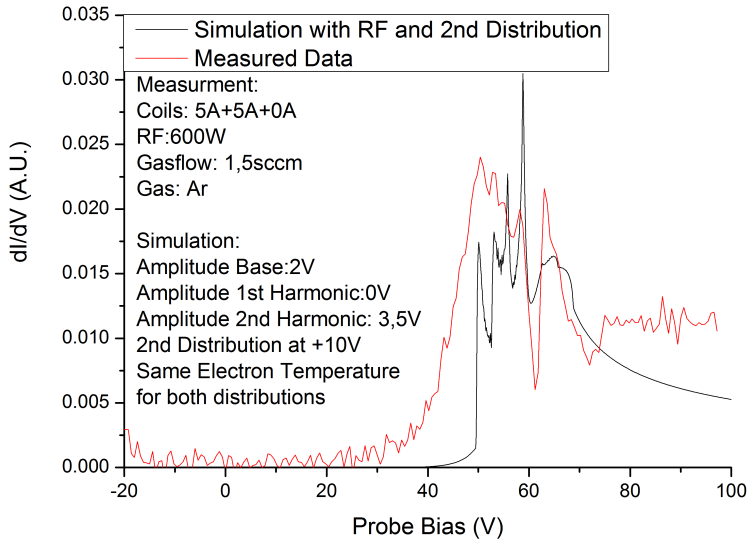

Figure 6.17: Derivative of a measured trace compared to the derivative of numerical simulation of a trace with two harmonics and a second electron distribution

probe with higher energies as the probe bias goes up. This leads to additional heating, that drives another, additional emission current. Emitted electrons are indistinguishable from collected ions, leading to the apparent loss of current. According to this model, limiting the loss is the Child-Langmuir law, which restricts a space-charge current from a virtual cathode that is supposed to form and as such, no arbitrarily strong current can be lost. In this thesis, the loss was observed to increase in strength with increasing pressure. This fits the description, as higher pressure means a higher particle density and as such, more heating. However, some questions remain open, especially in application to the phenomenon observed in NJORD. First, in NJORD current loss appears a good deal above both first and second electron distribution, which should result in a space charge current limit near zero (most models even assume the emitted current to be completely zero there, as stated in chapter 4.2.6) over the whole dip. In some of the graphs published by Lho [38], the appearance of this dip can be seen at potential higher than the plasma potential too, but no detailed discussion is given. Another open issue that needs care is the secondary electron distribution. Being a topic on its own, the interaction between the secondary electron distribution and the current loss need attention on its own. If, however a good model is available that includes both phenomena, it could pose a viable solution for quick data analysis to fit the model to the derivative of the I-V trace and discern the plasma potential immediately from this. As the current loss should directly be connected to the plasma potential, this would save the cumbersome process of varying the probe heating to get the zero emission limit.

6.6 Radial Potential Profile

Of interest for the validity of the concept of emissive probes in NJORD is a comparision between the potential profiles obtained via the RFEA method that is known to deliver realistic results and the radial profile obtained via the emissive probe. In figure 6.19, this comparison is given for a gasflow of 1,5 sccm, equaling a pressure between $0{,}22 \cdot 10^{-3} mbar$ and $0{,}31 \cdot 10^{-3} mbar$, depending on the gauge used to read out the pressure. The measured potentials are expected to have the following values in relation to the real plasma potential:

- The "Stable Tooth" is expected to be above the plasma potential (see chapter 6.4)
- The floating potential, taken here just as floating potential in the strongly emitting region should give a value above the plasma potential (see chapter 4.2.2), albeit reduced by a small shift due to the RF induced selfbias (see chapter 3.1.1)

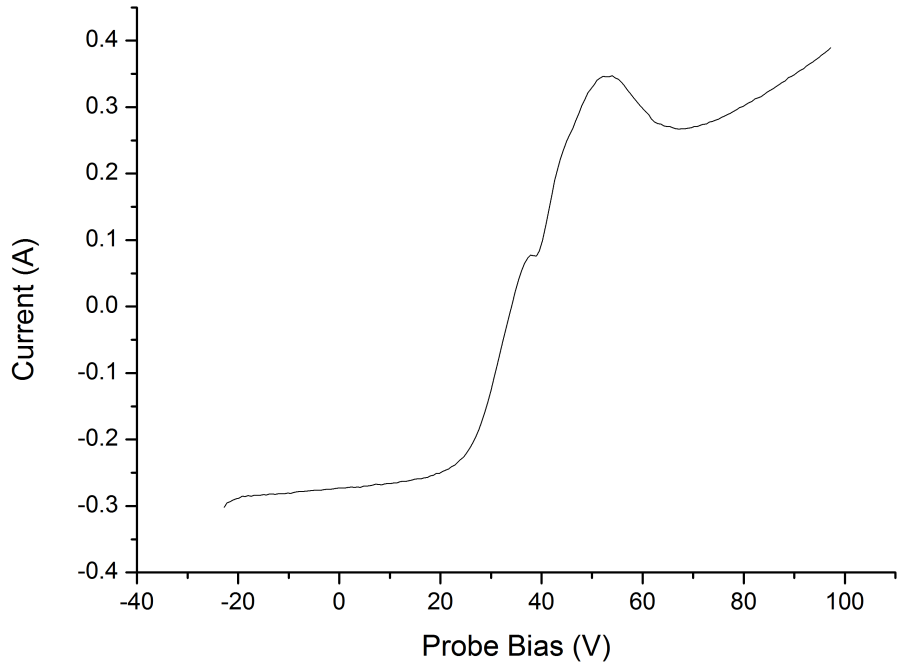

Figure 6.18: An I-V trace taken at a gas-flow of 7sccm. Note the loss of current around a probe of 60V bias.

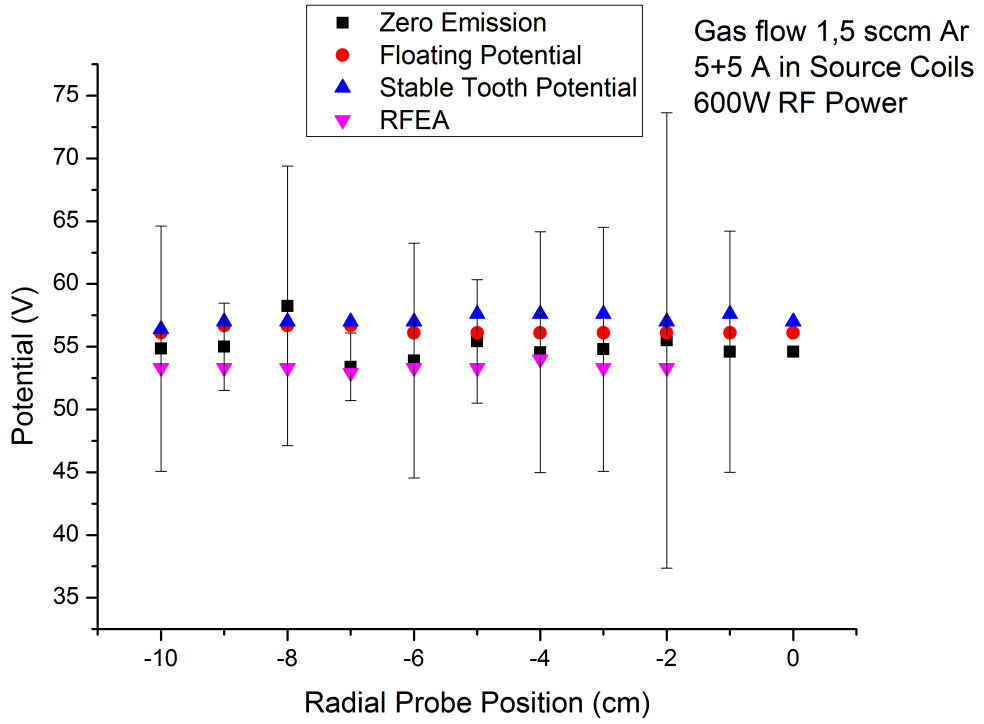

Figure 6.19: Radial Scan of the Plasma Potential, determined with different methods.

- The RFEA measurements should underestimate the plasma potential [37]
- The zero emission limit method should be the closest to the true plasma potential (see chapter 4.2.4)

The measurements in figure 6.19 show good accordance with this, which can also be seen as validation of the method proposed in chapter 5.2.6 to improve the data quality. The linear interpolation of several measurements at different heating also gives the opportunity to calculate error bars for every point measured. The error, however, is very large. This is due to the fact that only limited, discrete potential steps are recorded, and due to the difficulty of calibrating the probe heating in more detailed steps as well. With increased resolution in the scanning voltage and a finer heating control, if should be possible to reduce the error significantly. At a position of -8cm there is a slight increase in the plasma potential measured with the zero emission limit. It is not necessarily a point with bad data. As the source radius is a bit over 7cm, this could be an effect of the ion density conics measured by Charles [20] and thus it could be argued for a higher sensitivity of

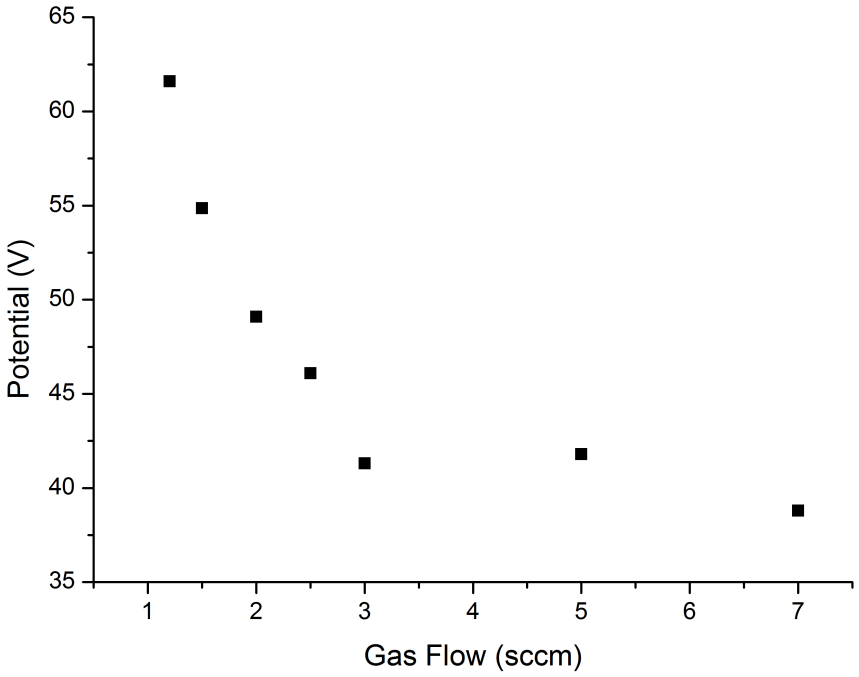

Figure 6.20: Potential determined at the center. Note that the gas flow is given. See table 5.1 for a conversion to pressure.

the zero emission limit method when applied in NJORD, compared to the RFEA or the floating potential.

6.7 Pressure Profile

To further ensure that the zero emission limit method can be trusted, the plasma potential in the center was determined for increased pressure. In figure 6.20 the potential is plotted for increasing gas flow which corresponds to pressure. This representation was chosen due to the availability of two different pressure readings from different gauges. See table 5.1 for more details and conversion to pressure. The qualitative behavior is the same as reported with other measurement methods [30], giving further credibility to the application of emissive probes in NJORD.

6.8 Radial I-V trace derivatives for different gas flow

In this section, the I-V trace derivatives where smoothed out, contrary to the points stated in chapter 5.2.5. This was done to show how the general composition of the I-V trace derivative and features within change with increased pressure. Also, with the waterfall setup, the radial probe positions are included to show that the behavior does not show strong changes with radial variation. Note that the potential in those graphs is given without the battery shift of +37,2V.

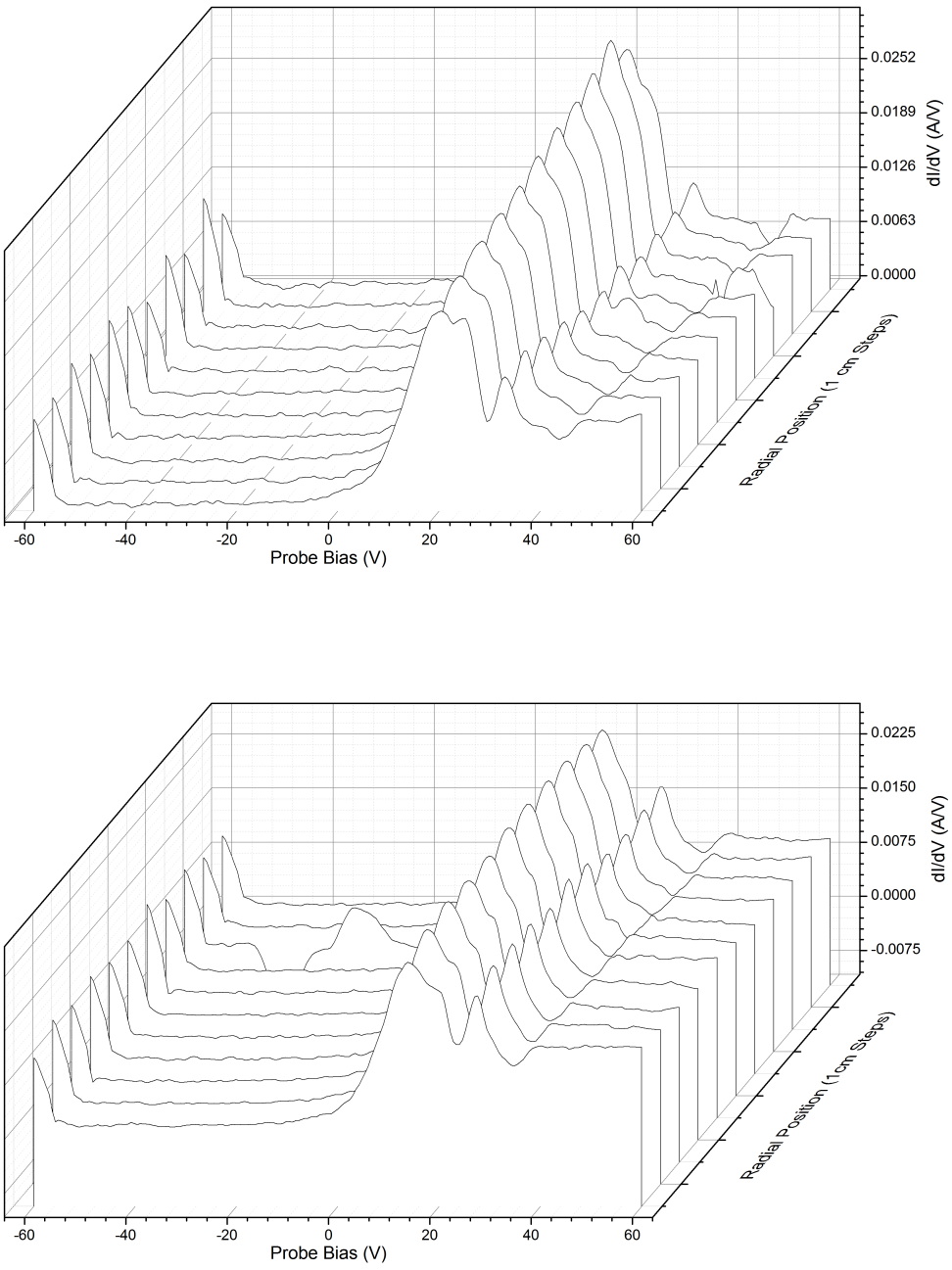

Figure 6.21: Smoothed waterfall graphs of the derivatives, radially measured. Top at 1,2sccm and bottom at 1,5sccm Argon.

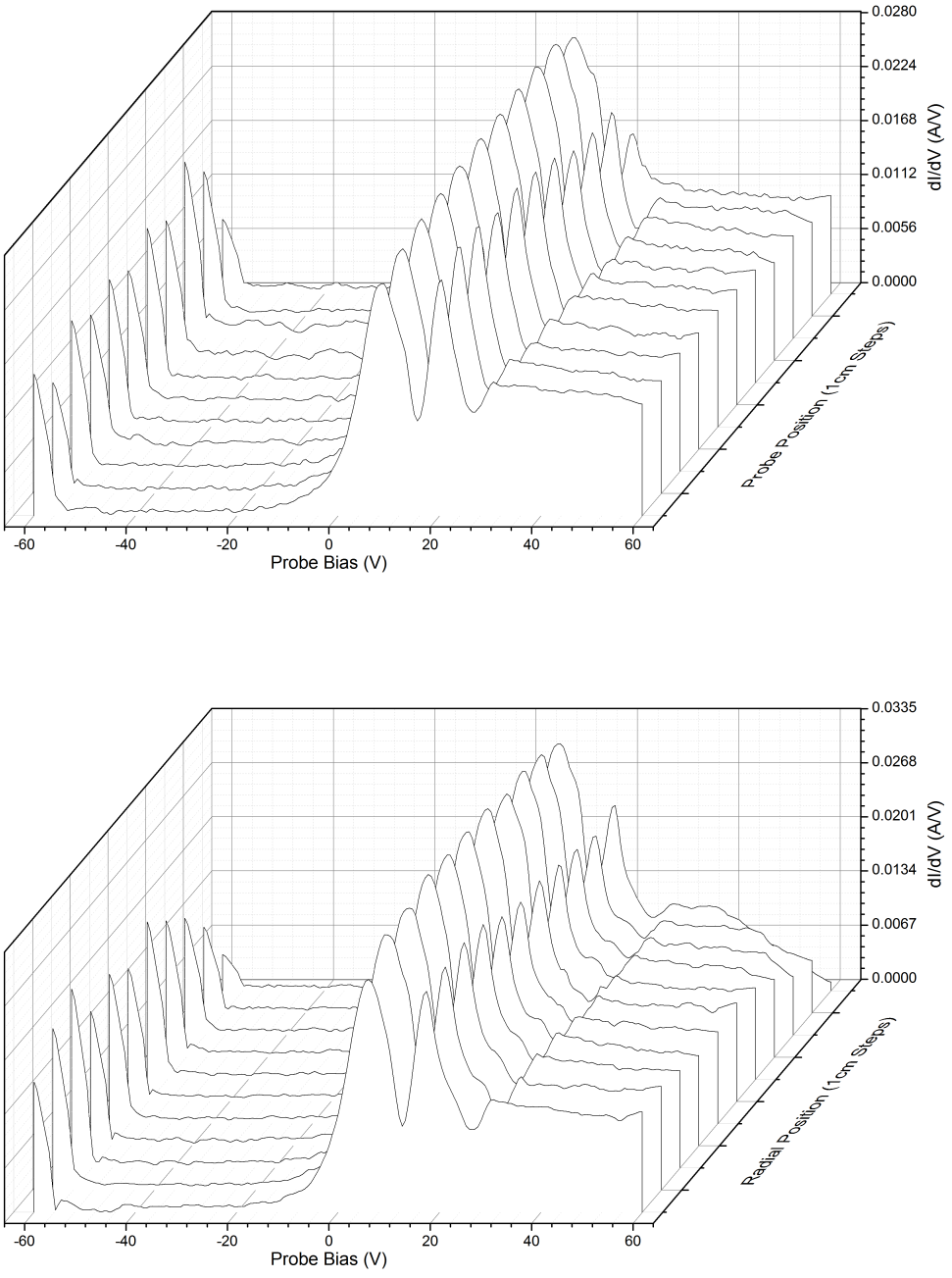

Figure 6.22: Smoothed waterfall graphs of the derivatives, radially measured. Top at 2sccm and bottom at 2,5sccm Argon.

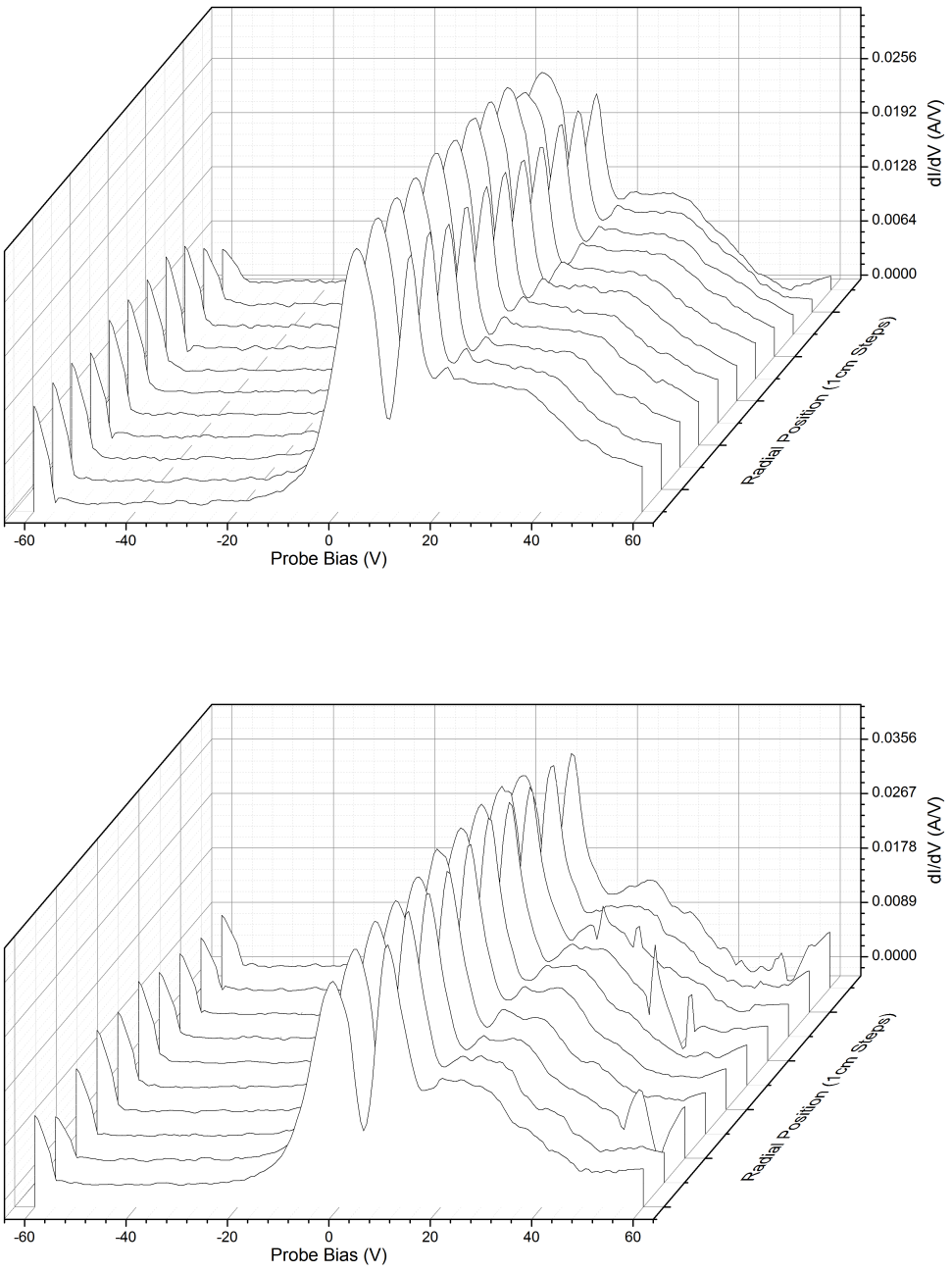

Figure 6.23: Smoothed waterfall graphs of the derivatives, radially measured. Top at 3sccm and bottom at 4sccm Argon.

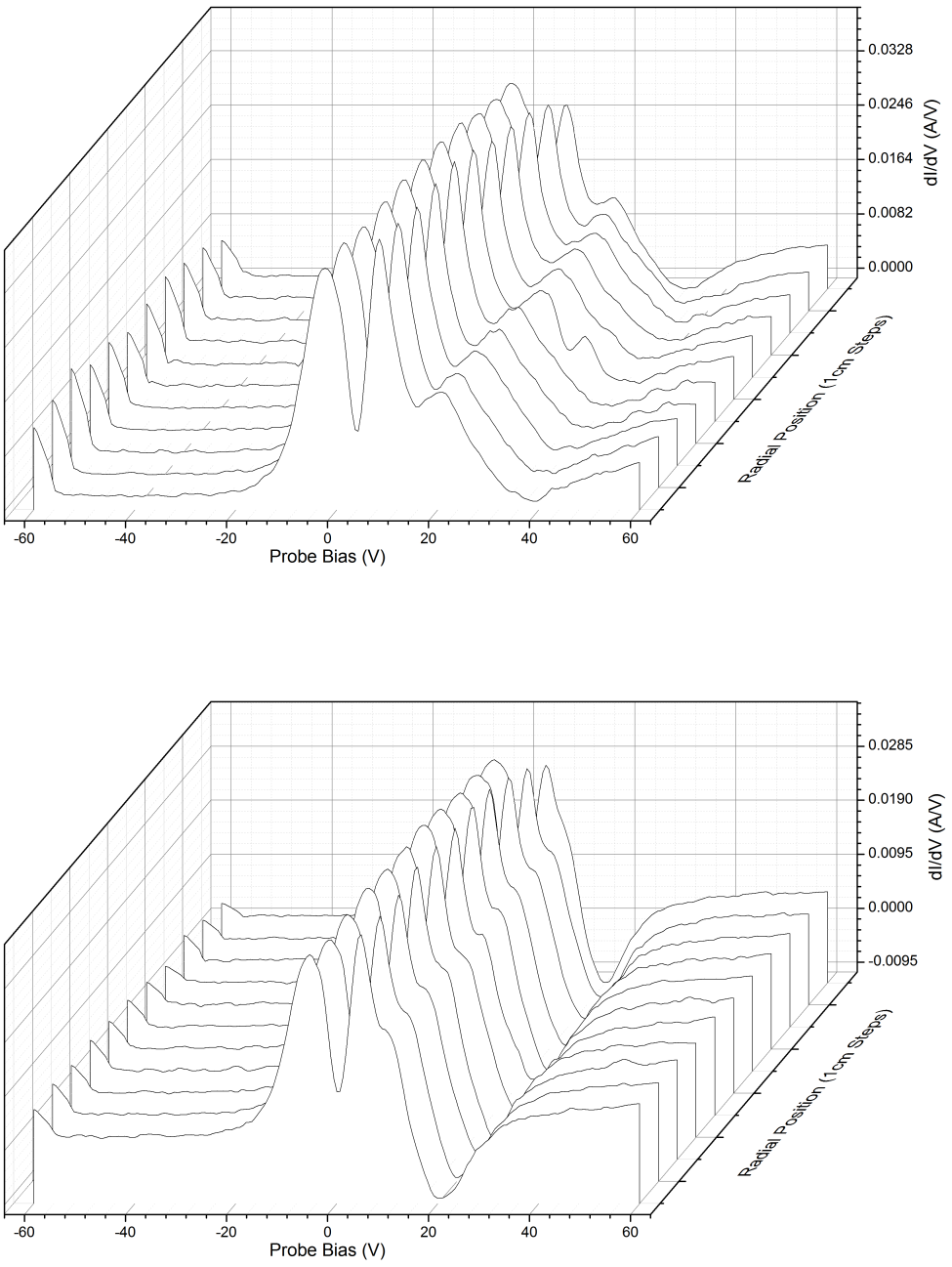

Figure 6.24: Smoothed waterfall graphs of the derivatives, radially measured. Top at 5sccm and bottom at 7sccm Argon.

Chapter 7

EMD application results

In this chapter, the EMD was used to see if the strong sifting capabilities of the EMD could be used to create an analysis method that is mostly automated to save work. Two runs of taking an emissive probe characteristic and subsequently analyzing it with EMD where taken. The lack of accessible computing power made for a slow analysis. The problem was exaggerated by in retrospective poorly chosen data in the first run. The measurement system consisted of an emissive probe, the heating circuit detailed in 5.2.1, an box containing a ramp generator and a Langmuir probe circuit, a battery box with 6 activated batteries to shift the sweep and a digital oscilloscope. The ramps sweep was set to cover 90V. For both runs comparatively well known experimental conditions where chosen. Both source coils where set to 5A, the gas flow was 1,5sccm Argon, the RF power 600W forward and the probe heated with 2,65A. In the analysis, the sifting for modes was done with the internal oscilloscope time count as the x-axis of the signal and the potential equivalent to the drawn current delivered by the Langmuir box as the y-axis. The oscilloscope was set to acquire 10 million data points over a duration of 100ms. With one sweep on the display, the sweep frequency is 10Hz, which can be seen as slow enough compared to the 13,6 Mhz helicon frequency.

7.1 First Run

In the first run, more than one full sweep ramp was included in the data. Also, the mode the plasma was driven in was very "noisy" with several harmonics. The discreet step from highest ramp bias voltage to lowest ramp bias. This caused as many 35 modes to be sifted out, many only containing a signal at the steps, which can be linked to the Gibbs phenomenon and the sifting process reducing the discrete step in steps which size was guided by numerical abort parameters after too many iterations. Figure 7.1 shows some of the sifted modes. Clearly the two

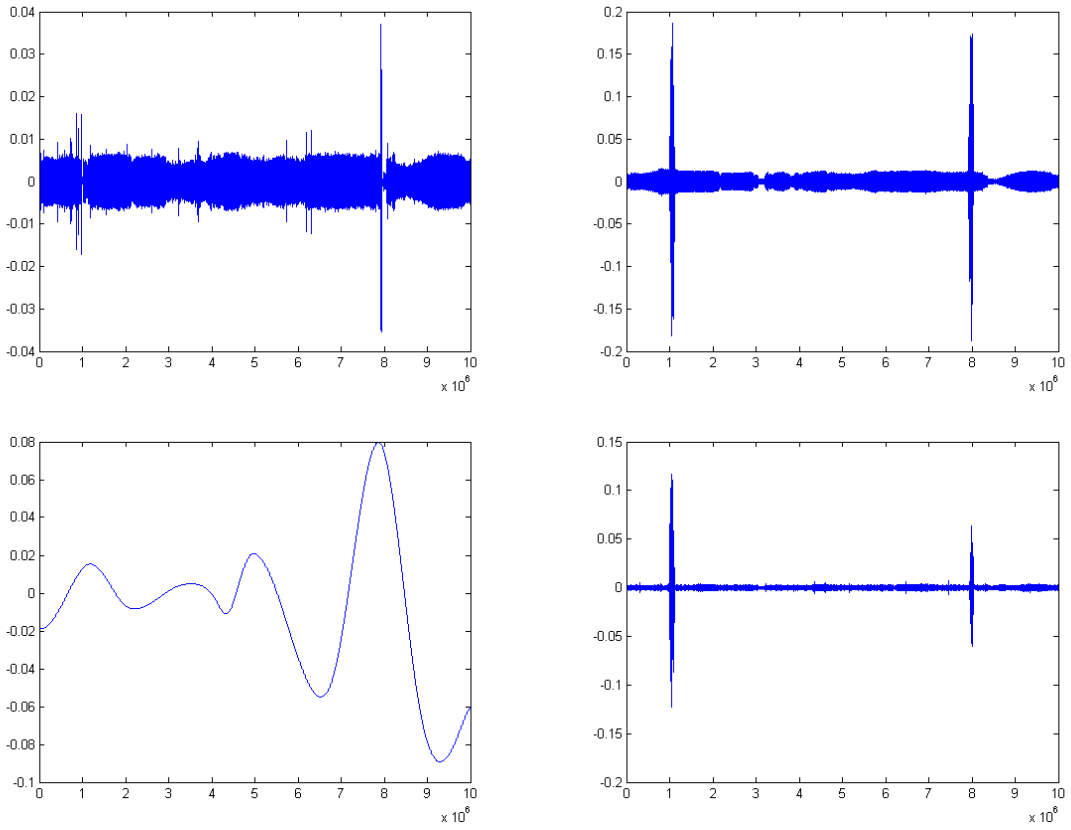

Figure 7.1: In the upper row, starting from the upper left corner, the 2nd, 4th mode. In the lower row the 6th and 32nd mode of the first EMD run

narrow peaks can be seen that mark the discreet steps, and how those spots grow more dominant in the higher modes. Also, the amplitude of all modes shows some fluctuation that seems to be connected to a beat frequency. Figure 7.2 shows the base trend. No features where visible probably connected to the problems of the numerics trying to apply a mathematical scheme incompatible with the discrete steps. So the run is considered to have given no usefull results.

7.2 Second Run

With the lesson from the first run, this time it was avoided to take in the steps. Also, it should be noted that fast fourier transformation of the floating potential revealed that one dominant harmonic was present with only a minor harmonic. This probably helped the second run to function far smoother than the first run. The sifting found quite a lot of modes again, but this time, the termination cri-

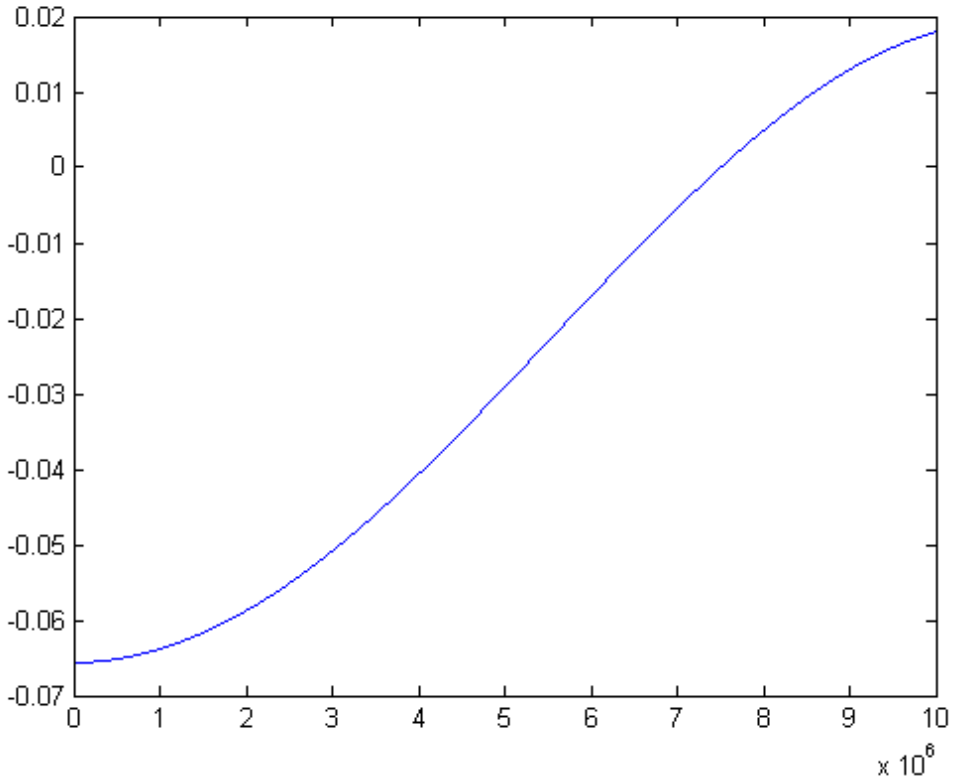

Figure 7.2: Base trend of the first EMD run

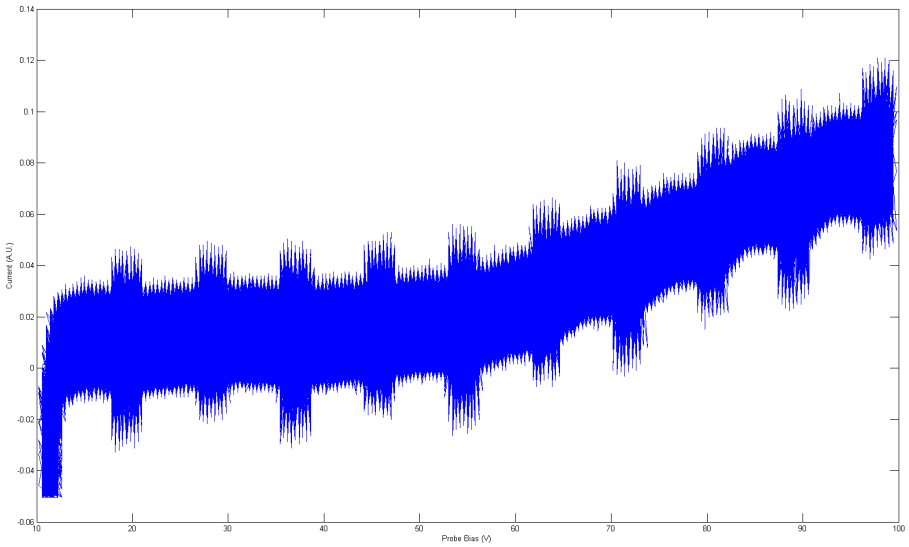

Figure 7.3: Original I-V trace used for the second EMD run

terion for standard deviation was reached always before the iteration limit was reached, which can be considered as a sign for better suited data (see chapter 5.2.7 for details. If the standard deviation between the points of two sifting iterations is below a certain threshold, they are considered the same and the function obtained in that iteration is taken as an intrinsic mode function).

Before discussing the sifted results, a look at the performance of the electronics is in order. Three effects potentially impacting the analysis come to mind. First, for small bias voltage, there seems to be a huge distortion in the current, as seen in figure 7.3. This is probably the result of a capacitance in the Langmuir sweep-box not being able to cope with the sweeping frequency and as such inducing a large slope with no physical basis at the beginning of each sweep. Also catching the eye in figure 7.3 are the low frequency peaks over the whole slope. They only occur when the sweep system is operated and not while letting the probe float (see figure 7.7), so again this is accredited to the electronics. The last problem is that the ramp voltage provided by the sweep-box to bias the probe is showing a high frequent oscillation with an amplitude of 1,6V. The voltage signal is shown against the internal oscilloscope time counter in figure 7.8. The first problem could be addressed by dropping the first part of the ramp, but as the potential is expected above 40V and the slope impact is expanding not further even in the in 26th mode, which should contain the slowest and thus furthest reaching compo-

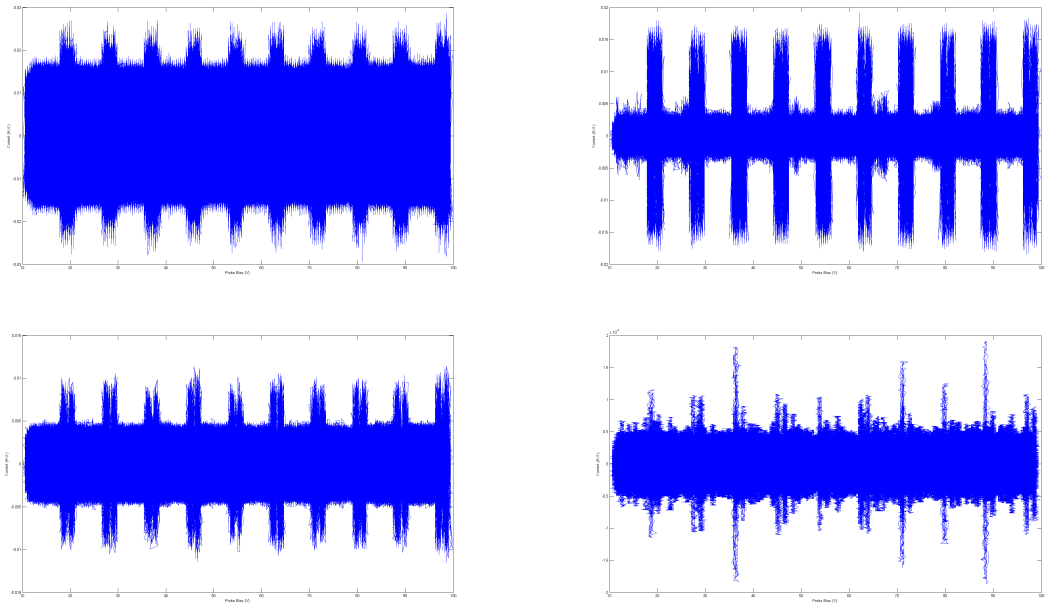

Figure 7.4: In the upper row, starting from the upper left corner, the 1st and 2nd mode. In the lower row the 3rd and 10th mode of the second EMD run

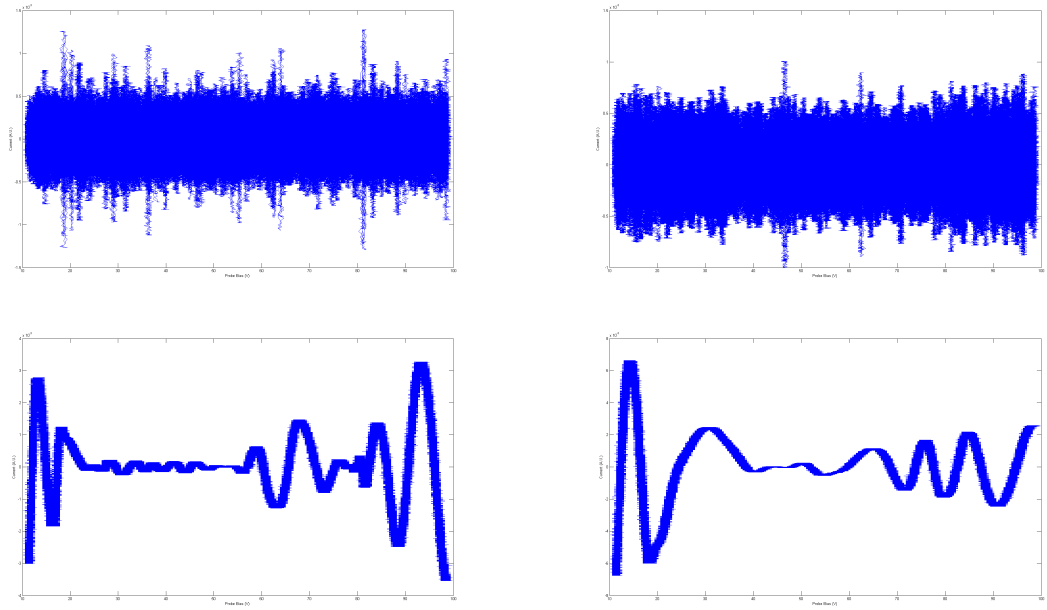

Figure 7.5: In the upper row, starting from the upper left corner, the 11th, and 12th mode. In the lower row the 25th and 26nd mode of the second EMD run

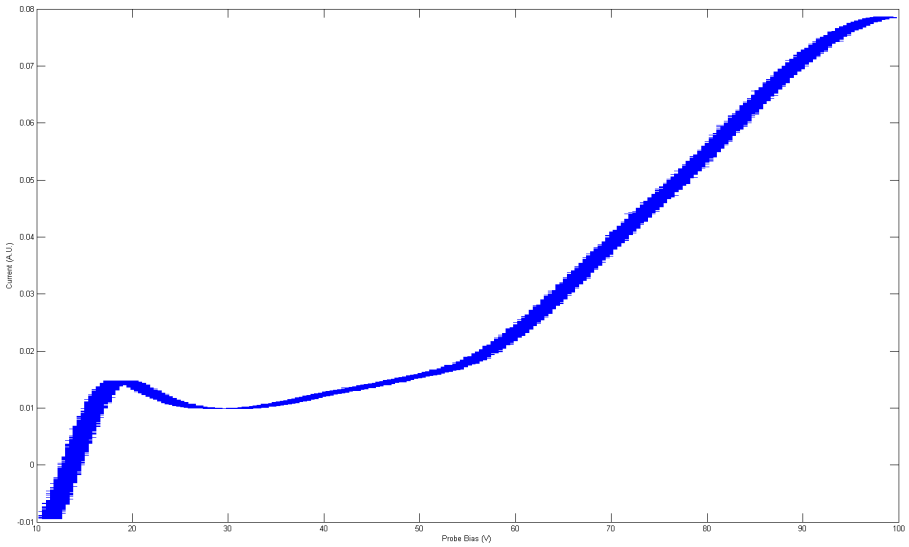

Figure 7.6: Base trend of the second EMD run

nents, it is simply ignored instead of cutting the data (see figure 7.5). The other two problems are problems of oscillatory nature and both seem to have a fixed frequency. As the EMD sifting is designed to filter out oscillating modes, it is proposed to simply ignore those issues as they should just create extra modes of low mode number, as they are high frequent. This can be seen in e.g. mode 2 (see figure 7.4), that seems to contain a big part of the artificial oscillation. For comparison, in figure 7.9, the modes are given against the oscilloscope time count, which cleans up the data significant. For the analysis there was no impact and the modes can be grouped in three groups, that are to be illustrated by the choice of mode sets printed in this thesis. A set of high frequency modes like mode 1 to 3, that carry the rapid oscillating probe signal. The medium frequency modes in the vicinity of mode 11, that probably carry some kind of noise and the low frequency modes near the base trend that are closely connected to "oscillation-like-changes"' in the base trend. "Oscillation-like-modes"' can be understood the way that an upward step-like function will be detected as a low frequency oscillation and a straight line trend directed upwards by the EMD. Looking at the simulations done for emissive probes in RF plasmas, it shows the I-V trace like a smooth step function, with steps around the potential. Looking at mode 25 in figure 7.5 backs up this assumption, as around the two peaks in figure 7.10 there is some distinct localized low frequency oscillation. This is why the normal peak broadening in RF plasmas should not be expected when using EMD. Figure 7.10 is the derivative of

the base trend obtained by sifting. The two peaks are at $\approx 67,5V$ and $\approx 82,5V$. The first peak should be the plasma potential. This is unusually high, yet not completely out of the expected frame. It could be due to experimental conditions, as the plasma was only showing one dominant mode while waveform monitoring. The second potential, which has previously been identified as a second electron distribution is visible to. The difference is with 15V a bit higher than observed in other comparable runs. However as explained in chapter 5.2.5, smoothing can shift a perceived peak upwards, as the new peak created by one sharp and one flat peak moves away from the sharp peak. A setup that is found when looking at the feature that makes up the second distribution in the derivative of normal characteristics like in figure 6.17. When applying a smoothing to the data, the second peak was found at up to 13V away for a gas flow of 1,5 sccm in the measurements for this thesis. So the unusual big potential distance between the two electron distribution is accredited to the smoothing effect of the EMD.
While the arguments given here are only qualitative, and not quantitative, in conclusion the EMD seems like a viable approach. Further experimentation is certainly necessary to evolve the concept further, but the first results look promising. As the physics are conserved, but noise is suppressed, the EMD inflection analysis method could prove to be a good approach when it comes to automating the data acquisition in plasmas with difficult RF oscillations close to noise. The distinction method between noise and peak that is described in 5.2.6, that makes the analysis of the I-V traces so slow, is with EMD exchanged for a numerical problem, whose solution speed is only dependent on available computing power. Also the Langmuir sweep box need a closer look as in the analysis process it is revealed to be quite a source of problems. But even under those complicating circumstances the approach gave a realistic appearing result.

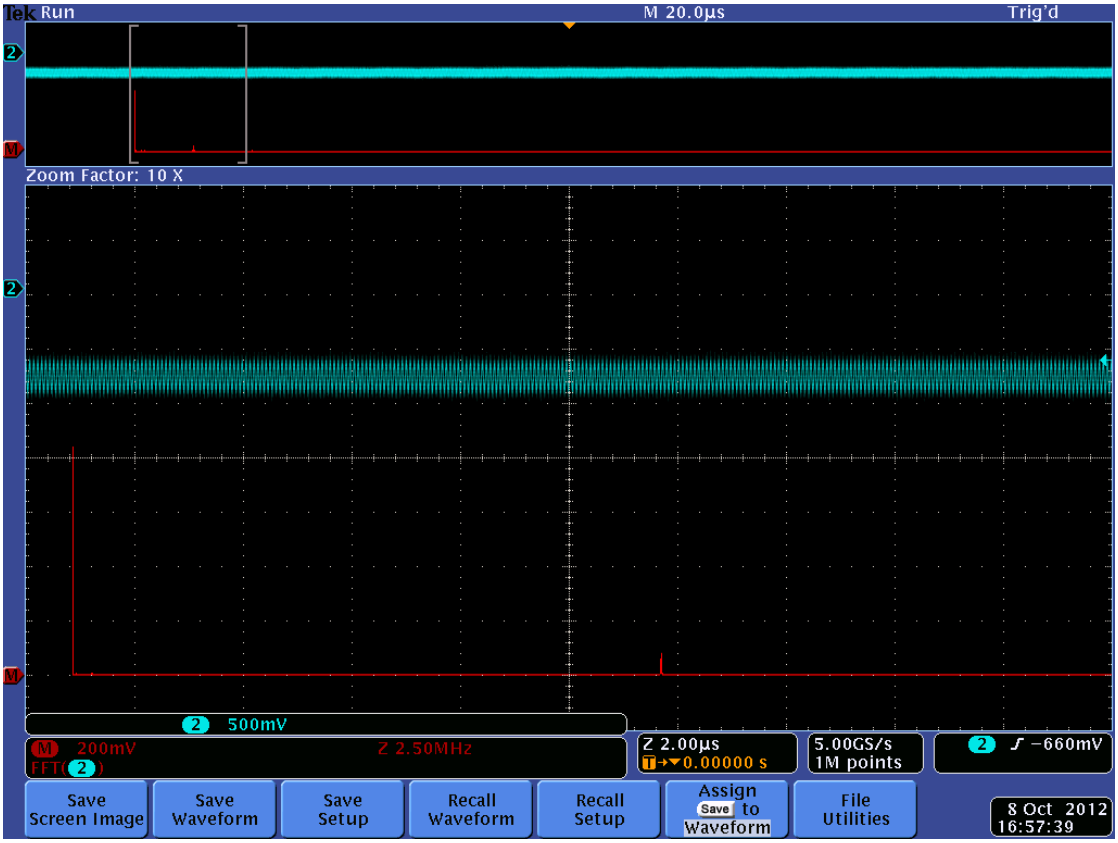

Figure 7.7: The probe in floating operation before taking the data for the second EMD run. Also, an FFT is visible to monitor the waveform as discussed in 5.2.5

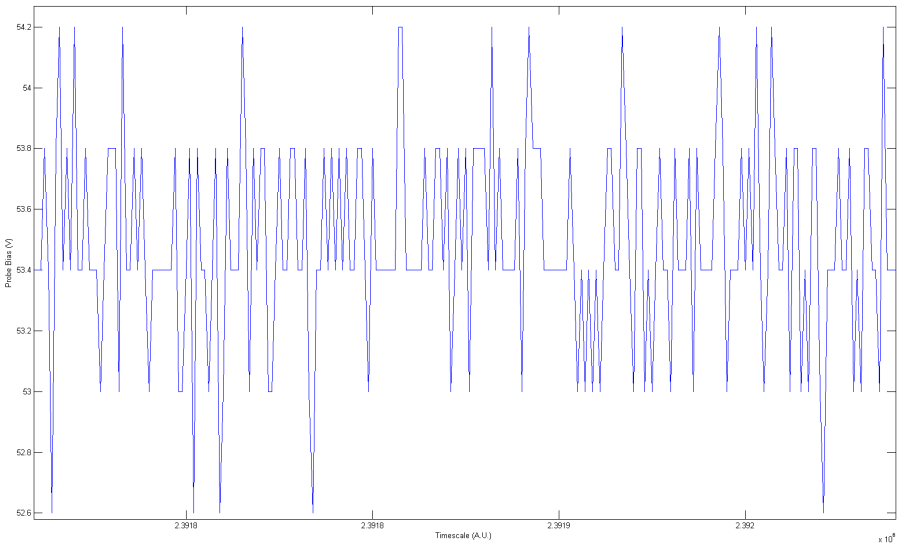

Figure 7.8: Short time frame of the bias potential in the second EMD run

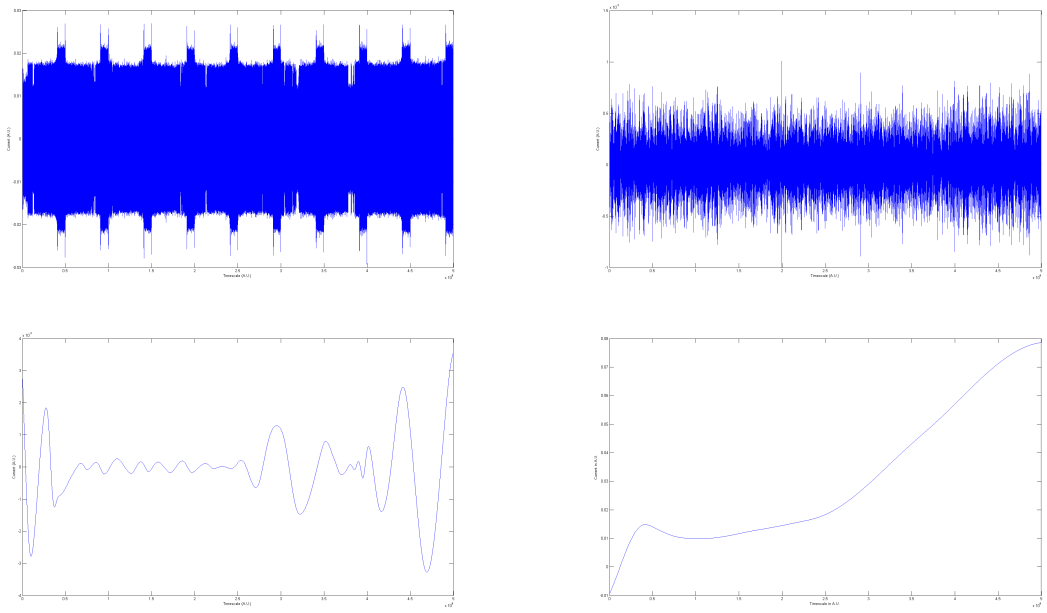

Figure 7.9: In the first row, starting from the upper left corner, the 1st and 12th mode. In the lower row the 25th and the base trend of the second EMD run. Not with voltage as x-Axis but with the oscilloscope internal time count, clearing up the data

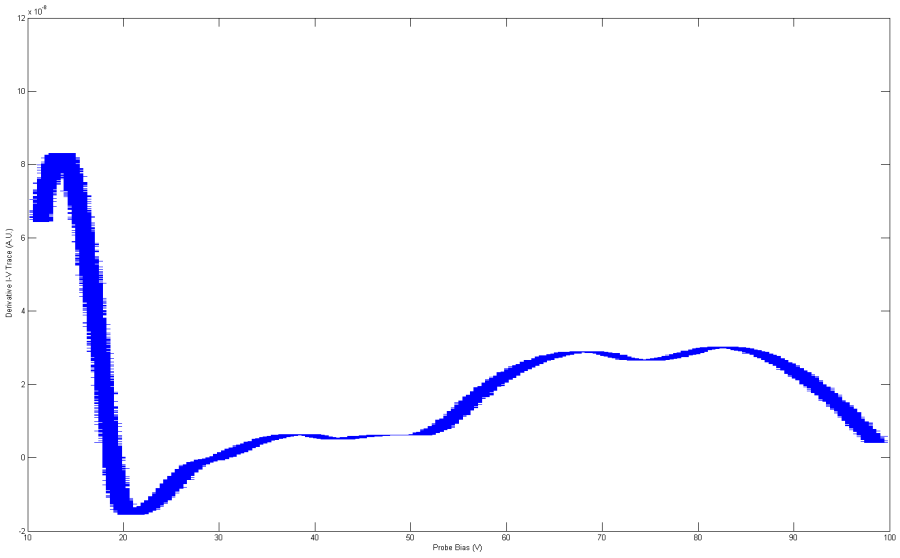

Figure 7.10: Derivative of figure 7.6 to determine the potential via inflection method

Chapter 8

Conclusion and further work

The emissive probe has been found to be a viable diagnosis tool in NJORD. A careful application has been able not only to give good measurements of the plasma potential but also to reveal other physical mechanisms.
Most important of these findings is the second electron distribution. Using an emissive probe to measure two distinct populations is novel, and might be better suited to do so than the standard procedure. In the standard procedure, the Druyvesteyn method, the second derivative of a cold Langmuir probe is taken and a change in slope indicates a change in temperature. With very similar temperatures and a high level of noise, it is possible that the change in slope is not visible. In an emissive probe, however, the features should still be visible, providing an easy acess.
Further insight into the physics of the plasma discharge could be gained by investigating the reason for the stable tooth and the loss of current that shows with emissive probes at higher pressure and strong positive bias. By using electronics with higher resolution and better control over the applied voltages and currents, the precision of the measurements should show some improvement. From the point of analyzing the plasma potential, the emissive probe, in combination with the already good accuracy, holds quite some potential. This is of use especially in relation to questions concerning electrons, which is a topic that is not easily assessed with RFEAs.
The main argument against emissive probes is, however, the high amount of work involved with the process of obtaining good measurements. Every measured plasma potential at some point is backed up by several potential measurements at different probe heating. As long as the phenomena noted earlier are not all fully understood, this requires inspection of the I-V traces in person and is not to be automated very well. Smoothing, as explained in the thesis, is also no truly viable option. From a point of efficiency, the emissive probe as such, is not the best way to obtain quick profiles for potential mapping, but rather a method to be applied

to predetermined points of interest in NJORD.
One approach taken to enable automated analysis was the use of empirical mode decomposition. While still having open issues, the preliminary results where promising. With a better Langmuir system that supplies a more stable voltage, further investigation into signal processing theory and access to more computing power, this avenue of approach could pose another opportunity to resolve the problem of cumbersome I-V trace analysis by hand.

Appendix A

Phyton Simulation Code

This code was used in simulating the probe in accordance with the model discussed in chapter 4.2.6. First, all arrays are created and the user is asked to enter his parameters. Then, two nested loops are called up to calculate every bias point defined in the array. The outer loop is a timeloop to go through twenty full oscillation of the slowest frequency. In every step, two things are done. First, the instantaneous potential is determined. Then, the inner loop is called up with this potential. In the inner loop, it is determined which current to used and then the current for every potential step is calculated and added to the array. After both loops have run, the arrays are divided by the amount of iterations that were added up and the result is given out. The program is also able to incorporate a secondary electron distribution and several RF harmonics. Note that the model is not fully calibrated an lacks hard-coded use of constants like e.g. κ, so that the results are qualitative and not quantitative.

```
# RF-Emissive Probe Sim for NJORD
# (c) by Christian Schregel
# Space Physics Group, Aurolab
# Universitaetet i Tromsoe, 2012
import math
#Initiate Datamatrix
Volt = ['Voltage','V']
ColCur = ['CollectedCurrent','A']
ColCur2 = ['CollectedCurrentBeam','A']
EmCur = ['EmittedCurrent','A']
ComCur = ['CombinedCurrent','A']
MainList = [Volt,ColCur,ColCur2,EmCur,ComCur]
#Initiate Variables
calcbeam = input('Calculate with Beam? (Yes or No)')
```

```
calcharmon = input('Calculate with n Harmonics? (Yes or No)')
Iel = float((input ('Electron Collection Saturation Current in A? (Standart:5)')))
Iem =float( input ('Electron Emission Saturation Current in A? (Standart:6)'))
Sweeprange= int(input ('Sweeprange in V?(Standart: 40)'))*10
Te =float( input ('Electron Temperature in eV? (Standart 3)'))
Tw = float(input ('Emitted Electron Temperature in eV? (Standart 0.3)'))
if calcbeam == 'Yes':
    secondpot = int((input ('Relative Beam Potential in regard to Plasmapotential in V? (Standart:20)')))*10
    if secondpot <0:
        print ('Beam has to have higher Potential then Plasma...')
        print ('Just what do you think you're doing, Dave?')
    else:
        Iel2 = float(input ('Beam Collection Saturation Current in A? (Standart: 1)'))
        Te2= float(input('Beam Electron Temperature in eV? (Standart 3)'))
RFAmp = float(input('RF-Osci-Amplitude in V? (Standart: 25)'))
if calcharmon== 'Yes':
    nharmon = int(input('How many Harmonics modes? (BaseRF is 1st Mode, Standart 3)'))
    RFAmparr = [RFAmp]
        for d in range (2,nharmon+1,1):
            print ('RF-', d,'. Harmonic')
            RFAmparr.append(float(input ('Amplitude in V ?')))
#RFAmp3 = float(input('RF-3rd-Harmonic-Osci-Amplitude in V?(Standart 10)'))
print('Starting Calculations. Please wait')
#RFLoop
for c in range (2,(Sweeprange+1)*2+1):
    Volt.append(0)
    ColCur.append(0)

       ColCur2.append(0)
    EmCur.append(0)
    ComCur.append(0)
for t in range (2,2002,1):
    if calcharmon=='Yes':
        VRF = 0
        for e in range (0,len(RFAmparr),1):
            VRF=VRF+RFAmparr[e]*math.sin((e+1)*math.pi/100*t)
    else:
```

```
        VRF=RFAmp*math.sin(math.pi/100*t)
    for V in range (-1*Sweeprange-1,Sweeprange,1):
        V = V+1
        RFLC = V+Sweeprange+2 #Marker for saving Data in Arrays
        Volt[RFLC]=V/10
        if V<VRF:
            ColCurh = Iel*math.exp((V-VRF)/10/Te)
            ColCur2h = 0
            if calcbeam == 'Yes':
                 if V <= secondpot+VRF:
                     ColCur2h = Iel2*math.exp((V-(VRF+secondpot))/10/Te)
                 elif V> secondpot+VRF:
                     ColCur2h = Iel2*math.sqrt(1+((V-(VRF+secondpot))/10/Te))
            EmCurh = -1*Iem
            ComCurh = (ColCurh+ColCur2h+EmCurh)
            ColCur[RFLC] = ColCur[RFLC]+ColCurh
            ColCur2[RFLC] = ColCur2[RFLC]+ColCur2h
            EmCur[RFLC] = EmCur[RFLC]+EmCurh
            ComCur[RFLC] = ComCur[RFLC]+ComCurh
        #print (V/10,ColCur,EmCur,ColCur2,ComCur)
        elif V == VRF:
            ColCurh = Iel*math.exp((V-VRF)/10/Te)
            EmCurh = -1*Iem*math.exp(-(V-VRF)/10/Tw)
            ColCur2h = 0
            if calcbeam == 'Yes':
                if V<=secondpot+VRF:
                    ColCur2h = Iel2*math.exp((V-(VRF+secondpot))/10/Te)
                elif V>secondpot+VRF:
                    ColCur2h = Iel2*math.sqrt(1+((V-(VRF+secondpot))/10/Te))
            ComCurh = (ColCurh+ColCur2h+EmCurh)
            ColCur[RFLC] = ColCur[RFLC]+ColCurh
            ColCur2[RFLC] = ColCur2[RFLC]+ColCur2h
            EmCur[RFLC] = EmCur[RFLC]+EmCurh
            ComCur[RFLC] = ComCur[RFLC]+ComCurh
        #print (V/10,ColCur,EmCur,ColCur2,ComCur)
        elif V>VRF:
            ColCurh = Iel*math.sqrt((1+(V-VRF)/10/Te))
            EmCurh = -1*Iem*math.exp(-(V-VRF)/10/Tw)*math.sqrt((1+(V-
VRF)/10/Tw))
            ColCur2h = 0
```

```
                if calcbeam == 'Yes':
                    if V<=secondpot+VRF:
                        ColCur2h = Iel2*math.exp((V-(VRF+secondpot))/10/Te)
                    elif V>secondpot+VRF:
                        ColCur2h = Iel2*math.sqrt(1+((V-(VRF+secondpot))/10/Te))
                ComCurh = (ColCurh+ColCur2h+EmCurh)
                ColCur[RFLC] = ColCur[RFLC]+ColCurh
                ColCur2[RFLC] = ColCur2[RFLC]+ColCur2h
                EmCur[RFLC] = EmCur[RFLC]+EmCurh
                ComCur[RFLC] = ComCur[RFLC]+ComCurh
            # print (V/10,ColCur,EmCur,ColCur2,ComCur)
for b in range (2,len(Volt)):
    ColCur[b]=ColCur[b]/2000
    ColCur2[b]=ColCur2[b]/2000
    EmCur[b]=EmCur[b]/2000
    ComCur[b]=ComCur[b]/2000
print ('Calculation Complete,Begin Result Output.')
for a in range (0,len(Volt),1):
    print (Volt[a],ColCur[a],ColCur2[a],EmCur[a],ComCur[a])
print ('Done. Simulation Finished')
```

Appendix B

EPS/ICPP 2012 Poster

Preliminary results of this thesis were presented on the EPS/ICPP 2012 conference taking place in Stockholm. For documentation purposes, the poster presented is included here.

UNIVERSITY OF TROMSØ UiT

Emissive probe measurement in a Helicon device

C. Schregel, A. Fredriksen

Dept. Of Physics and Technology

email: csc010@post.uit.no

Abstract

The most commonly used method for plasma potential determination in Helicon devices is the Retarding Field Energy Analyser (RFEA). In this work, emissive probes where applied to the same problem. Facing unique difficulties, they deliver a fresh look and reveal the presence of a two electron populations in the downstream plasma.

Determining a radial potential profile by emissive Probes

The most widely used method of plasma potential identification is the inflection point method by Smith et al.[2]. Using linear approximation of the plasma-potential-shift with increasing emission saturation current it is in theory possible to determine the plasma potential within a range of T_e/10e [3]. In RF plasmas with several dominating harmonics, a part of this accuracy is lost, as the peaks overlap and make identification of the potential difficult. Another problem is posed by strong noise creating false peaks. A useful method to identify the potential amidst RF noise in a given I-V Trace is to look at many peaks in the derivative (and deformations in inclination) and determine the mid-point between pairs. Around the potential, the matching pairs should show a similar, stable midpoint. If wrongly a pair of peaks caused by noise has been included, the midpoint, due to the randomness of noise, reflects this by moving. Further methods to narrow down to the exact number of RF-caused peaks include monitoring the time-resolved behaviour of the floating potential of an emissive probe to get an estimate for the expected peak-to-peak distance and, by Fourier transformation, the number and amplitude-ratio of the harmonics

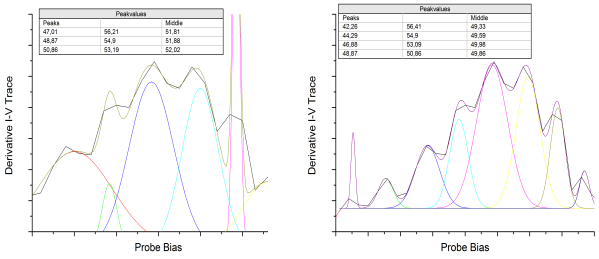

Comparison middle-point with and w/o inclusion of peaks created by noise

Care should also be taken about the intensity of heating, as features of interest get suppressed in the derivative if the emission current is to high. Also, at to high emission, the distortion is too high to gain useful data, as e.g. on the right hand side, a distinct, stable peak forms. Further research is required to determine the cause for this peak. The obtained profiles show expected values for the potential and also behavior at the edge of the source region seen with RFEAs

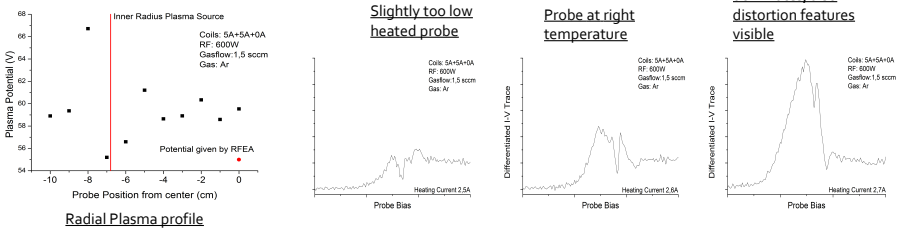

Radial Plasma profile

Experimental Setup

Device[1]:
Chamber: Length 1,2m + Half-Dome 0,3m; Diameter 0.6m
Vacuum: Base pressure 1x10-6 Torr
Source: Inductively coupled RF through pyrex cylinder (Length 0.305m;Inner Diameter 0,138m), Saddle Antenna (Boswell Type), coupled to a 13,5Mhz RF-signal, 0,3-1kW
Magnetic: 3 Coils, 2 in Source, 1 Guidecoil (unused) at 1.8cm, 23.3cm and 58cm from end of source
Typical Parameters:
Gas: Argon
Plasma Potential: 70V-100V in source, 30-60V at 50cm (radial probe position)
Densities: 1-7x10^17m-3 in source, 0.2-5x10^17m-3 at 50cm
Electron Temperature: 3-6eV

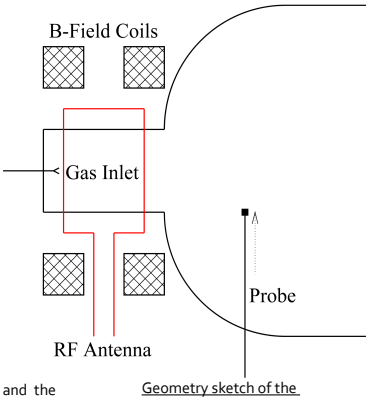

Geometry sketch of the NJORD experimental setup

The emissive probe is driven by a continuous DC heating and the current. The spot welds serve to ensure good control over the region of heated wire so that no heating takes place within the ceramic tube. Heating can be controlled by simply varying the current. Probe temperature can be monitored with a spectrometer and be determined by fitting an a Planck-Spectrum to it. The current is sampled 201 times for each out of 201 bias steps and the average current and bias voltage of each step written to disk. Averaging is necessary to reduce noise as nonlinear dynamics in the plasma make it difficult to determine the potential otherwise.

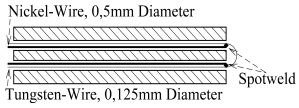

Sketch of the Emissive Probe used

Numerical Simulation

A basic numeric simulation can simulate expected I-V-traces and their respective derivatives..The program does not consider more advanced modeling for the emitted current given by Ye & Takamura [3] but use the simpler approach given by Hershkowitz et. al.[4]:

$$I_{Combined} = I_{Collected} + I_{Emitted}$$

$$I_{Collected} = I_{e0} * e^{\frac{e\Delta V}{T_e}} \; for \; V_{bias} < V_{Plasma}, \; I_{e0} * g(\Delta V) \; for \; V_{Plasma} < V_{bias}$$

$$I_{Emitted} = I_{em0} \; for \; V_{bias} < V_{Plasma}, \; I_{em0} * e^{\frac{-e\Delta V}{T_{Wire}}} * f(\Delta V) \; for \; V_{Plasma} < V_{bias}$$

A time averaging over several periods of an oscillating space potential is done like in the experimental setup. The amplitude, number and order of harmonics can be chosen to simulate a potential behaving as close as possible to the experiment. It show quite clearly that the measured data can be explained with two distributions at different potentials if the values for harmonic number, order and amplitude are chosen within observed ranges.

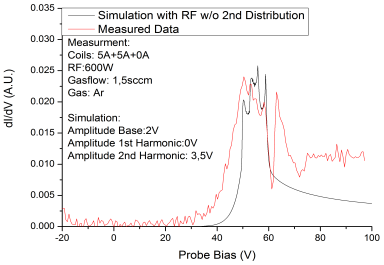

Comparison between simulations

Monitoring the behavior of the two distributions over pressure range

The plasma potential has been measured over a pressure range of ???? to ?????. For better visibility of important features is its feasible to smooth the data by a 2nd order 7 point Savitsky Golay filter. A certain loss of information is inevitable as the peak broadening is on the same level as the noise, but the ratio of saturation currents for the two electron distributions is kept. Of interest in this case is the behavior of the second electron distribution. The difference between the plasma potential, which drops with increasing pressure, and the second distribution stays roughly at an value of 9V. The saturation current ratio increases strong with pressure. This is in agreement with increased plasma density with pressure, as is commonly observed in our plasma Another finding is, that especially at higher pressure it is an easy fallacy to take the two populations as two peaks, which leads to a too high estimate of the plasma potential. This can be avoided by monitoring of the probe behavior while increasing the pressure.

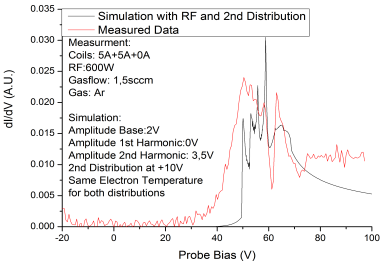

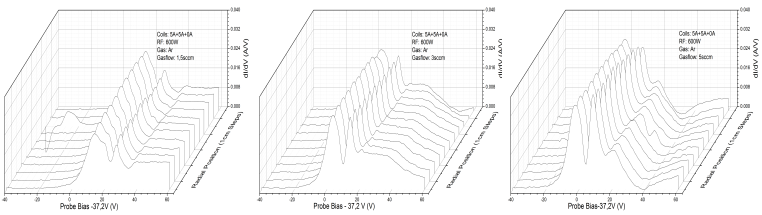

Smoothed I-V-Trace derivatives for several pressures

Conclusion

Although some issues remain when using emissive probes in Helicon-devices, there is given good potential. Care has to be taken to obtain good and useful data to avoid missassumptions. But data fulfilling those requirements matches the data obtained by RFEA measurements and gives strong indication for the presence of two distinct electron populations. The origin of the second population has so far not been determined.

References:

[1]Fredriksen A., Mishra L.N. Et al.;Plasma Sources Sci. and Technol., 19 034009 (2010)
[2] Smith J.R., Hershkowitz N. Et al.; Rev. Sci. Instrum. 50, 210 (1979)
[3]Ye M.Y. & Takamura S.; Phys. Plasmas 7, 3457 (2000)
[4] Sheehan J.P. &Hershkowitz N.;Plasma Sources Sci. Technol. 20 (2011) 063001

Bibliography

[1] C. Charles, "Topical review: A review of recent laboratory double layers experiments," *Plasma Sources Sci. Technol.*, vol. 16, pp. R1–R25, 2007.

[2] F. Chen, *Introduction to Plasma Physics and Controlled Fusion*, vol. 1. Springer, 2 ed., 2006.

[3] P. Bellan, *Fundamentals of Plasma Physics*. Cambridge University Press, 2008.

[4] T. Boyd and J. Sanderson, *The Physics of Plasmas*. Cambridge University Press, 2005.

[5] P. Chabert and N. Braithwaite, *Physics of Radio-Frequency Plasmas*. Cambridge University Press, 2011.

[6] I. Hutchinson, *Principles of Plasma Diagnostics*. Cambridge University Press, 2002.

[7] P. Debye and E. Hueckel, "Zur theorie der elektrolyte i. gefierpunktserniedrigung und verwandte erscheinungen," *Physik.Zeits.*, vol. 24, p. 185, 1923.

[8] N. Hershkowitz, "Sheath: More complicated than you think," *Phys. Plasmas*, vol. 12, p. 055502, 2005.

[9] S. Baalrud and N. Hershkowitz, "The nature of an electron sheath in steady-state, low-pressure plasma," in *Plasma Science, 2006. ICOPS 2006. IEEE Conference Record - Abstracts. The 33rd IEEE International Conference on*, 2006.

[10] R. Stenzel, "High frequency instablity of a magnetized spherical electron sheath," *Phys. Plasmas*, vol. 17, p. 062109, 2010.

[11] T. Stix, *The Theory of Plasma Waves*. McGraw-Hill, 1962.

[12] R. Boswell and F. Chen, "Helicons - the early years," *IEEE Trans. Plasma Sci.*, vol. 25, pp. 1229–1243, 1997.

[13] F. Chen, "Plasma ionization by helicon waves," *Plasma Phys. Control. Fusion*, vol. 33, pp. 339–64, 1991.

[14] A. Anders and M. Kuhn, "Characterization of a low-energy constricted-plasma source," *Rev. Sci. Instrum.*, vol. 69, pp. 1340–1343, 1998.

[15] C. Ionita, D. D.-G., and R. Schrittwieser, "Elementary processes at the origin of the generation and dynamics of multiple double layers in dp machine plasma," *Int. J. Mass Spec.*, vol. 233, pp. 343–354, 2004.

[16] N. Singh, "Current-free double layers: A review," *Phys. Plasmas*, vol. 18, p. 122105, 2011.

[17] S. Pottinger, V. Lappas, C. Charles, and B. R., "Performance characterization of a helicon double layer thruster using direct thrust measurements," *J. Phys. D: Appl. Phys.*, vol. 44, p. 235201, 2011.

[18] F. Chen, "Physical mechanism of current-free double layers," *Phys. Plasmas*, vol. 13, p. 034502, 2006.

[19] M. A. Lieberman, C. Charles, and R. W. Boswell, "A therory for formation of a low pressure, current-free double layer," *J. Phys. D: Appl. Phys.*, vol. 39, pp. 3294–3304, 2006.

[20] C. Charles, "High density conics in a magnetically expanding helicon plasma," *Appl. Phys. Lett.*, vol. 96, p. 051502, 2010.

[21] J. Sheehan and N. Hershkowitz, "Topical review: Emissive probes," *Plasma Sources Sci. Technol.*, vol. 20, p. 063001, 2011.

[22] R. Kemp and J. Sellen, "Plasma potential measurements by electron emissive probes," *Rev. Sci. Instrum.*, vol. 37, p. 455, 1966.

[23] S. Takamura, N. Ohno, M. Ye, and T. Kuwabara, "Space-charge limited current from plasma-facing material surface," *Contrib. Plasma Phys.*, vol. 44, pp. 126–137, 2004.

[24] L. Schwager, "Effects of secondary and thermionic electron-emission on the collector and source sheaths of a finite ion temperature plasma using kinetic-theory and numerical-simulation," *Phys. Fluids. B*, vol. 5, p. 631, 1993.

[25] J. Smith, N. Hershkowitz, and P. Coakley, "Inflection point method of interpreting emissive probe characteristics," *Rev. Sci. Instrum.*, vol. 50, p. 210, 1979.

[26] M. Ye and S. Takamura, "Effect of space-charge limited emission on measurements of plasma potential using emissive probes," *Phys. Plasmas*, vol. 7, p. 3457, 2000.

[27] E. Wang, T. Hershkowitz, N. an Intrator, and C. Forest, "Techniques for using emitting probes for potential measurement in rf plasmas," *Rev. Sci. Instrum.*, vol. 57, p. 2425, 1986.

[28] M. Wiebold, T.-Y. Sung, and J. Scharer, "Ion acceleration in a helicon source due to the self-bias effect," *Phys. Plasmas*, vol. 19, p. 053503, 2012.

[29] T. Lafleur, C. Charles, and B. R., "Detailed plasma potential measurements in a radio-frequency expanding plasma obtained from various electrostatic probes," *Phys. Plasmas*, vol. 16, p. 044510, 2009.

[30] G. Tribulato, "Characterization of a magnetized plasma in cylindric geometry," Master's thesis, Universitetet i Tromso, 2007.

[31] R. Schrittwieser, "Course on vacuum physics." Lecture, Januar 2010.

[32] H. Conrads and M. Schmidt, "Plasma generation and plasma sources," *Plasma Sources Sci. Technol.*, vol. 9, pp. 441–454, 2000.

[33] K. Takahashi, C. Charles, R. Boswell, and R. Hatakeyama, "Radial characterization of the electron energy distribution in a helicon source terminated by a double layer," *Phys. Plasmas*, vol. 15, p. 074505, 2008.

[34] A. Siebenforcher and R. Schrittwieser, "A new simple emissive probe," *Rev. Sci. Instrum.*, vol. 67, pp. 849–850, 1996.

[35] X. Sarasola, "Personal correspondence on the application of emd.".

[36] N. Huang, S. Z., S. R. Long, M. Wu, H. Shih, Q. Zheng, N. Yen, C. Tung, and L. H.H., "The empirical mode decomposition and the hilbert spectrum for nonlinear and non-stationary time series analysis," *Proc. R. Soc. Lond. A*, vol. 454, pp. 90–995, 1998.

[37] W. J. Milloch, N. Gulbrandsen, L. Mishra, and A. Fredriksen, "The role of acceptance angle in measurements with ion energy analyzers: Study by numerical simulations," *Appl. Phys. Lett.*, vol. 97, p. 261501, 2010.

[38] T. Lho, N. Hershkowitz, G. Kim, W. Steer, and J. Miller, "Asymmetric plasma potential fluctuation in an inductive plasma source," *Plasma Sources Sci. Technol.*, vol. 9, pp. 5–11, 2000.